Machine learning-based additive manufacturing process optimization and quality prediction with photomicrography and tomography

by

Jiafeng Ye

A dissertation submitted to the Graduate Faculty of
Auburn University
in partial fulfillment of the
requirements for the Degree of
Doctor of Philosophy

Auburn, Alabama
August 05, 2023

Key words: additive manufacturing, machine learning, fused deposition modeling, laser beam powder bed fusion, process optimization, defect classification, x-ray computed tomography, critical defect identification

Approved by:

Dr. Jia (Peter) Liu, Assistant Professor Industrial & Systems Engineering
Dr. Shuai Shao, Associate Professor Mechanical Engineering
Dr. Daniel Silva, Associate Professor Industrial & Systems Engineering
Dr. Aleksandr Vinel, Associate Professor Industrial & Systems Engineering
Dr. Xinyu Zhang, Professor Chemical Engineering

Abstract

Process optimization and quality prediction are essential for promoting manufacturing quality and improving product reliability in Additive manufacturing (AM). However, the complex multi-physics processes of AM, involving process-material interactions, melt pool dynamics, phase transformation, and microstructure development, result in challenges for finding the optimal process conditions (especially of AM fabrications with advancing novel materials design) and forecasting the mechanical properties of the AM parts.

With the ever-expanding data availability of AM by various sources (e.g., photomicrography and tomography), data-driven machine learning (ML) modeling has gained increasing attention in AM research. Compared to trial-and-error or computational approaches, ML modeling can bypass the complex physics-based model of AM, explore the feasible space efficiently, and reduce time and cost for process optimization and quality prediction by using computationally inexpensive algorithms.

In this dissertation, two different AM technologies, namely, fused filament fabrication (FFF) and laser beam-powder bed fusion (L-PBF) processes, are investigated for adoptions of ML-based process optimization and quality prediction, utilizing the data from photomicrography and tomography, such as the optical microscope, scanning electron microscope (SEM), and X-ray computed tomography (XCT). The overarching goal of this dissertation is to develop innovative methodologies tailored for different objectives regarding efficient process optimization and accurate quality prediction for FFF and L-PBF processes based on photomicrography and tomography data. Specifically, three new methodologies are developed as follows:

First, a data-driven nonparametric Bayesian framework is developed to unify nanocomposite design and part fabrication by integrating statistical learning and optimization into quality prediction and process optimization. It regulates the design and fabrication of specimens with different materials composition using the FFF process and ensures successful printings and accurate quality prediction while maintaining its design flexibility and customization. It can be easily extended to other materials and will have a profound influence on advancing their applications and innovations in various industries.

Second, an ML-driven framework is proposed to conduct an efficient and accurate defect classification for the L-PBF process by the distinct morphology and size of each defect type obtained from the XCT scans. It leverages the efficiency of low-resolution (LR) XCT scanning and ML to achieve improved defect inspection efficiency and classification accuracy simultaneously. The classification results from the proposed framework can be used as an effective method to identify the most detrimental defect type in the L-PBF parts to the fatigue performance and rectify the fabrication conditions of the L-PBF process for future manufacturing.

Third, a cross-dimensional (3D/2D) defect matching process is proposed to identify the matches to the critical defects (i.e., defects at fracture origin) among numerous volumetric defects in the XCT scans of the L-PBF parts. It exploits the defect features extracted from SEM-based fractography to characterize the positions, sizes, and morphologies of the critical defect for identifying the volumetric defect in the XCT scans with the highest similarities to the critical defect as the match. Identifying the match to the critical defect not only reveals the important features of the critical defect, which contributes to the fatigue life of L-PBF parts but also opens the possibility of critical defect identification and fatigue life prediction non-destructively.

Acknowledgments

I would like to express my deepest gratitude and appreciation to my esteemed academic advisor, Dr. Liu, for his exceptional mentorship, including constructive guidance, unwavering support, and great patience throughout my Ph.D. study. Beyond this, his passion and dedication to his field are instrumental in shaping my attitude toward future work.

I am truly grateful for Dr. Vinel and Dr. Silva, who generously invested their time and effort into mentoring me. Their insightful guidance and critical feedback have consistently challenged me to think critically, push the boundaries of my research, and strive for excellence in all aspects of my work.

I would also like to thank Dr. Shao and Dr. Zhang, whose willingness to engage in meaningful discussions and provide constructive criticism based on their profound knowledge has significantly enhanced my academic growth and enriched the quality of my research.

Also, our collaborators Arun Poudel, Muztahid Muhammad, and Mohammad Salman Yasin from the Mechanical Engineering Department and Fahim Momin from the Chemical Engineering Department have been continuously supportive of my research by providing invaluable data.

I would like to extend my sincere gratitude to my lab mates Anyi Li, Tianyu Gao, Enkai Bi, and Mohammad Shahadath Hossain, whose inspiring thinking and valuable suggestions have contributed significantly to my research endeavors.

Lastly, I want to acknowledge the support of my beloved parents and my best friend, Yida Bao, whose unwavering encouragement, and understanding have been the pillars of my success throughout this journey.

Table of Contents

List of Tables

List of Figures

1 Introduction

1.1 Background

Additive manufacturing (AM) refers to "the process of joining materials to produce parts from a three-dimensional (3D) computer-aided design (CAD) model, layer by layer, as opposed to subtractive manufacturing processes" [1, 2]. Like subtractive manufacturing, AM is applicable to a wide range of materials (e.g., metal, alloy, polymer, composite, ceramic, wood, and glass) by different technologies (e.g., laser beam-powder bed fusion, fused filament fabrication, binder jetting). However, AM generally offers better design flexibility for the parts with intricate designs or complex geometries than subtractive manufacturing[1-3]. There are many proceeding applications of AM by various industries to fabricate parts with complex geometrical designs, such as aerospace (e.g., turbine blades and fuel nozzles), automotive (e.g., electric motors and rims), and biomedical (e.g., surgical implants and tissue engineering scaffolds) [4-11], which are difficult to fabricate by subtractive manufacturing. Meanwhile, AM is ever-evolving with innovative materials and improved fabrication quality to find its way into more application areas [12-14]. In this case, the value of the global AM market is expected to skyrocket from $10.495 billion in 2020 to $65.148 billion by 2027 [15], showing a promising future for AM.

The fused filament fabrication (FFF) process is among the most used AM technologies for its superior accessibility [16]. The FFF parts can be fabricated through those affordable and user-friendly in-house desktop printers, as shown in Figure 1(a) and (b), with commercially available, inexpensive materials (e.g., acrylonitrile butadiene styrene (ABS) and polylactic acid (PLA)). In this context, companies, universities, various independent groups, and individuals took advantage of the excellent design flexibility and user accessibility of the FFF process for rapid prototyping of personal protection equipment (PPE) (e.g., face-protecting shields and safety goggles) and medical devices (e.g., ventilator valves and splitters) to fight the shortages at the beginning of the global pandemic of coronavirus disease 2019 [17-20].

As shown in Figure 1(d), the FFF process fabricates parts layer-wise by melting filaments through an extruder and depositing the molten filaments on the printing bed to fabricate parts with complex geometrical designs [21, 22]. The quality of FFF parts is strongly influenced by the combination of three key process parameters (i.e., extruder temperature, print speed, and layer thickness) used in the FFF process [23, 24]. For instance, the inferior surface quality of the FFF parts with defects (i.e., voids, under-fill, over-fill) caused by non-optimal process parameters was reported in many studies [21, 25, 26]. Meanwhile, the inferior surface quality can impair the functionality and assembly, the precision of the dimensions fit, and the mechanical properties of the FFF parts [27, 28]. Therefore, it is essential to find optimal process parameters for fabricating high-quality FFF parts.

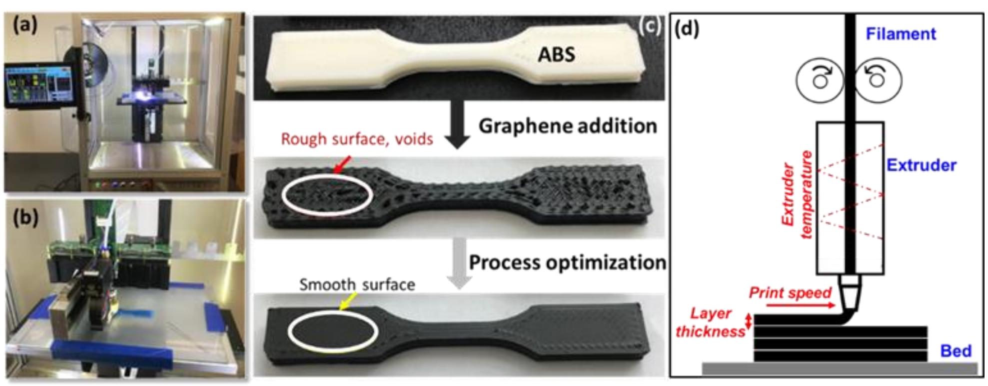

Figure 1 (a) A Hyrel System 30M 3D printer used in the study and (b) its build platform. (c) The illustration of the interactions between graphene composition and FFF process parameters affecting the properties and quality of the FFF parts with ABS/graphene nanocomposites. A defect-free FFF part with ABS fabricated under a feasible process condition; adding graphene without adjusting the process parameters leads to defects on the FFF part with ABS/graphene nanocomposite; after properly adjusting the FFF process parameters, the fabricated part with the same nanocomposite has a defect-free surface finish. (d) The sketch of the extrusion of the FFF machine indicates the critical process parameters.

Another commonly used AM technology is the laser beam powder bed fusion (L-PBF) process, which is among the dominating technologies in the metal AM market [29]. L-PBF parts can achieve comparable dimensional accuracy to those fabricated by subtractive manufacturing processes (e.g., machining and casting) [30]. Furthermore, the design freedom inherited from AM of the L-PBF process enables part consolidation, i.e., reducing the number of components and raw materials by fabricating a single part with complex structures through topology optimization [31]. The benefits of part consolidation include reducing the cost (using fewer raw materials) and lead time (minimizing assembly operations), and fabricating lightweight parts with a high strength-to-weight ratio [10, 31]. These benefits primarily cater to the demands of the aerospace sector, one of the largest sectors in the U.S. [32], thus enabling the adoption of the L-PBF process in this industry. A typical example of the L-PBF process in aerospace applications is that Genetic Electric company has consolidated a 20-parts fuel nozzle for aircraft engines into a single L-PBF part with a 25% weight reduction [33].

As shown in Figure 2(a), the L-PBF process fabricates 3D parts by localized melting and fusing the powder particles through a laser beam energy source, layer upon layer, into a pre-defined pattern within an enclosed building chamber filled with inert gas (e.g., argon or nitrogen) to prevent oxidation [5, 34-37]. Like the FFF process, the quality of L-PBF parts is also largely affected by four key process parameters (i.e., laser power, scanning velocity, hatch distancing, and layer thickness) used in the L-PBF process [38]. For instance, these four process parameters can control the energy input of the L-PBF process [39-41]; meanwhile, different energy inputs lead to the formation of different types of volumetric defects [39, 42, 43], which can negatively affect the mechanical properties of the L-PBF parts [44, 45].

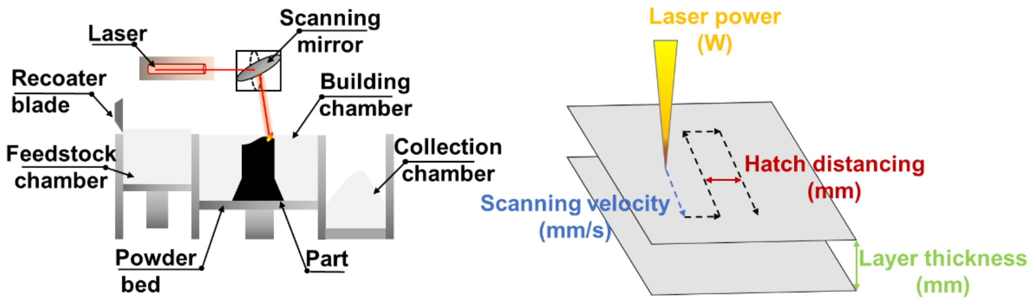

Figure 2 (a) The schematic diagram and (b) four key process parameters of the L-PBF process

Three major types of defects, i.e., keyholes (KHs), lack of fusions (LoFs), and gas-entrapped pores (GEPs), can occur in the L-PBF process primarily caused by different energy inputs [39, 42, 43, 46-49]. These defects severely influence the reliability and durability of the L-PBF parts, specifically in fatigue-critical applications [44, 45, 50, 51]. For instance, they can initiate cracks, leading to impaired mechanical properties and reduced fatigue life of the L-PBF parts [52-55]. Hence, for fabricating high-quality L-PBF parts, it is critical to prevent defects. One specific task that can help with this overarching goal is to be able to correctly identify defect types and their influence on the structural integrity of the part [56, 57], as it can enable rectifying inappropriate energy inputs.

Moreover, fatigue life is an essential criterion to evaluate the reliability and durability of components under cyclic loadings for many applications [44, 58-62]. However, fatigue life of L-PBF parts is inferior to their wrought counterparts, which affects their functionality in the safety-critical task, such as the aforementioned aerospace applications [12, 63-65]. For machined L-PBF parts with heat treatment to mitigate residual stress, the process-induced volumetric defects are the most significant factor affecting the fatigue life of the L-PBF parts, since cracks initiated from those defects can lead to the fatigue failure of the L-PBF parts [44, 50, 61, 65-67]. More specifically, positions, sizes, and morphologies of the defects play important roles in the initiation and propagation of the cracks [44, 51, 68-70]. For example, large and irregularly shaped defects can easily act as crack initiation sites by inducing high stress concentrations [44, 45].

Presently, photomicrography and tomography have been widely used in AM domain to characterize the defects (e.g., underfill or overfill on surfaces of the FFF parts and volumetric defects in the L-PBF parts) for process optimization and quality control. For instance, an optical microscope (OM) has been applied for surface analysis in the FFF process [21, 22, 71, 72]. The OM (also known as the light microscope) utilizes visible light and a group of lenses to generate magnified images of a sample in the focal plane[73, 74] with a common magnification range of 10X~200X for capturing the contrast detail from most surfaces [75, 76]. Besides, scanning electron microscope (SEM), a type of electron microscope, has been utilized for fracture analysis of the L-PBF parts [77-79]. The SEM can produce enlarged images of fracture surfaces of the parts with superior resolution and depth of field to reveal the topographical features on the fracture surfaces enabled by the electrons with small wavelengths [77, 78, 80]. Lastly, X-ray computed tomography (XCT) scanning has been commonly used to inspect the defects in the L-PBF parts for defect and fatigue analysis. Such a technique can inspect the defects non-destructively by measuring the absorption differences of penetrable X-rays on the L-PBF parts and reconstructing three-dimensional (3D) models of the parts to inspect the internal volumetric defects [81-84].

With the rising data availability in AM domain from various sources (e.g., photomicrography and tomography) and exponential development in computing infrastructure, the data-driven and programmed algorithm-based machine learning (ML) has become an increasingly influential candidate for process optimization and quality prediction of various AM technologies by modeling the process-structure-property-performance (PSPP) relationships [29, 85, 86]. It can efficiently recognize data patterns, extract insights, and establish high-accuracy predictive models from historical data, thus being widely used for data analysis and decision-making [87-90]. It trains surrogate models using algorithms to approximate the PSPP relationships of the complex AM process (involving multiscale multi-physics processes), which cannot be fully understood so far, in a data-driven manner based on historical data. Moreover, compared to other approaches, such as experimental designs and computational simulations, ML modeling has lower experimental and computational costs by applying those computationally inexpensive algorithms [91].

1.2 Research contributions

According to the background in Section 1.1, this dissertation has three specific tasks to achieve process optimization and quality prediction for the FFF and L-PBF processes by developing novel integrated ML-based methodologies. By fulfilling these three tasks, the research contributions of this dissertation are highlighted in this section.

1.2.1 Process optimization for FFF with novel materials design

Besides process optimization, novel material designs are another important aspect of high-quality FFF fabrications by enhancing the properties of currently used materials. Among the commonly used polymer filaments in FFF, ABS is an excellent material for easy extrusion and accurate printing due to its amorphous characteristic, low glass transition temperature, and small shrinkage ratio during cooling [92]. This material has also been used for FFF-fabricated PPE and medical devices, such as forehead bands for face shields [93] and splitters of the ventilators [94]. However, the inferior mechanical properties of ABS (e.g., tensile strength) can negatively affect the performance of FFF parts in these safety-critical and load-bearing applications [95]. Therefore, developing new nanocomposites to improve mechanical and thermal properties is imperative for further adoption of the FFF process.

Nonetheless, creating a new nanocomposite with successful FFF manufacturing remains challenging. Materials composition and FFF process parameters (e.g., extruder temperature, print speed, and layer thickness) interacted during fabrication, affecting the quality and properties of the final parts, as shown in Figure 1(c). Fabrication under nonoptimal process parameters for certain materials composition can lead to various defects (e.g., voids, underfill, overfill, rough surface) on the FFF parts [96]. In this case, it is requisite to involve the materials composition in the process optimization for fabricating high-quality FFF nanocomposite parts.

The first contribution of this dissertation is that a nonparametric Bayesian framework is developed to simultaneously achieve composition and FFF process parameter optimization for fabricating FFF parts with optimal quality. The proposed framework can identify the critical process parameters, decipher composition-process-property relationships by investigating the impact of materials composition and process parameters and their interactions on the quality of FFF parts, and finally discover the optimal fabrication conditions for the desired product quality.

1.2.2 Defect classification for L-PBF

An efficient and accurate way to classify the defects in the L-PBF process is by utilizing the distinct morphology of each defect type. We specifically focus on data that can be obtained by X-ray Computed Tomography (XCT) to explicitly account for the significant (and often prohibitively large in practice) cost of high-resolution XCT (HR-XCT) scanning [97]. It is broadly agreed that KHs are large, near-spherical (more precisely, keyhole-looking) defects that occur when the excessive energy input vaporizes the metal near the bottom of the melt pool [39, 47, 98, 99]. LoFs, on the other hand, are irregularly-shaped, elongated, and crack-like defects that occur when insufficient energy input fails to fully melt the powder between the adjacent scan tracks of the laser beam or layers [39, 47, 48, 100-102]. GEPs are the smallest and most spherical defects among all three types of defects [39, 42], caused by a small amount of gas – either presented originally in the powders or generated in the printing – trapped in the parts. The GEPs are unpreventable even with the optimal energy input. These different morphologies and sizes of the defects can effectively assist in distinguishing different defect types. The size, shape, and location of volumetric defects are known to influence the fatigue strength and the scatter in fatigue life [44, 103]; therefore, the classification of such defects can help determine their effect on the fatigue performance of the part [104].

The sizes and morphologies of defects can be obtained from XCT scans of the L-PBF parts. Some 3D features of the defects, such as dimensions, volume, and surface area, can be directly measured from the XCT scans. Furthermore, these 3D features can be used to derive other features that describe the defects' morphologies for defect classification.

The second contribution of this dissertation is that a machine learning-based framework is proposed to classify the defects in the L-PBF parts with high efficiency and accuracy based on the morphologies and sizes of defects extracted from XCT scanning, primarily focusing on using the XCT scanning with low resolution, which has a reduced scanning time. The classification results showing the types of defects can be used as an effective method to identify and improve the quality of fabricated parts by the L-PBF process.

1.2.3 Critical defect identification for L-PBF

Three-dimensional (3D) features characterizing the positions, sizes, and morphologies (e.g., spatial distribution, volume, and sphericity) of the volumetric defects can be extracted from non-destructive X-ray computed tomography (XCT) [81-84, 105] to evaluate the significant roles of the defects in the fatigue life of the L-PBF parts. However, critical defects (i.e., the defects at the fracture origin), which are more influential to the fatigue life of the L-PBF parts than other defects, cannot be specifically identified among numerous volumetric defects in the XCT scanned areas. On the other hand, critical defects can be observed on the SEM-based fracture surfaces of the L-PBF parts [77-79]. Some two-dimensional (2D) features (e.g., distance from the surface, area) of the critical defects can be extracted from their contours outlined on the fracture surfaces, which provide useful information for identifying the matches to the critical defects among the volumetric defects in the XCT scans.

The third contribution of this dissertation is that a cross-dimensional (3D/2D) defect matching process is developed and applied to identify the matches to the critical defects among the numerous 3D volumetric defects in the XCT scans based on the defect features extracted from the 2D fractography images. Identifying the match to the critical defect not only reveals the important features of the critical defect, which lead to the variation in the fatigue life of L-PBF parts, but also opens the possibility of critical defect identification and fatigue life prediction non-destructively.

1.3 Dissertation organization

The rest of this dissertation is organized as follows. Related literature regarding process optimization and quality prediction of FFF and L-PBF processes are reviewed in Chapter 2. Chapter 3 presents the developed nonparametric Bayesian framework integrating the nanocomposite design and FFF process parameters for process optimization of the FFF fabricated ABS/graphene nanocomposite parts. The proposed machine learning-based framework to use the augmented LR XCT scanning data for efficient and accurate defect classification of the L-PBF process is elaborated in Chapter 4. Chapter 5 introduces the proposed cross-dimension defect matching process to identify the matches to the critical defects among the volumetric defects for the L-PBF parts. Chapter 6 summarizes the contributions and conclusions of this dissertation and puts forward the potential future research works.

2 Literature review

As introduced in Chapter 1, this dissertation aims to achieve process optimization and quality prediction for the FFF and L-PBF process through ML modeling based on micrographic and tomographic data. In this chapter, the literature related to this is reviewed and organized into four sections: (1) an overview of process optimization to achieve high-quality FFF and L-PBF fabrication; (2) an overview of quality prediction for FFF and L-PBF processes regarding defect analysis and fatigue life prediction; (3) a summary of ML applications for the FFF and L-PBF processes; and (4) an introduction to micrographic and tomographic analysis for the FFF and L-PBF processes.

2.1 Process optimization for FFF and L-PBF

Process parameters of the FFF and L-PBF processes impact the part quality and properties. Many research efforts have been exerted on investigating the effects of process parameters on a variety of quality and properties of fabricated parts, such as surface quality, geometry accuracy, density, and mechanical properties [24, 96, 106-110]. Specifically, Design of Experiments (DoE) is an efficient procedure for planning-controlled experiments so that the data can be efficiently collected and analyzed to yield statistically valid conclusions about the impacts from process parameters of the FFF process (e.g., extrusion temperature, filament feed rate, flow rate, layer thickness, print speed) and L-PBF process (e.g., laser power, scanning velocity, hatch distancing, layer thickness, scan strategies, build orientation). Such conclusions are valuable for understanding the FFF and L-PBF physics and making reliable predictions about FFF and L-PBF process states and part quality.

For instance, Anitha et al. [24] discovered that the road width, layer thickness, and extrusion speed were statistically significant contributors to the surface roughness (R_a) of FFF parts by using a Taguchi (L18) design. Rao et al. [96] applied a factorial experimental design with varying process parameters of an FFF process (such as extruder temperature, filament feed rate, flow rate, and layer thickness) to quantify their main effects and interactions on surface finish. They observed the best surface roughness (R_a) was obtained at a feed/flow ratio of 1.0 to 1.2, a layer thickness of 0.20 mm, and an extruder temperature of 237.5~245°C. Peng and Wang [110] discussed the effect of extrusion temperature. They found that a low nozzle temperature (e.g., below 220°C) for melting the ABS plastic filament would lead to poor layer adhesion and extruder clogging. The authors also made observations regarding feed rate and flow rate settings, noting that part defects were minimized when their ratio approached one. Gurrala and Regalla [7] designed and implemented a minimum of 20 experiments to investigate the impact of process parameters (model interior, horizontal direction, and vertical direction) on the geometry accuracy of FFF parts. Analysis of variance (ANOVA) was used to verify that all three parameters were statistically significant on the part geometry accuracy with the collected experimental data. Then a regression model was built to predict the geometry accuracy from these process parameters. Similar research was done by Nancharaiah [109], where a full factorial design and ANOVA were used to verify the significant impact on the printing duration from layer thickness, air gap, and raster angles. Moza et al. [108] used a Taguchi L9 (3×4) design and ANOVA to verify the effects of printing material, infill rate, the number of shells, and layer height on the dimensional accuracy of FFF parts.

For polymer nanocomposites, Cantrell et al. [106] investigated the extent of anisotropy present in FFF parts with ABS and polycarbonate materials and the impact on the tensile and shear behavior of the parts. Experiments were implemented by varying raster ([+45/-45], [+30/-60], [+15/-75] and [0/90]) and build orientations (flat, on-edge and up-right). The results showed that raster and build orientations had negligible effects on Young's modulus or Poisson's ratio in tensile specimens, but raster orientation in the flat build samples revealed anisotropic behavior in specimens.

Aboulkhair et al. [111] investigated the operating windows of parameters (scanning velocity, hatch distancing, laser power, and scanning strategy) required to produce high-density parts from AlSi10Mg alloy using L-PBF. Through the window of process parameters, the optimal combination was found to be a velocity of 500mm/s, hatch distancing of 50μm, laser power of 100W, and using the pre-sinter scan strategy, leading to the highest relative density of 99.77 ± 0.08%. Read et al. [112] investigated the influence of process parameters (i.e., laser power, scanning velocity, hatch spacing, and island size) on the porosity development in the L-PBF AlSi10Mg parts based on twenty-seven specimens fabricated under different parameters combinations through a fractional factorial design. The ANOVA found that either decreasing the laser power or increasing the scan speed could result in increased porosity. Similarly, Shah and Dey [113] employed the Taguchi design and ANOVA to investigate the effects of process parameters (laser power, scanning velocity, and hatch distancing) on the density and ultimate tensile strength of L-PBF AlSi10Mg parts with nine experimental runs. The hatch distancing was found to be the most impactful on density, while the laser power had the most critical effect on ultimate tensile strength. The optimal density and ultimate tensile strength can be simultaneously achieved with a scanning speed of 1200mm/s, hatch distancing of 0.15mm and laser power of 330W. Moreover, Sun et al. [114] studied the impact of four process parameters (i.e., laser energy density, hatch distancing, powder layer thickness, and scanning strategy) on the density of L-PBF Ti6Al4V (Ti64) parts using the Taguchi design with sixteen experimental runs. The ANOVA result showed that the layer thickness and hatch distancing were the most and least impactful on the part density.

2.2 Quality prediction for FFF and L-PBF

Defects in the FFF (i.e., under-fill and over-fill) and L-PBF (i.e., KH, LoF, and GEP) parts can negatively impact the part quality and properties. Each type of defect is formed under different fabrication conditions. Accurately classifying the defect types contributes to identifying and rectifying the fabrication conditions for defect mitigation and quality improvement of future fabrication. In this case, many research efforts [21, 40-43, 96, 115-121] have been devoted to defect classification for the FFF and L-PBF processes.

Many studies [21, 96, 119-121] identify the defects in the FFF process using either physical sensing-based approaches or image-based sensing technologies [21]. Prahalad et al. [96] detected the defects occurring in the FFF process by monitoring the temperature and vibration of the extruder and bed, melt pool temperature with a custom multisensory measurement system consisting of thermocouples, accelerometers, and an infrared temperature sensor. Wu et al. [120] distinguished the defects and normal printings using acoustic emission sensors to detect the stress waves generated from the emission source, such as defect formations. Kim et al. [119] used the current sensors to detect the material deposition status of the FFF process based on the hypothesis that the nozzle’s extrusion pressure was related to the motor current of the feed motor, which could be used to diagnose the nozzle status. Liu [21] used the gray level co-occurrence (GLCM) matrix as the textural representation of the image data collected by the optimal microscope (OM) to identify different types of surface defects in the FFF process. The GLCM effectively described the spatial correlation of the patterns by printing tracks, thus being a key feature in distinguishing different types of defects from normal printings.

Process maps are a commonly used method to classify different types of defects based on the effect of the main process parameters of the L-PBF process [40, 42, 43, 115, 116]. As mentioned above, the generation of different types of defects is significantly impacted by the energy input; meanwhile, the energy input is stated to be controlled by four main process parameters. A volumetric energy density E_V (J/mm^3) [39-41] is defined to qualify the magnitudes of the energy input as a function of the process parameters:

$$E_V = \frac{p}{v \cdot h \cdot t} \tag{1}$$

where p is the laser power (W), v is the scanning velocity (mm/s), h is the hatch distancing (mm), and t is the layer thickness (mm). Excessive energy input leading to KHs can be caused by high laser power, low scanning velocity, small hatch distancing, or small layer thickness. On the contrary, insufficient energy leading to the LoFs can be caused by low laser power, high scanning velocity, large hatch distancing, or small layer thickness. In this case, Zhu et al. [43] developed process maps to fabricate a nearly full-density (relative density above 99%) L-PBF nitinol part by identifying proper combinations of four process parameters. Gordon et al. [42] generated a process map to identify the boundaries of KHs and LoFs in a laser power-scanning velocity (*p*-*v*) space of the L-PBF Ti-6Al-4V (Ti64) parts. Tapia et al. [115] and Meng et al. [116] distinguished keyhole mode and conduction mode regions in the *p*-*v* space of the L-PBF parts fabricated with stainless steel 316L to identify KHs. However, utilizing the process map approach, all the defects in one L-PBF part are classified by the process parameters instead of being individually inspected, leading to a possible high misclassification rate, especially in identifying the GEPs, which can co-occur with KHs and LoFs.

Other studies [41, 42, 117, 118] classify different types of defects in the L-PBF process primarily depending on defect length. For instance, Gordon et al. [42] observed that the lengths of KHs and LoFs were larger than 40μm, while the lengths of GEPs were smaller than 20μm. To further distinguish KHs and LoFs, they stated that KHs were spherical and LoFs were nonspherical. Their findings were based on the L-PBF Ti64 parts fabricated with laser power varying from 100W to 370W and scanning velocity from 400mm/s to 1500mm/s. Kasperovich et al. [41] summarized that the lengths of LoFs ranged from 10μm to more than 200μm, and the lengths of KHs were larger than 100μm in the L-PBF Ti64 parts fabricated with laser power varying from 100W to 200W and scanning velocity varying from 200mm/s to 1100mm/s. Zhang et al. [117] observed that both LoFs and KHs had lengths ranging from 10μm to more than 100μm, and GEPs had lengths shorter than 10μm from the defects in the L-PBF parts fabricated with stainless steel 316L. Snell et al. [39] concluded that the lengths of LoFs are larger than 31μm and the lengths of KHs are roughly two times larger than LoFs to distinguish the LoFs and KHs in the L-PBF parts fabricated with Inconel 718. However, the inconsistency of the defect lengths used for defect classification in various studies due to different materials and process parameters might lead to a discrepancy in the results. Therefore, it is beneficial to include more features (e.g., morphological features) of defects for more consistent defect classification [97]. Furthermore, it would be useful to have a technique that does not depend on fixed thresholds for classification.

Many research efforts have been devoted to studying the quantitative relationship between different defect features and the fatigue life/strength of the L-PBF parts. Some [45, 66, 79, 122, 123] utilized 2D defect features of the critical defects for fatigue life/strength prediction. For instance, Beretta and Romano [66] and Poulin et al. [122] used Murakami's parameter, Stress Intensity Factor (SIF) estimated by the Linear Elastic Fracture Mechanics (LEFM), and

Murakami's shape factor (0.5 for internal defects and 0.65 for surface and near-surface defects) to calculate the fatigue strength of the L-PBF parts fabricated with AlSi10Mg and Inconel 625, respectively by the El-Haddad's model [124]. Masuo et al. [123] and Yamashita et al. [45] estimated the fatigue limit of the Ti6Al4V (Ti64) and Ni-based Superalloy 718 L-PBF parts, respectively, as a function of the effective area parameters of the critical defects and the Vickers hardness of the materials.

Some studies [50, 125, 126] used 3D defect features extracted from the XCT scans for fatigue life prediction of the L-PBF parts. Hu et al. [50] discovered the quantitative relationship between the equivalent diameters and distances from the surface of the volumetric defects and the fatigue life of the L-PBF Ti64 parts by the Fatigue Crack Growth model [50, 68]. They found that a volumetric defect with either a larger equivalent diameter or a smaller distance from the surface can lead to shorter fatigue life of the parts. Moon et al. [126] discovered strong negative linear correlations between some 3D defect features (e.g., sum volume of surface defects, density of surface defects, and mean surface defect volume) and high cycle fatigue life of the L-PBF Ti64 parts.

It is noticed that few studies have combined the 2D and 3D defect features of the critical defects for fatigue performance analysis of the L-PBF parts because of the limited access to specific 3D features of the critical defects. Some studies [125, 127, 128] tried to use defects with the largest sizes (e.g., volumes or major axis lengths) to represent the most detrimental ones in the fatigue performance analysis. However, it is found in [129] not necessarily the largest defects became the critical defects.

2.3 ML applications for FFF and L-PBF

Many studies [112, 130-134] used ML to model the relationships between the porosity (the ratio between the total volume of all defects and the volume of an L-PBF part [135]) and the process parameters of the L-PBF parts. For instance, Read et al. [112] used a polynomial regression model to build the relationship between the porosity and process parameters (i.e., laser power, scanning velocity, and hatch distancing) and fabricated low porosity (0.29%) L-PBF parts with the optimal process parameters found by their model. Tapia et al. [131] built a Gaussian process regression (GPR) model to predict part porosity based on laser power and scanning velocity and achieved a low mean absolute square error (below 20%) between the predicted porosity values and actual observations. Ye et al. [133] conducted an iterative Bayesian optimization established on a GPR model to search for the optimal process parameters in the *p-v* space and reduced the porosity of L-PBF parts by 0.6%. Liu et al. [134] developed a Gaussian process-based layer-wise porosity modeling to quantify the spatial distribution of porosity in previous layers and predict the positions, sizes, and numbers of the pores in consecutive layers. They achieved an F-score of 0.86 to identify the porosity in 30 consecutive layers based on the six previous ones.

ML has been widely used as an automatic process in many studies [21, 26, 96, 136, 137] to identify different defects in the FFF process with high accuracy. For instance, Liu et al. [21] used various classifiers (i.e., Support Vector Machine, linear discriminant analysis, naïve Bayesian and k-nearest neighbor) to distinguish defects (i.e., over-fill and under-fill) from normal printings in the FFF process based textural features of the FFF parts. The classification results achieved a high accuracy of 85% and were incorporated into a closed-loop feedback control system to mitigate the defects by adjusting process parameters (e.g., flow rate, fans cooling rate) in the FFF fabrication. Narayanan et al. [26] separately applied a Support Vector Machine (SVM) and

Convolutional Neural Network (CNN) classifiers to achieve an accuracy of 98.2% and 99.5%, respectively, to classify under-fill and over-fill based on geometry images of the FFF parts. Wu et al. [136] utilized different regression models (i.e., random forest, Support Vector Regression, ridge regression, and least absolute shrinkage and selection operator) to predict the surface roughness of the FFF parts online by the sensor data (i.e., temperature and vibration of the extruder and build plate) with low relative error rate to 4%. Prahalad et al. [96] proposed a nonparametric Bayesian Dirichlet process mixture model to facilitate a sensor data-driven (including thermocouples, accelerometers, and an infrared temperature sensor) defect detection system, which enabled a real-time identification of FFF defects with accuracy approaching 85%. Delli et al. [137] trained an SVM classifier to distinguish normal printings and defective parts based on ex-situ images of the FFF parts and correctly identified a test sample with their trained SVM classifier.

Several pioneering studies [39, 97] applied ML to build the relationship between defect features and types for defect classification in the L-PBF process. Snell et al. [39] used *k*-means clustering models to classify large amounts (over 20,000) of defects into KHs, LoFs, and GEPs using three 2D morphological features (i.e., length, sphericity, and aspect ratio). However, these three morphological features cannot fully distinguish all the defects with unsupervised learning; roughly half of the defects were unable to be classified into any defect types. Poudel et al. [97] applied an Artificial Neural Network (ANN) model to establish the relationships between the defect types and some 3D morphological features (e.g., elongation, aspect ratio, sphericity) extracted from the HR-XCT scans for defect classification. Their ANN model achieved an overall accuracy above 99% to classify approximately 2000 defects into their types. Cui et al. [138] trained convolutional neural network models to classify defects by 2D image features (e.g., edges, shapes) of the defects directly and achieved an accuracy of 92.3% from 4140 images. Other studies [139, 140] utilized ML to predict occurrences of defects from the in-situ monitoring data. Bartlett et al. [139] trained naïve-Bayes classifiers to identify the nonoptimal energy input-induced KHs or LoFs by the irregular surface topology of each powder layer extracted by an optical camera and achieved an average accuracy of 72%. Khanzadeh et al. [140] applied a self-organizing map to distinguish the defects in the L-PBF process by their abnormal melt pool signatures, and their model achieved an accuracy of 63% in predicting the occurrences and positions of defects. Garg et al. [141] developed multi-gene genetic programming (MGGP) to ensemble ANN, Bayesian classifier, and SVM algorithm to identify the defects in L-PBF parts with the combination of three process parameters (i.e., layer thickness, laser power, and scanning velocity). Their models showed that laser power and scanning velocity were the most impactful to cause the defects.

Some studies [142-145] applied ML modeling to directly connect the process parameters (e.g., laser power, scanning velocity) and the fatigue life of the L-PBF parts. For instance, Zhan et al. [142] separately trained ANN, random forest (RF) and SVM models to predict the fatigue life of L-PBF fabricated SS316L, AlSi10Mg, and Ti64 parts based on the process parameters (i.e., laser power, scanning velocity, hatch distancing, and layer thickness) and fatigue loads (i.e., maximum stress and stress ratio) using simulated training data. Compared to the experimental fatigue life, most of their predictions for three different materials are within the three-error band (i.e., predicted fatigue life is between one-third and three times of the experimental values). Zhang et al. [143] built a “process-based” (predictors including laser power, scanning velocity, and post-processing conditions) ANN fatigue life prediction model for the L-PBF SS316L parts and observed that all the predictions were within the two-error-band of the experimental values. Zhang et al. [145] predicted the fatigue life of L-PBF SS316L under high (296MPa) and low (197MPa) stress amplitude by a second-order polynomial equation of laser power and scanning velocity.

Their predictions achieved R^2 values of 0.954 and 0.584 for high and low-stress conditions, respectively.

Besides, other studies [125, 128, 146-148] utilized ML for fatigue life prediction of the L-PBF parts using defect features and achieved high accuracy. Li et al. [146] trained a Support Vector Regression (SVR) model to predict the fatigue life of the L-PBF parts based on the size, morphology, and location of the critical defects (i.e., the defects imitated crack propagation to cause the fatigue failure of the L-PBF parts) extracted from the fracture surfaces. Their SVR model with optimized hyperparameters achieved a low mean absolute percentage error (MAPE) value of 0.11 for fatigue prediction. Similarly, Bao et al. [125] applied SVR to conduct the fatigue life prediction of the L-PBF parts by the location, size, and morphology of the top twenty defects with the largest volumes in each part. Their prediction achieved a high R2 value of 0.99 compared to the parts' experimental fatigue life. Salvati et al. [128] developed a Physical-Informed Neural Network (PINN) model to predict the fatigue life of the L-PBF parts based on size, location, the morphology of defects, and fatigue testing parameters. Their PINN model used weighted prediction error of Neural Network (NN) and differences between NN predicted fatigue life and estimated fatigue life using E739 ASTM standard as the loss function to update bias and weights of the NN, which improved the prediction accuracy than directly using the NN for fatigue life prediction. Li et al. [147] ran the Monte Carlo simulations to generate a large dataset consisting of defect, size, depth, location, build orientation, and fatigue life of the L-PBF parts and used a NN model to predict fatigue life with high accuracy ($R^2 \geqslant 0.97$).

2.4 Micrographic and tomographic analysis for FFF and L-PBF

In many studies [21, 22, 71, 72] investigating the surface quality of FFF parts, the optical microscope (OM) has been applied to collect the image data for surface analysis. For instance, Liu [21] used OMs to collect the image data of the top surface of FFF parts in-situ and extracted textural features from the collected image data for defect classification. Rashed [22] utilized OMs to obtain the root mean square roughness of the surface of the FFF parts ex-situ for process optimization. Zhang et al. [72] used the OMs to observe and compare the grain orientation of the FFF and L-PBF Ti64 parts.

Among existing studies, various features are extracted from SEM-based fractography (i.e., 2D features of the critical defect) and XCT scans (i.e., 3D features of volumetric defects) to characterize volumetric defects. 2D defect features characterizing the sizes, morphologies and positions of the critical defects can be extracted from the SEM-based fractography images of fracture surfaces [45, 79]. For instance, Murakami's parameter ($\sqrt{area}$) [149], representing the square root of the projected area of a volumetric defect on a plane normal to the stress, was commonly used to quantify the sizes of the critical defects based on their contours on the fracture surfaces [66, 122, 150]. Yamashita et al. [45] and Masuo et al. [123] developed an effective area parameter ($\sqrt{area_{eff}}$), which measured the sizes of surface or near-surface critical defects through a polygon surrounding those defects and their ligaments to the surface, to reveal the higher risk of the surface or near-surface critical defects to the fatigue life of the L-PBF parts than the internal ones. Li et al. [79] utilized four 2D morphological features (e.g., circularity, eccentricity, solidity, and extent) to quantify the irregular shapes of the critical defects. Many studies [45, 79, 123, 128] used distance from the surface to locate the positions of the critical defects on the fracture surfaces. However, only using distance from the surface cannot provide precise position information for the critical defects.

Compared to the fractography, the non-destructive XCT scanning has four major advantages, such as (1) keeping the L-PBF parts intact for future processes (e.g., heat treatments, shot peening, fatigue testing) [81, 83]; (2) eliminating the part preparation procedures (e.g., grinding, and polishing processes, which may change the morphologies and sizes of defects owing to metal smearing) [151]; (3) examining the entire 3D volume of the L-PBF parts (compared to fractions of the parts with 2D planes); (4) describing 3D features of the defects (e.g., spatial distribution, volume).

Given those advantages, many studies used XCT scanning to obtain 3D defect features to characterize the sizes, morphologies, and positions of the volumetric defects. For instance, the sizes of the volumetric defects can be represented by their equivalent diameters [128], major axis lengths [129, 152, 153], volumes [125], or projected areas on XY planes and YZ planes [126] from the XCT scans. Arun et al. [153] and Ye et al. [152] utilized up to eight 3D morphological features (e.g., elongation, flatness, sphericity, solidity) extracted from the XCT scans to distinguish different shapes of the volumetric defects. Moreover, the X-, Y-, Z-locations of the volumetric defects can be obtained to demonstrate their precise positions in the XCT scanned areas [154].

Meanwhile, since the 3D features were available for all the volumetric defects in the XCT scanned areas, Muhammad et al. [155] and Shen et al. [156] obtained the volume fractions and total defect numbers to inspect the quality of the L-PBF parts. Maskery et al. [151] obtained the morphologies and sizes of the volumetric defects in the XCT scanned area and accordingly refined the process parameters to mitigate the defects with large volumes and irregular shapes. du Plessis et al. [157] utilized XCT scans to investigate the effect of hot isostatic pressing (HIP) on L-PBF parts non-destructively. They observed that the HIP reduced the average volumes and lengths of the defects in the Ti64 parts. In another study to investigate the effects of shot peening (SP), Damon et al. [154] used XCT to obtain the spatial distribution and volumes of the defects in the L-PBF AlSi10Mg parts before and after SP and concluded that most of the near-surface defects were healed with their volumes decreased. Other studies [46, 55, 118, 140] obtained the volumes and positions of all defects in the XCT scanned areas and used them as ground truth to verify their defect prediction models. Generally, the HR-XCT scanning with a small voxel size (0.65~2.1μm) was used to obtain precise morphologies and sizes of the defects [42, 46, 151, 158, 159]. However, the HR-XCT needs a long scanning time and may only allow for a relatively small scanned volume. For instance, in [151], it took approximately 32 hours for an HR-XCT to finish scanning a region of 125mm^3. As a result, HR-XCT could be prohibitively costly and inefficient for analyzing defects in many practical applications.

Some studies [41, 160, 161] related the 2D defect features from the fractography and 3D defect features from the XCT scans to inspect the quality of the L-PBF parts with different fabrication conditions and post-processing treatments. For instance, Kasperovich et al. [41] compared 2D defect features (i.e., area and circularity) of the defects on multiple cross-sections and 3D defect features (i.e., volume and sphericity) of the L-PBF parts fabricated with different energy density levels. They observed similar distributions in the circularity and sphericity, especially for the L-PBF parts fabricated with excessive energy density levels. Meanwhile, the area fraction and volume fraction from the same L-PBF parts were in good argument to show close percent porosity. Benedetti et al. [161] also found that the percent porosity values estimated by the sum volume of the 3D defects lay within the error band of those estimated by the sum area of the 2D defects for as-built, shot peened, and hot isostatic pressing treated L-PBF parts. Sanaei et al. [160] observed that decreases both in the 2D defect features (i.e., aspect ratio and circularity) and

3D defect features (i.e., aspect ratio and sphericity) were typically along with the increases in the sizes of defects, which can induce high-stress concentration for crack initiation. They also concluded that by enough cross-sections, 2D defect analysis could reveal a similar spatial distribution of the defects to 3D analysis. Since the 2D and 3D defect features used for comparisons could be extracted from differently sampled defects in the L-PBF parts, these studies did not investigate the relationship between 2D and 3D defect features of the same defects by identifying the 3D counterparts of the 2D defects.

3 Nonparametric Bayesian framework for material and process optimization with nanocomposite fused filament fabrication

3.1 Introduction

Developing new nanocomposites to enhance the mechanical and thermal properties of ABS material is critical for further adoption of the FFF in safety-critical tasks. In recent years, polymer nanocomposites have remained a heated research topic due to the potential property improvement in host materials by adding nanomaterial fillers (e.g., carbon nanotubes, nanowires, and nanoparticles) [106, 162-170]. They become functional and structural materials in various industries, including automobile, aerospace, packaging, and construction [171].

With a rigid planar nanostructure of single-layer carbon atoms arranged in a hexagonal crystal lattice, graphene is a suitable filler to provide polymers with many functional characteristics, such as unparalleled thinness and strength, large specific surface area, high elasticity, superior chemical stability, excellent thermal and mechanical properties [171]. It is found that adding graphene into ABS enhances its tensile strength, bending strength, elongation-to-failure, and storage modulus [106, 162, 166, 170, 172] and is promising for different functional and structural applications.

In this case, the research in FFF with nanocomposites has gained tremendous traction among material scientists and practitioners for its promising potential in customizing complex structural parts at a low cost with desktop FFF machines. Different research groups have dived into the design and fabrication of graphene-based polymer nanocomposites with FFF processes. For instance, Wei et al. [169] presented one of the first attempts to print graphene-enhanced polymer filament using FFF directly and demonstrated the graphene composite with ~5.6wt.%

graphene could be successfully 3D-printed. Dul et al. [173] successfully created filaments for FFF by melting 4wt.% graphene nanoplatelets in an ABS matrix to improve ABS's tensile modulus and reduce the thermal dilation coefficient. Sakunphokesup et al. [174] compared three techniques, i.e., dry mixing, solvent mixing, and coagulation techniques, to prepare ABS/graphene nanocomposites for FFF regarding tensile strength and elongation at break and Young's modulus. Singh et al. [175] developed an ABS/graphene blended composite feedstock filament for FFF and proved that FFF specimens printed with graphene-blended ABS improved mechanical, thermal, and electrical properties for many engineering applications.

Other research studies [176-181] formulated ABS/graphene filaments for FFF to meet the application requirements by varying the graphene composition in the nanocomposites. These studies have developed novel nanocomposite filaments with improved mechanical properties that potentially benefit the manufacturing industry. For instance, Tambrallimath et al. [179] developed feed materials to FFF by blending different ratios of graphene platelets to two polymers (i.e., polycarbonate and ABS). The addition of graphene platelets resulted in a significant increase in Young's modulus with the highest value of 4.038GPa (with 0.8wt.% graphene). It also increased the glass transition temperature and reduced the mass with the increase of temperature from the thermal analysis. Vidakis et al. [180] developed novel nanocomposite filaments by adding Titanium Dioxide (TiO_2) and Antimony-doped Tin Oxide (ATO) nanoparticles to ABS at various concentrations. They found that TiO_2 filler enhanced the overall tensile strength by 7%, the flexure strength by 12%, and the micro-hardness by 6% compared to unfilled ABS, while for the ATO filler, the corresponding values were 9%, 13%, and 6%, respectively. Vidakis et al. [181] dispersed Zinc Oxide nanoparticles (ZnO nano) and Zinc Oxide micro-sized particles (ZnO micro) into ABS matrices to fabricate FFF filaments. A 14% increase in the tensile strength was shown at 5 wt.%

concentration in ABS/ZnO nano and ABS/ZnO micro compared to ABS. Furthermore, a 15.3% increase in flexural strength was found in 0.5 wt.% ABS/ZnO nano and a 17% increase in 5 wt.% ABS/ZnO micro.

Current research on nanocomposite development in FFF usually fixes the FFF process parameters when changing the mixture proportion of ABS and graphene. Therefore, the impact of FFF process parameters on the properties and quality of printed FFF parts with ABS/graphene nanocomposites is not fully investigated. Since the composition of nanocomposites and FFF process parameters are intertwined, they impose critical challenges in developing nanocomposite materials and achieving successful fabrication simultaneously for practical applications.

The goal of this chapter is to develop a nonparametric Bayesian framework for surface quality prediction with different graphene compositions and FFF process parameter optimization to achieve the optimal quality of fabricated parts. This framework is centered on the Gaussian process (GP), which acts as a prior for the regression surrogate model in a nonparametric form [182-185] and bypasses the complexity of modeling the relationships among process parameters and their effects on part quality. Moreover, GP can leverage its covariance structure to incorporate the correlations among various predictors, implying that similar fabrication conditions would lead to similar product quality and achieve flexible modeling even with a small amount of experimental data in a variety of applications [131, 134, 186, 187]. Therefore, this framework can identify the critical process parameters, decipher composition-process-property relationships by investigating the impact of graphene composition and process parameters and their interactions on the quality of FFF parts, and finally discover the optimal fabrication conditions for the desired product quality. It will bridge the enduring gaps and unify materials design and process optimization. The outcomes from this study could accelerate nanocomposite design and fabrication with FFF, reduce the waste in materials, cost, and time, and facilitate innovations in functional and structural applications of ABS/graphene nanocomposites in different fields.

The rest of this chapter is structured as follows: the experimental trials and preliminary results of ABS/graphene nanocomposite synthesis and FFF manufacturing are introduced in Section 3.2; the proposed nonparametric Bayesian framework with its major three components is detailed in Section 3.3 to achieve nanocomposite design and FFF process optimization; it is further corroborated with a case study in Section 3.4; finally, conclusions and future work for FFF ABS/graphene nanocomposites are presented in Section 3.5.

3.2 Experimental equipment and preliminary experimental trials

3.2.1 Experimental equipment

Material preparation and filament production

Graphene nanoplatelets (high purity carbon 99+%, with a thickness of 10~100nm) and ABS pallets (grade Lustron 248), sealed in original packages, were mixed by shaking in a closed container at different loadings of graphene up to 10 wt.%. The mixture was then fed into a twin-screw extruder (Leistritz MIC-18). Using a twin-screw extruder can make sure the blending of ABS and graphene nanoplatelets is homogenous. During filament production, the twin-screw extruder temperature was gradually increased from 170°C to 195°C with constant extrusion speed and feed rate as recommended in [177]. The filaments obtained from the twin-screw extruder were further ground in a pelletizer into small pallets so they could be extruded again using a single screw extruder to extract the filaments with a final diameter of 1.75±0.10mm. The speed of the single screw extruder was set between 40-45 rpm, and the temperature of the two heating zones was between 180~190°C.

After the filaments were produced, we measured the diameter at multiple points along the filaments to ensure that their diameter was within the range of 1.75±0.10 mm and they were ready for printing in an FFF machine. Moreover, the consistency of graphene composition in the filaments was confirmed by thermal gravimetric analysis (TGA) testing. In addition, precautions were taken to further manually examine the filament diameters right before actual printing to ensure the success of part fabrication.

ABS/graphene nanocomposite FFF printing

Hyrel System 30M was used for ABS/graphene nanocomposite rapid prototyping, as shown in Figure 1(a). It is an open experimental platform with easy access to a variety of process parameters. Optimal printing with proper graphene composition can improve the mechanical properties and surface quality of FFF parts with ABS/graphene nanocomposites, as shown in Figure 1(b).

The sketch of FFF extrusion in Figure 1(c) reveals that extruder temperature, print speed, and layer thickness are closely related to heat transfer and materials deposition in FFF, which mainly contribute to product quality; therefore, they were selected as the critical process parameters to be tested and optimized in the study. Other process parameters of the FFF machine were fixed according to the manufacturer’s recommendations, for instance, 85^{o}C bed temperature, 1.75mm extrusion width, rectilinear fill pattern with 100% fill density, 20% infill/perimeters overlap, and 25% fan speed.

Tensile testing and surface imaging for FFF parts

Type-V tensile test specimens, which have a dumbbell shape with a thickness of 3~4mm, as shown in Figure 1, were fabricated by the FFF machine for the tensile test in ASTM D638. An Instron (model 4505) machine was used to test the tensile strength for the printed parts with the elongation speed of 3.5mm/min and the grip GD638-243, following the standard procedure of ASTM D638.

The surface quality of the test specimens was quantified by calculating surface quality values from surface images captured by a digital microscope (Opti-Tek Scope OT-HD, with 200× magnification). The surface quality values were used as the quality indicators for the predictive model and process optimization and are introduced in detail in the following section.

3.2.2 Surface roughness as quality indicators

The surface roughness of FFF parts was chosen as a quality indicator in this work. It can reveal the binding quality of the molten filaments and the defects occurring on the printed parts and has been widely used to indicate printing quality for various FFF materials [24, 188, 189]. Two areal surface quality values, S_a (average surface roughness) and S_q (root mean square surface roughness) [190], are calculated from the surface images as shown in Figure 3 with their pixel intensity values:

$$S_a = \frac{\sum_{n=1}^{N} \sum_{m=1}^{M} |I_{nm} - \bar{I}|}{N \cdot M}$$
$$S_q = \sqrt{\frac{\sum_{n=1}^{N} \sum_{m=1}^{M} (I_{nm} - \bar{I})^2}{N \cdot M}} \tag{2}$$

where N and M define the size of the image, I_{nm} is the intensity value of the pixel at the n^{th} row and the m^{th} column, $n \in \{1,2,\dots,N\}, m \in \{1,2,\dots,M\}$, and $\bar{I}$ is the average intensity value of the image.

It is expected that the surface roughness of FFF parts varies according to different graphene compositions in the filament. The areal surface quality values S_a and S_q can quantify the differences in the surface quality as shown in Figure 3, where FFF parts with different surface quality are captured by using a microscope: (a) smooth surface finish; (b) underfill with voids; (c) overfill with a rough surface.

It is important to note that the surface quality values indicate the relative surface quality among all the FFF parts in this work. With the easy availability of surface images, they are convenient and fast to calculate and compare the surface quality of printed parts in one study. However, when capturing surface images with a microscope, strict controls on potentially impacting factors (such as ambient light) are needed for reliable quantification and comparison. We will discuss some controls in our case study in Section 3.4.

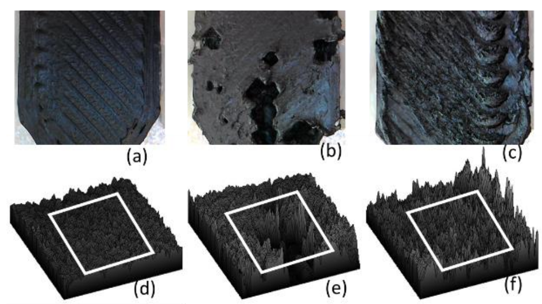

Figure 3 FFF parts with different surface quality: (a) smooth surface finish, (b) underfill with voids, (c) overfill with a rough surface; (d)-(f) the selected areas on the grayscale images for calculating areal surface quality values S_a and S_q, with the pixel intensity values represented in 3D.

3.2.3 Preliminary experimental trials

The preliminary experimental trials revealed that changing graphene composition in the nanocomposite severely impacted the product quality even with the same set of feasible process parameters. As shown in Figure 4, with the same process parameters, the FFF parts with ABS have an acceptable surface quality with only a few voids (Figure 4(a)). However, the FFF parts with the nanocomposite (5wt.% graphene in ABS) suffer from inferior surface quality or even printing failure (Figure 4(b)). Such differences can be attributed to the fact that the original feasible fabrication conditions for ABS are no longer applicable for the nanocomposite due to the high melting point of graphene, requiring an increase in extrusion temperature.

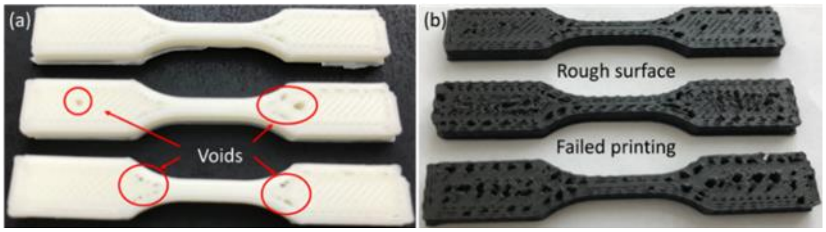

Figure 4 FFF parts under the same process conditions with (a) ABS and (b) ABS/graphene nanocomposite (5wt.% graphene). The fabricated ABS parts in (a) have a smooth surface finish with a few small voids, while the parts with the nanocomposite in (b) show a rough surface and even have failed prints caused by inconsistent extrusion and extruder clogging. The difference could result from a higher melting point after adding graphene.

It is also observed from the experimental results that the improper changes in process parameters without a holistic optimization could further aggravate the inferior quality of the FFF parts. For instance, the decrease of print speed from 20mm/s to 10mm/s, with other process parameters fixed for the ABS/graphene nanocomposite (5wt.% graphene), led to the decrease of material flow rate and the decline of materials deposited on the build platform, consequently, the deteriorated surfaces with large voids, as shown in Figure 5(b). Some parts even failed at the early stage of printing.

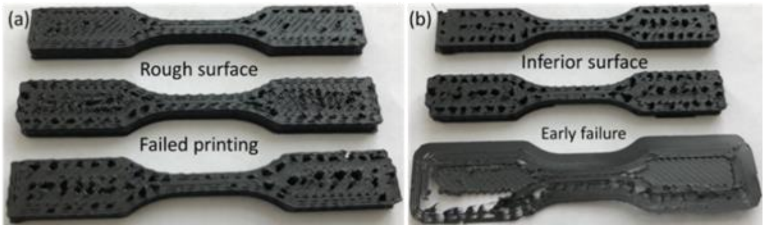

Figure 5 ABS/graphene nanocomposite with 5 wt.% graphene was printed at different print speed: (a) 20 mm/s and (b) 10 mm/s. Printing at a relatively low speed without corrections on other parameters can lead to discontinuous material deposit and aggravation of voids, and inferior surface quality.

By adjusting process parameters for the nanocomposite with 5wt.% graphene, the surface quality of FFF parts was significantly improved, as shown by the FFF specimens in three repeated printing runs in Figure 6. Moreover, the ultimate tensile strength of these FFF parts was about 55MPa in Figure 6, a 25%-50% increase from FFF parts with ABS (reported as 35MPa in a benchmark study from Yayanth et al. [191]). These results emphasized the importance of optimizing process parameters based on the graphene composition in the nanocomposites to fabricate high-quality FFF parts.

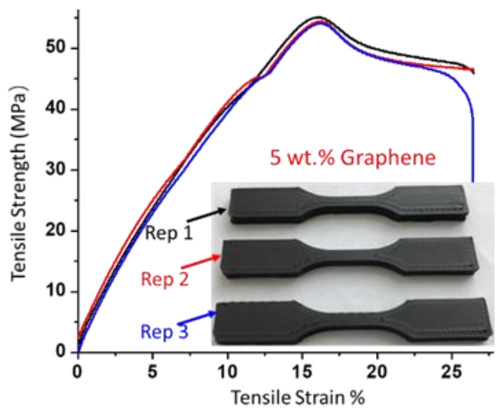

Figure 6 The superior surface quality of three repeated FFF parts with nanocomposite (5wt.% graphene) under a satisfying set of process parameters. The ultimate tensile strength of these FFF parts was about 55MPa, a 25%-50% increase from FFF parts with only ABS.

However, it was time-consuming and inefficient to experiment with many possible combinations of process parameters with different graphene compositions to achieve high surface quality and optimal process parameters through all these experimental trials. Therefore, we aim to leverage and integrate statistics, machine learning, and optimization techniques to model the composition-process-property relationships and optimize them for the ABS/graphene nanocomposite synthesis and freeform fabrication.

3.3 Methodology

In this work, we aim to bridge the existing gaps in designing and fabricating ABS/graphene nanocomposites through FFF by proposing a nonparametric Bayesian framework in a physics-based data-driven manner. It unifies nanocomposite design and part fabrication and simultaneously optimizes graphene composition and process parameters to achieve optimal surface roughness on the fabricated parts. The proposed framework is centered on the Gaussian process for modeling the complex effects and interactions among fabrication conditions on part quality and Bayesian optimization for identifying the optimal graphene composition and process parameters. The overall research methodology is summarized in Figure 7 with the following four basic steps:

Step 1 (Section 3.3.1): Fractional factorial design is used to plan controlled tests to generate experimental data with reduced experimental costs.

Step 2 (Section 3.3.2): Gaussian process regression (GPR) is utilized to model the relationships between process parameters and product quality and achieve accurate prediction by leveraging the correlation among process parameters.

Step 3 (Section 3.3.3): Model agnostic methods are integrated to interpret the results from GPR and understand the impacts of process parameters on product quality.

Step 4 (Section 3.3.4): Bayesian optimization is incorporated to find the optimal process parameters iteratively for achieving the best product quality.

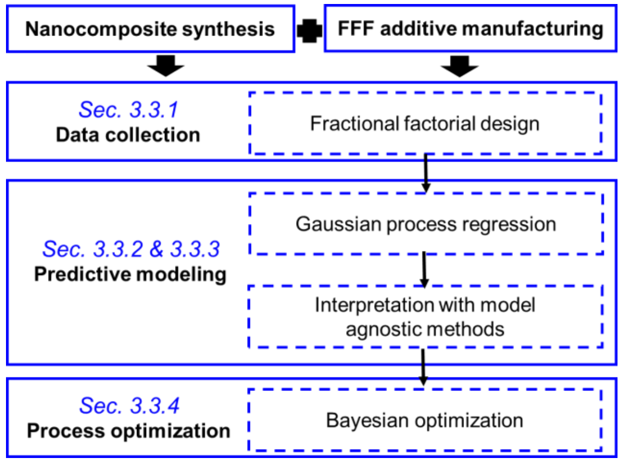

Figure 7 The overall structure of the proposed nonparametric Bayesian framework in quality prediction and process optimization for nanocomposite synthesis and fabrication with FFF.

3.3.1 Factional factorial design

Fractional factorial design, a DoE technique [192], is used to plan and conduct controlled experiments with different experiment conditions for evaluating the effects of FFF process parameters and graphene composition on the surface roughness of FFF parts. A non-regular fractional factorial design with an orthogonal array can efficiently cover the whole design space and produce informative data for analysis. Besides the graphene composition (*G*), three critical process parameters (i.e., extruder temperature (*T*), print speed (*S*), and layer thickness (*L*)) have been proved to have significant impacts on FFF surface roughness [21, 188, 193, 194], and consequently, contributing to a successful FFF printing with ABS/graphene nanocomposites. The identified process parameters and graphene composition are listed in Table 1, as well as their respective levels for the fractional factorial design.

Two graphene composition levels (5wt.% and 10wt.%) are used to investigate the effect of graphene composition on FFF surface roughness. Adding graphene to ABS could change the glass transition temperature (T_g), at which ABS transitions from a rigid glassy state to a fluid state before decomposition [195] since there might be molecular level interactions like π-π stacking between

ABS and graphene and lead to a much higher melting temperature of graphene compared with ABS [196]. Therefore, graphene composition will affect the melting and deposition of nanocomposite filament during the FFF process.

The extruder temperature mainly impacts filament fusing and decomposition throughout FFF and must be correctly configured based on material thermal characteristics [197]. An excessively high extruder temperature (around 250~260ºC) [188] overly fuses the ABS filaments and causes a long deposition time and overflow, while a low temperature leads to incomplete filament fusing and potential extruder blockage. In our experiments, the range of extruder temperature is selected 220~240ºC, according to recommended extruder temperature of the ABS [177, 198].

The print speed affects the filament flow rate in Hyrel System 30M and, consequently, FFF surface roughness. The preliminary experimental result shows that a print speed lower than 20mm/s leads to voids due to an inadequate flow rate, even printing failures on the initial layers; on the contrary, a print speed higher than 40mm/s leads to filament overflow and overfill [21, 188, 199]. We select 30mm/s as the normal print speed in our experiments and 40mm/s and 20mm/s as high and low print speed levels.

Layer thickness defines the resolution of the FFF parts along the building direction (Z-axis). A smaller layer thickness could improve build resolution with finer feature details [188, 199]. A normal layer thickness is selected as 0.2mm in this research with satisfactory resolution and printing time. The high and low levels are selected as 0.3mm and 0.1mm, respectively.

Table 1 The selected graphene composition/process parameters and their respective levels to conduct experimental design.

Factors	Level 1	Level 2	Level 3
Graphene composition (%)	5	10	-
Extruder temperature (ºC)	220	230	240
Print speed (mm/s)	20	30	40

Layer thickness (mm)	0.1	0.2	0.3

3.3.2 Gaussian process regression (GPR)

In the proposed methodology, GPR is incorporated to model the relationships between fabrication conditions and product quality and predict the surface roughness based on the graphene composition and process parameters.

Gaussian process (GP) is a random process such that any finite subcollection of random variables has a multivariate Gaussian distribution. In GPR, it can act as a prior with mean μ and covariance K on the regression function f without a parametric form.

$$y = f(\boldsymbol{x}) + \epsilon$$

$$f \sim GP(\mu, K) \tag{3}$$

where the predictor $\boldsymbol{x} = [G, T, S, L]^T$ represents a fabrication condition with graphene composition and process parameters; the response y is the surface roughness; ϵ is the random noise. The covariance function $K(\cdot,\cdot)$ in GP is a kernel function (e.g., exponential kernel function) to measure the similarity among fabrication conditions. As a prior, GP captures beliefs that similar fabrication conditions result in similar surface roughness with its covariance function and enhance the predictive power of GPR.

In the case of modeling the surface roughness of FFF parts affected by process parameters and graphene composition, with surface roughness measurements at different FFF fabrication conditions $(\boldsymbol{x}_1, \boldsymbol{x}_2, \ldots, \boldsymbol{x}_d)$ in the training dataset, the random variables $\boldsymbol{y}_{training}$ follow a multivariate Gaussian distribution:

$$\boldsymbol{y}_{training} \sim \mathcal{N}(\boldsymbol{\mu}, \boldsymbol{\Sigma}_{training}) \tag{4}$$

where mean $\boldsymbol{\mu}$ is the expected surface roughness of FFF parts; the covariance function $\boldsymbol{\Sigma}_{training} = \boldsymbol{K}(\cdot,\cdot)$ encodes the correlations among surface roughness variables $\boldsymbol{y}_{training}$ based on the similarity among their fabrication conditions $(\boldsymbol{x}_1, \boldsymbol{x}_2, \ldots, \boldsymbol{x}_d)$. For instance, the covariance function can be represented by an exponential kernel function $\boldsymbol{K}(\boldsymbol{x}_i, \boldsymbol{x}_j) = \sigma^2 \exp(-\phi|\boldsymbol{x}_i - \boldsymbol{x}_j|)$, where σ^2 is the variance, and ϕ is the decay parameter in the covariance function. It is usually assumed that more similar fabrication conditions result in a higher correlation among surface roughness via the kernel function.

The surface roughness $\boldsymbol{y}_{testing}$ at new fabrication conditions $(\boldsymbol{z}_1, \boldsymbol{z}_2, \ldots, \boldsymbol{z}_t)$ can be predicted by GPR from the joint multivariate Gaussian distribution with the random variables $\boldsymbol{y}_{training}$ at fabrication conditions $(\boldsymbol{x}_1, \boldsymbol{x}_2, \ldots, \boldsymbol{x}_d)$ in the training data [200].

$$\begin{bmatrix} \boldsymbol{y}_{testing} \\ \boldsymbol{y}_{training} \end{bmatrix} \sim \mathcal{N}\left[\begin{pmatrix} \boldsymbol{\mu_1} \\ \boldsymbol{\mu_2} \end{pmatrix}, \quad \begin{pmatrix} \boldsymbol{\Sigma_{11}} & \boldsymbol{\Sigma_{12}} \\ \boldsymbol{\Sigma_{21}} & \boldsymbol{\Sigma_{22}} \end{pmatrix}\right] \tag{5}$$

The conditional distribution of $\boldsymbol{y}_{testing}$ at new fabrication conditions can be written in terms of $\boldsymbol{y}_{training}$ as:

$$\boldsymbol{y}_{testing} | \, \boldsymbol{y}_{training} \sim \mathcal{N}(\overline{\boldsymbol{\mu}}, \overline{\boldsymbol{\Sigma}}) \tag{6}$$

where the mean function $\overline{\boldsymbol{\mu}} = \boldsymbol{\mu_1} + \boldsymbol{\Sigma_{12}}\boldsymbol{\Sigma}_{22}^{-1}(\boldsymbol{y}_{training} - \boldsymbol{\mu_2})$ and the covariance matrix $\overline{\boldsymbol{\Sigma}} = \boldsymbol{\Sigma_{11}} - \boldsymbol{\Sigma_{12}}\boldsymbol{\Sigma}_{22}^{-1}\boldsymbol{\Sigma_{21}}$.

GPR benefits from properties inherited from Gaussian distribution in prediction and can predict with uncertainty in a closed form. The covariance function incorporates the correlations among similar process parameters and graphene composition. It can achieve a high prediction accuracy with a small dataset [115, 116, 131]. GPR is also an integral part of Bayesian optimization to discover the process parameters of FFF fabrication and graphene composition for achieving the optimal surface roughness in the FFF-fabricated ABS/graphene nanocomposite.

3.3.3 Model-agnostic interpretation methods

Model-agnostic interpretation methods [201] will be used to enhance the interpretability of GPR to investigate the effects of process parameters and graphene composition on the surface roughness of FFF parts. It can be helpful to decipher the material-process-property relationships in FFF ABS/graphene nanocomposite in a data-driven manner.

Permutation feature importance (PFI) identifies significant features and measures the importance of a feature by permuting the values of each factor and calculating the increase in the model error after permuting the feature [202]. A feature is "important" if shuffling its values increases the model error because the model relied on the feature. Mean absolute error (MAE) is selected as our error function.

Accumulated local effects (ALE) describe the average impact of a factor on the prediction based on the conditional distribution, addressing the challenges of collinearity among factors. It is a faster and unbiased alternative to PDP and can describe the dependence of features on machine learning outcomes, even when the features are correlated. ALE plots average the changes in the model outcomes and accumulate them over the grid. To estimate local effects, we divide the feature into many intervals and compute the differences in the model outcomes.

$$\hat{f}'_{x_s,ALE}(x) = \sum_{k=1}^{k_{x_s}(x)} \frac{1}{n_{x_s}(k)} \sum_{i:x_s^{(i)} \in n_{x_s}(k)} f\left(z_{k,x_s}, x_c^{(i)}\right) - f\left(z_{k-1,x_s}, x_c^{(i)}\right) \tag{7}$$

where z's is a grid of intervals over which we compute the changes in the outcome of the machine learning algorithm. ALE plots are centered at zero, and the value at each point of the ALE curve is the difference to the mean outcomes. They indicate the relative effect of changing the feature on the model outcomes.

These model-agnostic interpretation methods provide flexibility in understanding the complex material-process-property relationships discovered by GPR and facilitate knowledge exploration in nanocomposite design and fabrication with FFF.

3.3.4 Bayesian optimization

To achieve the best surface roughness in successful FFF fabrications, Bayesian optimization is integrated to simultaneously optimize process parameters and graphene composition in an iterative manner. It attempts to find the global optimum in a minimum number of iterations and is well-suited for cases with expensive experiments.

The objective function of Bayesian optimization is the regression function f in equation (3) in GPR. Bayesian optimization incorporates prior belief about f in a Gaussian process $GP(\mu, K)$ and updates the prior with observations to get a posterior that better approximates f. Bayesian optimization uses an acquisition function that directs sampling to areas where an improvement over the current best observation is likely. Expected improvement (EI) is adopted as the acquisition function here. The acquisition function balances exploration and exploitation to minimize the number of experiments via the acquisition function: (1) exploitation means sampling where the GPR model predicts small surface roughness values, (2) exploration means sampling at locations where the prediction uncertainty is high. Both correspond to high acquisition function values, and the next sampling point $\boldsymbol{x}_{new}$ is determined by maximizing the acquisition function in Eq. (8).

$$\begin{gathered}\boldsymbol{x}_{new} = \underset{\boldsymbol{x}}{\operatorname{argmax}}\ \mathrm{EI}(\boldsymbol{x}) \\ \mathrm{EI}(\boldsymbol{x}) = \mathbb{E}\max(f(\boldsymbol{x}^{+}) - f(\boldsymbol{x}), 0)\end{gathered} \tag{8}$$

where $f(\boldsymbol{x}^{+})$ is the best surface roughness so far under the fabrication condition $\boldsymbol{x}^{+}$. EI can be evaluated analytically under GP:

$$\begin{aligned}\mathrm{EI}(\boldsymbol{x}) &= \mathbb{E}\max(f(\boldsymbol{x}^{+}) - f(\boldsymbol{x}), 0) \\ &= \begin{cases}(f(\boldsymbol{x}^{+}) - \mu(\boldsymbol{x}) - \xi)\Phi(Z) + \sigma(\boldsymbol{x})\phi(Z), & if\ \sigma(\boldsymbol{x}) > 0 \\ 0, & if\ \sigma(\boldsymbol{x}) = 0\end{cases}\end{aligned} \tag{9}$$

where $Z = \begin{cases}\frac{f(x^{+}) - \mu(x) - \xi}{\sigma(x)}, & if\ \sigma(\boldsymbol{x}) > 0 \\ 0, & if\ \sigma(\boldsymbol{x}) = 0\end{cases}$, $\mu(\boldsymbol{x})$ and $\sigma(\boldsymbol{x})$ are the mean and standard deviation of the GRP prediction at the condition $\boldsymbol{x}$. Φ and ϕ are the CDF and PDF of the standard Gaussian distribution. Parameter ξ determines the amount of exploration during optimization, and higher ξ values lead to more exploration. In other words, with increasing ξ values, the importance of improvements predicted by the GP posterior mean $\mu(\boldsymbol{x})$ decreases relative to the importance of potential improvements in regions of high prediction uncertainty, represented by large $\sigma(\boldsymbol{x})$ values. EI determines the next fabrication condition for the experiment. The posterior distribution over the surface roughness random variables will be updated sequentially with observations by evaluating EI until the results converge.

The nonparametric Bayesian framework provides holistic research in developing and fabricating ABS/graphene nanocomposites for material and product innovation. It addresses the issues of inferior mechanical properties of ABS, unsuccessful FFF printing, and costly materials design with trial and error simultaneously and ensures high product quality and cost efficiency while maintaining design flexibility and customization of FFF. It will fuel fast nanocomposite design and prototype with FFF for product innovations in various industries. For instance, it can design graphene composition and FFF process parameters based on the required properties (i.e., tensile strength, surface roughness) for specific applications. The proposed nonparametric Bayesian framework for materials and process optimization will be verified in a case study in the following Section 3.4, efficiently identifying optimal process parameters for different graphene compositions and entails reliable fabrication with high product quality.

3.4 Application of nonparametric Bayesian material and process optimization

The proposed nonparametric Bayesian methodology in Section 3.3 is put into practice with a real-world case study of ABS/graphene nanocomposite design and FFF manufacturing. In contrast to the preliminary experimental trials in Section 3.3, we follow the steps in the proposed framework to systematically conduct experiments, collect data, predict part quality, and optimize process conditions for successful fabrication. The results of the case study demonstrate the effectiveness of the proposed methodology.

3.4.1 FFF experiments and data collection

3.4.1.1 Experimental design and FFF printing process

A non-regular fractional factorial design with an orthogonal array of OA (18, 2^1 3^7) [203] was utilized in this experimental design. This orthogonal array could accommodate one two-level factor and up to seven three-level factors with only eighteen experiments, therefore, greatly reducing the cost and time in FFF fabrication. The graphene composition and three critical process parameters (i.e., extruder temperature, print speed, and layer thickness) were included in the design with their respective levels as listed in Table 2 for 18 experiments. The experimental design is summarized in Table 2.

Table 2 The 18-run non-regular fractional factorial design matrix.

Experimental run	Factors			
	Graphene composition (%)	Extruder temperature (ºC)	Layer thickness (mm)	Print speed (mm/s)

1	10	240	40	0.3
2	10	240	30	0.2
3	10	240	20	0.1
4	10	230	40	0.3
5	10	230	30	0.2
6	10	230	20	0.1
7	10	220	40	0.2
8	10	220	30	0.1
9	10	220	20	0.3
10	5	240	40	0.1
11	5	240	30	0.3
12	5	240	20	0.2
13	5	230	40	0.2
14	5	230	30	0.1
15	5	240	20	0.3
16	5	220	40	0.1
17	5	220	30	0.3
18	5	220	20	0.3

Based on the experimental design in Table 2, we conducted 18 experiments, with each experiment repeated twice (printing two FFF parts for each experiment). For each experiment, the three critical process parameters were set according to the design, as well as the graphene composition. Other process parameters of the FFF machine were fixed according to the manufacturer’s recommendations, for instance, 85ºC bed temperature, 1.75mm extrusion width, rectilinear fill pattern with 100% fill density, 20% infill/perimeters overlap, and 25% fan speed.

Two type-V FFF design specimens in a symmetrical dumbbell shape (as shown in Figure 4) were printed in each experiment. Two images were taken by microscope on the left and the right side of each specimen. While capturing the surface images, strict controls were in place for reliable quantification and comparison: (1) designated one student for microscopy, (2) 3D-printed a special fixture to place the specimens for microscopy, (3) kept the same light source to ensure consistent lighting and no shadows cast on the part surface. Four microscopic images were obtained for each experiment to reduce bias in quantifying the surface quality and mitigate the impact of subtle differences in lighting among experiments.

The surface quality values S_a and S_q were calculated from the intensity values of four grayscale images in an area of 640×480 pixels, as shown in Figure 3(d)-(f). S_a and S_q values for all the experiments are summarized in Table 3.

Table 3 Surface roughness values for S_a and S_q on the left (L) and the right (R) sides of FFF printed dumbbell parts for all the experimental runs repeated twice. The bolded black numbers indicate the smallest average surface roughness; the bolded red numbers indicate the largest average surface roughness; The bolded blue numbers indicate the surface roughness with the largest variations.

Run	S_a						S_q						Surface finish
	1 (L)	1 (R)	2 (L)	2 (R)	Avg.	Std.	1 (L)	1 (R)	2 (L)	2 (R)	Avg.	Std.	
1	26.13	24.89	25.79	25.50	*25.58*	*0.53*	32.72	31.32	32.61	31.68	*32.08*	*0.69*	Overfill
2	17.96	18.88	19.96	15.61	*18.10*	*1.85*	23.48	24.87	26.21	20.75	*23.83*	*2.34*	Overfill
3	15.91	12.14	17.21	10.17	*13.86*	*3.27*	22.22	16.66	25.17	14.97	*19.75*	*4.76*	Underfill
4	24.55	22.70	24.43	27.49	*24.79*	*1.99*	30.60	28.82	30.54	33.63	*30.90*	*2.00*	Overfill
5	8.46	8.55	9.39	8.66	*8.77*	*0.42*	12.50	11.58	12.36	11.58	***12.01***	*0.49*	Normal
6	9.53	14.20	9.35	12.85	*11.48*	*2.42*	12.89	21.14	12.57	17.22	*15.96*	*4.05*	Underfill
7	11.93	11.32	10.93	11.02	*11.30*	*0.45*	16.24	15.96	14.71	14.86	*15.44*	*0.77*	Normal
8	19.14	18.05	21.55	25.44	*21.05*	*3.27*	27.00	25.82	28.76	32.61	*28.55*	*2.97*	Underfill
9	13.47	13.00	9.88	14.20	*12.64*	*1.91*	17.10	17.29	13.30	19.84	*16.88*	*2.70*	Normal
10	31.09	30.96	33.42	31.73	***31.80***	*1.13*	38.19	37.39	39.84	39.17	***38.65***	*1.08*	Overfill
11	19.93	17.34	20.07	21.29	*19.66*	*1.66*	26.62	23.98	26.11	27.63	*26.09*	*1.54*	Overfill
12	18.45	20.35	11.58	11.51	*15.47*	***4.60***	25.05	27.47	16.76	16.71	*21.49*	***5.59***	Underfill
13	11.24	9.30	14.69	13.26	*12.12*	*2.36*	15.41	12.78	20.14	18.21	*16.64*	*3.22*	Overfill
14	9.72	9.04	11.90	9.03	*9.92*	*1.36*	13.03	12.60	16.47	12.08	*13.55*	*1.99*	Normal
15	14.47	15.31	13.60	13.58	*14.24*	*0.83*	22.20	22.10	20.21	19.02	*20.88*	*1.55*	Underfill
16	10.20	8.93	8.82	9.53	*9.37*	*0.64*	13.71	13.11	11.98	13.03	*12.96*	*0.72*	Normal
17	19.46	19.76	21.80	21.50	*20.63*	*1.19*	26.80	27.34	28.94	28.47	*27.89*	*0.99*	Underfill
18	7.26	7.28	9.55	8.98	***8.27***	*1.18*	10.44	11.04	14.74	13.58	*12.45*	*2.05*	Normal

3.4.1.2 Experimental results and discussion

It can be seen from Table 3 that among the 18 experiments with different combinations of graphene composition, extruder temperature, print speed, and layer thickness, disparate surface finishes were realized, such as *normal* smooth surface finish, *overfill* with a rough surface, or *underfill* with voids. We also observed in Section 3.2.3 that FFF parts fabricated from ABS/graphene nanocomposites required process parameter adjustments for improving surface finish. For each experiment, four S_a (or S_q) values were calculated from four images of two FFF specimens, and the average and the standard deviation of four S_a (or S_q) values were used to quantify the mean and variance of the surface quality values. Since the two surface quality values S_a and S_q have a strong correlation (0.99), we chose S_a as our quality indicator in the subsequent analysis. In Table 3, the average surface quality values (S_a) of *normal* smooth surface finish were 8.27~9.92 for 5wt.% graphene and 8.77~12.64 for 10wt.% graphene; values of *overfill* with a rough surface were 12.12~31.80 for 5wt.% graphene and 18.10~25.58 for 10wt.% graphene; values of *underfill* with voids 14.24~20.63 for 5wt.% graphene and 11.48~21.05 for 10wt.% graphene. Therefore, the observed surface finish can be quantified and was consistent with the calculated surface quality values.

Moreover, it is shown from Table 3 that (i) the best surface roughness among all the experiments appears in the 5th experiment (the FFF part in Figure 8(a)) with extruder temperature 230ºC, print speed 30mm/s, layer thickness 0.2mm and 10wt.% graphene in the nanocomposite, and 18th experiment (the FFF part in Figure 8(b)) with extruder temperature 220 ºC, print speed 20 mm/s, layer thickness 0.3 mm, and 5 wt.% graphene; (ii) The worst surface roughness with overfill appears in the 10th experiment (the FFF part in Figure 8(c)) with extruder temperature 240 ºC, print speed 40 mm/s, layer thickness 0.1 mm and 5 wt.% graphene; (iii) The largest variation in the surface roughness values with underfill happens in the 12th experiment (the FFF part in Figure 8(d)) with extruder temperature 240 ºC, print speed 20 mm/s, layer thickness 0.2 mm and 5 wt.% graphene.

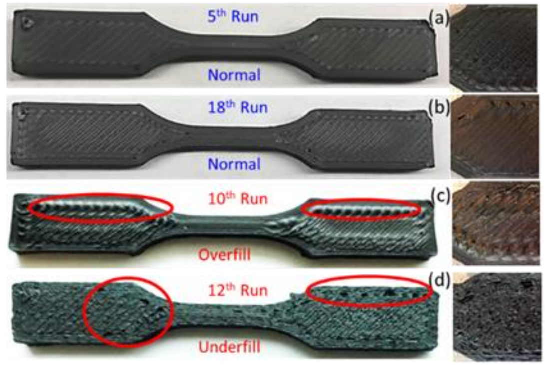

Figure 8 FFF parts printed in the experimental design show different surface quality: smooth surface finish under (a) 5th run and (b) 18th run; overfill under (c) 10th run; underfill under (d) 12th run.

In the 10th experiment, the filament was melted quickly at a high extruder temperature (240 ºC), and a high print speed (40mm/s) can lead to a high flow rate. With a too-thin layer (0.1mm), the excessive molten filaments were deposited, resulting in overfill and poor surface roughness, as shown in Figure 8(c). On the contrary, in the 12th experiment, a low print speed (20 mm/s) led to a low flow rate, with a medium layer thickness (0.2 mm), insufficient filaments were deposited, resulting in underfill and poor surface roughness, as shown in Figure 8(d).

In summary, the surface finish of FFF-fabricated ABS/graphene composite parts is affected by graphene composition, extruder temperature, print speed, and layer thickness, contributing to filament meting and depositing [21, 188, 193]. The extruder temperature mainly affects filament fusing and decomposition throughout FFF and must be correctly configured based on material thermal characteristics. Adding graphene to ABS could change the glass transition temperature of ABS and increase the melting temperature of ABS/graphene nanocomposites. The print speed affects the filament flow rate and, consequently, filament deposition. Layer thickness defines the resolution of the FFF parts. While layer thickness is the dominant parameter for the surface resolution [194], extruder temperature and print speed, affecting filament melting and flow rate, respectively, complicate the effects on the FFF surface roughness with graphene compositions.

Therefore, with the experimental data from Table 1, ANOVA was used to analyze the statistical significance of the main effects and interactions of these process parameters on the surface roughness of the FFF-printed ABS/graphene nanocomposite parts in the following section.

3.4.2 Analysis of variance (ANOVA)

ANOVA [204] was utilized to analyze experimental data and to identify factors significantly impacting the surface roughness of FFF-fabricated ABS/graphene nanocomposite. Besides the main effects from graphene composition and process parameters, we also included two-factor interactions between extruder temperature and other three factors since the heat at the extruder is the drive for filament melting and fusing in FFF and is critical to the surface roughness of FFF parts.

The ANOVA results in Table 4 manifested the significant effects of process parameters and graphene composition on the surface roughness with p-values less than the significant level (α = 0.05). The experiments also verified the significant effects of the two-factor interactions with extruder temperature and other process parameters on surface roughness by interaction plots in Figure 9. These results aligned with our experimental observations and discussion in Section 3.3 above and could be interpreted by the FFF mechanism and influencing factors. For instance, the interaction between extruder temperature and print speed was shown in Figure 9 to affect the surface quality value S_a: with 10 wt.% graphene and 0.2mm layer thickness, a medium extruder temperature (230ºC) and a medium print speed (30mm/s) in the 3rd experiment led to small S_a; so did a low extruder temperature (220ºC) and a high print speed (40mm/s) in the 7th experiment. It could be explained by the impacts on filament meting and depositing from extruder temperature and print speed. The filament was melted sufficiently at a medium extruder temperature (230ºC), and a medium print speed (30mm/s) generated an adequate flow rate for deposition without overspill; At a low extruder temperature (220ºC), the filament had a slow melting before depositing, but a high print speed (40mm/s) forced a high flow rate and counteracted the slow melting to achieve a good surface quality.

Table 4 ANOVA result showing the significance of main effects and extruder temperature-related two-factor interactions on the surface roughness (significance level $\alpha = 0.05$).

Source	DF	SS	MS	F-value	p-value
Graphene	1	20.75	20.75	4.95	0.03
Extruder T.	2	749.56	374.78	89.45	0.01
Print S.	2	378.63	189.32	45.19	0.00
Layer Th.	2	58.65	29.33	7.00	0.00
Error	54	226.24	4.19		
Total	71	3238.84			

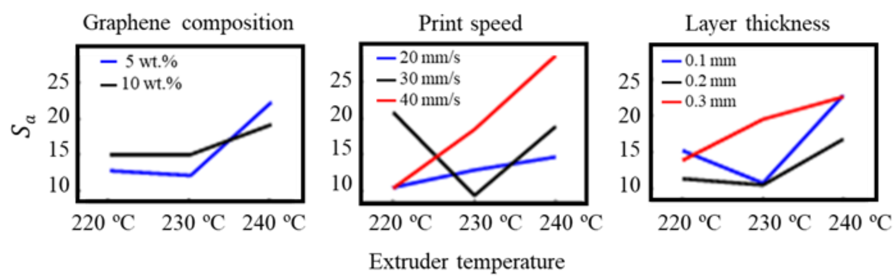

Figure 9 The Interaction plots between the extruder temperature and graphene composition/print speed/layer thickness show two-factor interactions between extruder temperature and other factors.

3.4.3 Prediction of surface roughness

Three benchmark machine learning methods, linear regression, regression tree, and support vector regression (SVR), were incorporated to compare with GPR in this study. The kernel function of the GPR model was selected as the Matern kernel function. The goodness of fit of the models was evaluated by R^2; the model accuracy was evaluated by mean absolute percentage error (MAPE) and root mean squared error (RMSE) with 5-fold cross-validation, summarized in Table 5.

Table 5 The R^2, RMSE and MAPE values of different machine learning models in predicting surface quality values S_a from graphene composition and FFF process parameters. The numbers in the parenthesis are the standard deviation of the predicted values (5-fold cross-validation).

	Linear regression	Regression tree	SVR	GPR
R^2	0.28	0.62 (0.08)	0.83	**0.84**
RMSE	5.74	4.16 (0.40)	2.79	**2.66**
MAPE	0.32	0.22 (0.01)	0.14	**0.13**

It is observed that GPR and SVR outperform the other two machine learning methods in terms of the goodness of fit and prediction accuracy. Linear regression has the lowest goodness of fit and the largest prediction error since the relationships between graphene composition/process parameters and surface roughness value S_a are unlikely to be linear; the regression tree is prone to overfitting with such a small dataset in this work. Compared to the SVR, GPR has a closed form for predicting the surface roughness value S_a and quantifying its uncertainty by leveraging its underlying assumption of S_a as Gaussian distributions and the correlation structure among different process parameters. Therefore, the GPR model is selected in this work for the surface roughness prediction of the FFF-fabricated ABS/graphene nanocomposite. The predicted surface roughness at different combinations of process parameters and graphene compositions was visualized in Figure 10, where Figure 10(a)-(c) were with 5wt.% graphene composition and Figure 10(d)-(f) were with 10wt.% graphene composition.

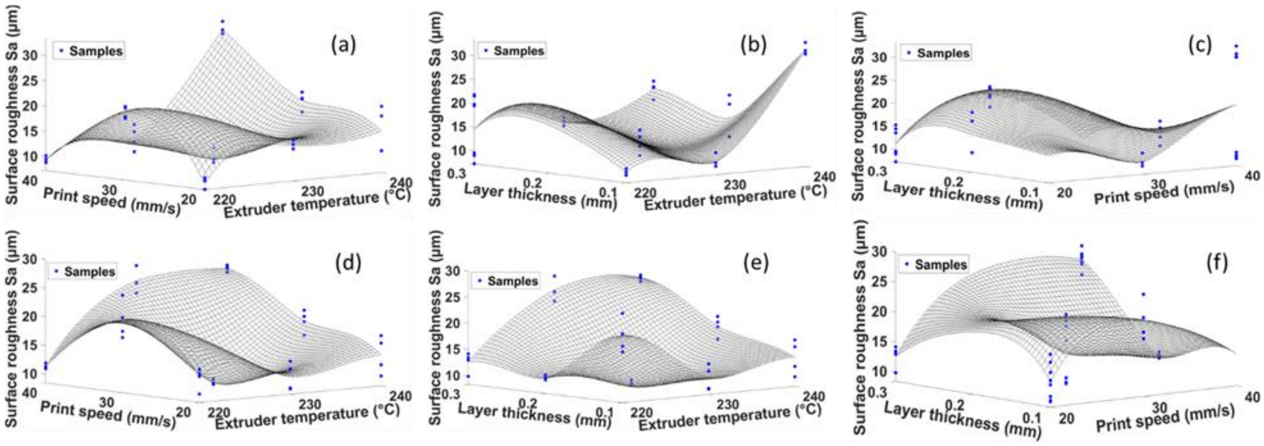

Figure 10 The predicted surface roughness S_a from GPR at different combinations of process parameters and graphene compositions: (a)-(c) are with 5wt.% graphene composition; (d)-(f) are with 10wt.% graphene composition.

Furthermore, the model-agnostic methods (PFI and ALE) were utilized to strengthen the interpretations of outcomes for the GPR model in this study. Specifically, PFI was firstly used to assess the marginal importance of process parameters concerning the predicted surface roughness S_a from GPR. Then ALE was adopted to evaluate how these critical process parameters influenced the prediction of the GPR model on average. These methods could improve comprehension of the relationships between FFF process parameters and surface roughness S_a of FFF-printed ABS/graphene nanocomposites.

PFI mainly measures the increase in the prediction error of the GPR model after permuting the process parameters. As shown in Table 6, extruder temperature and print speed were more important (with larger PFI values) to the prediction errors in surface roughness. Also, it is noted that graphene composition and layer thickness were less significant to surface roughness prediction with smaller PFI values.

Table 6 PFI with standard deviation in predicting surface roughness S_a from graphene composition and FFF process parameters.

Feature	PFI values
Extruder temperature	1.40 ± 0.606
Print speed	1.24 ± 0.094
Graphene composition	0.27 ± 0.119
Layer thickness	-0.00 ± 0.000

ALE is mainly used to describe the marginal relationship between a feature and the predicted values considering other features fixed. As shown in Figure 11, the surface roughness of FFF-printed ABS/graphene nanocomposite parts generally increased because of overflow with the increase of the extruder temperature (225~235°C) or the increase of print speed (25~35mm/s) when other parameters remained fixed. Also, the increase in layer thickness (0.15~0.25mm) had nearly no effect on the surface roughness when other parameters remained fixed, as in Figure 11 (c). All these results from ALE aligned with the PFI result in Table 6.

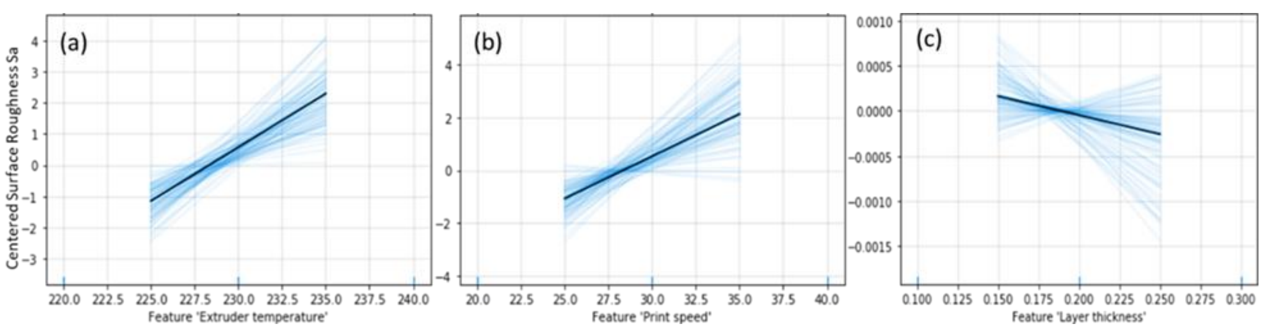

Figure 11 ALE plots to show the marginal relationships between the centered surface roughness value and (a) extruder temperature, (b) print speed, and (c) layer thickness.

Furthermore, to verify the sensitivity of surface quality values concerning the number of surface areas, we chose different numbers of observational units (i.e., the areas on which the surface quality values were obtained) for surface quality value calculation. For instance, as shown in Figure 12, on one side of an FFF part, we chose the number of observational units as 1, 4, 9, 16, 25, and 36, and the total number of roughness values for each experiment changed accordingly as listed in Table 7. Since the increase of observational units can reduce observational errors, the prediction accuracy of GPR could be increased with the increase of observational units. However, the improvement was insignificant, as indicated by the similar MAPE and RMSE of GPR models in Table 7, with surface quality values calculated from different numbers of observational units. It proved that the increment of observational units could not reduce the dominant experimental errors. A better way to improve the prediction accuracy of GPR is to increase the experimental units by printing more specimens under each printing condition.

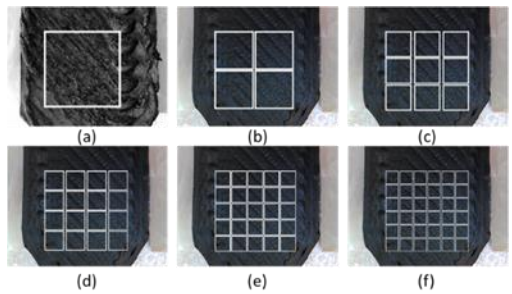

Figure 12 Different numbers of observational units (i.e., the areas on which the surface quality values are obtained) were chosen for the surface quality value calculation to verify the sensitivity of surface quality values regarding the number of surface areas.

Table 7 RMSE and MAPE values of GPR in predicting surface roughness Sa with different numbers of observational units as in Figure 10. The numbers in the parenthesis are the standard deviation of the measures (5-fold cross-validation). With the increase of observational units, no significant improvement in prediction accuracy is observed.

No. observational units	1	4	9	16	25	36
No. of data per	4	16	36	64	100	144
RMSE	2.66	2.68 (0.01)	2.86 (0.05)	**2.56 (0.03)**	2.83 (0.29)	2.73 (0.09)
MAPE	**0.13**	0.14 (0.01)	0.15 (0.01)	0.15 (0.01)	0.15 (0.01)	0.15 (0.01)

3.4.4 Process parameter optimization

We followed the proposed framework to conduct the optimization procedure iteratively for process parameters optimization. Four experiments with 5wt.% graphene were selected, as summarized in Table 8, to construct the initial GPR surrogate model. Afterward, Bayesian optimization was applied to explore the initial surrogate model within the design space of the process parameters (print speed: 20~40mm/s; layer thickness: 0.1~0.3mm; extruder temperature: 220~240ºC) to search for the optimal process parameters resulting in the lowest S_a values. The EI acquisition was maximized during each iteration to find the next fabrication condition to evaluate, which potentially led to a lower S_a value. In each iteration, a new set of process parameters was proposed after 100 times of evaluation. Two new parts were fabricated with the proposed process parameters and the observed surface quality values S_a were calculated from the microscopic images of these parts to update the surrogate model for the next iteration of the Bayesian optimization. This process ceased until the optimization results converged.

Table 8 The fabrication conditions and corresponding observed S_a values of four selected experiments to construct the initial GPR surrogate model for Bayesian optimization (5wt.% graphene).

Experiments	Factors			Response
	Extruder temperature	Print speed (mm/s)	Layer thickness	S_a
2	30	0.3	240	17.34~21.29
4	40	0.2	230	9.30~14.69
6	20	0.3	240	13.58~15.31
8	30	0.3	220	19.46~21.80

The results of Bayesian optimization are summarized in Table 9 in terms of predicted optimal process parameters and predicted surface quality values at each iteration, as well as the observed surface quality values from the fabricated parts under the predicted process parameters. Figure 13 and Figure 14 show the predicted surface quality values and their prediction uncertainties by the surrogate models (i.e., GPR models) based on the initial four experiments (see Table 8) and after each iteration of the Bayesian optimization. With a high value of parameter ξ to encourage exploration, the Bayesian optimization searched the process parameters that lead to low predicted surface quality values with high uncertainties of the prediction for next FFF fabrications. It is observed from Figure 13(a) that the Bayesian optimization accurately found the optimal process parameters leading to the lowest predicted S_a value based on the GPR model built with the initial four experiments. At the first and second iterations (see Figure 13(b) and Figure 13(c)), using the high value of parameter ξ, the Bayesian optimization found the process parameters leading to relatively low predicted S_a values with the highest prediction uncertainties (see Figure 14(b) and Figure 14(c)). At the third iteration (see Figure 13(d)), Bayesian optimization found the potential optimal process parameters (i.e., extruder temperature of 220.5 ºC, print speed of 20.01mm/s, and layer thickness of 0.29mm) resulting in low predicted S_a value with low prediction uncertainty (see Figure 14(d)). From the third to fifth iteration (see Figure 14(d)~(f)), the optimal process parameters found by the Bayesian optimization hardly changed from the ones of the third iteration with reduced prediction uncertainties. Under this circumstance, we considered the results converged and ended the optimization process. As summarized in Table 9, the optimal process parameters were found at the fourth iteration of the Bayesian optimization: extruder temperature of 220.09ºC, print speed of 20.09mm/s, and layer thickness of 0.27mm, which led to the lowest S_a values of 6.45 for 5wt.% graphene nanocomposite. The surface finishes of FFF parts and their observed surface quality values for the five iterations of Bayesian optimization were visualized in Figure 15.

Table 9 The summary results for Bayesian optimization at each iteration. For each iteration, a predicted S_a and its corresponding predicted process parameters were obtained from Bayesian optimization. New printing was conducted according to these process parameters. The observed S_a values were calculated from four images of FFF parts and were used to update the surrogate model in Bayesian optimization for the next iteration. (5wt.% graphene).

Bayesian optimization iteration	Predicted process parameters			Surface quality values	
	Print speed (mm/s)	Layer thickness	Extruder temperature	Predicted S_a	Observed S_a
First	39.99	0.19	220.67	12.19	13.97~21.18
Second	39.97	0.22	239.30	5.05	20.47~24.36
Third	20.01	0.29	220.50	14.26	10.69~12.10
Fourth	20.09	0.27	220.09	9.37	6.45~10.10
Fifth	20.12	0.29	220.76	8.69	7.31~12.95

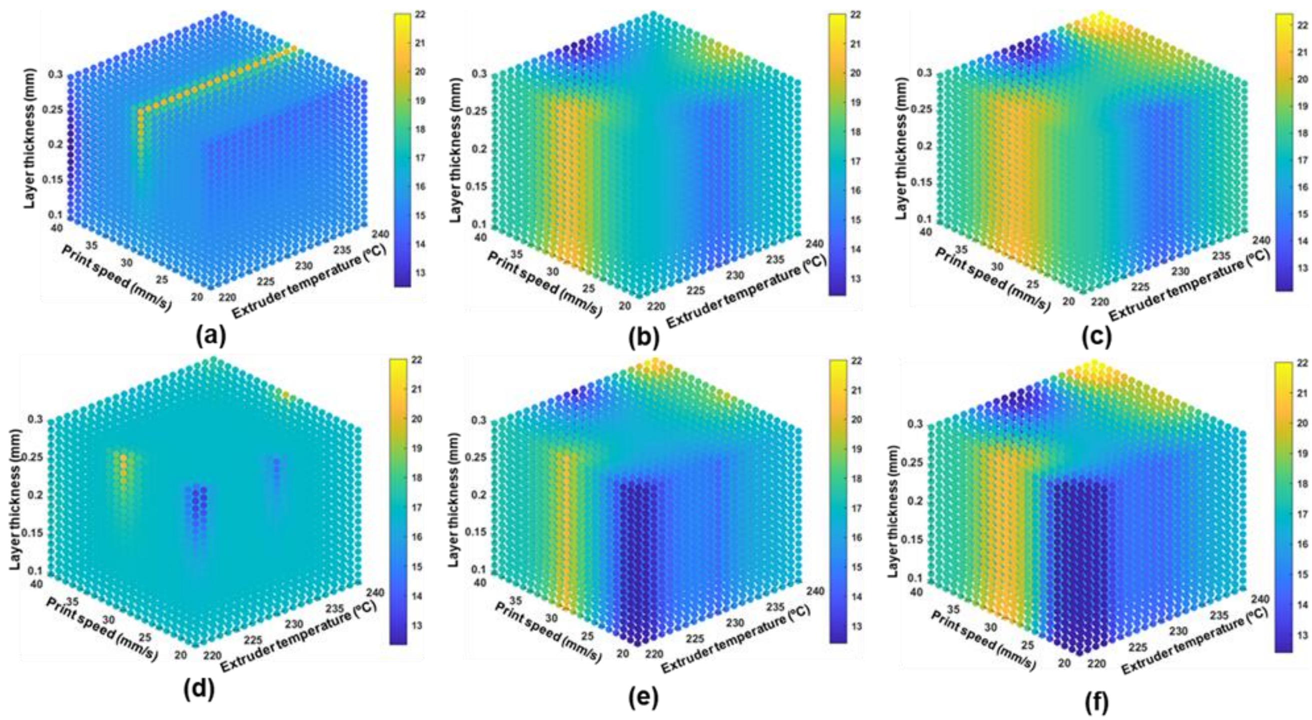

Figure 13 The predicted S_a values by the surrogate models (i.e., GPR models) within the design space of the FFF process parameters based on (a) initial four experiments and after (b) first, (c) second, (d) third, (e) fourth, (f) fifth iteration of the Bayesian optimization.

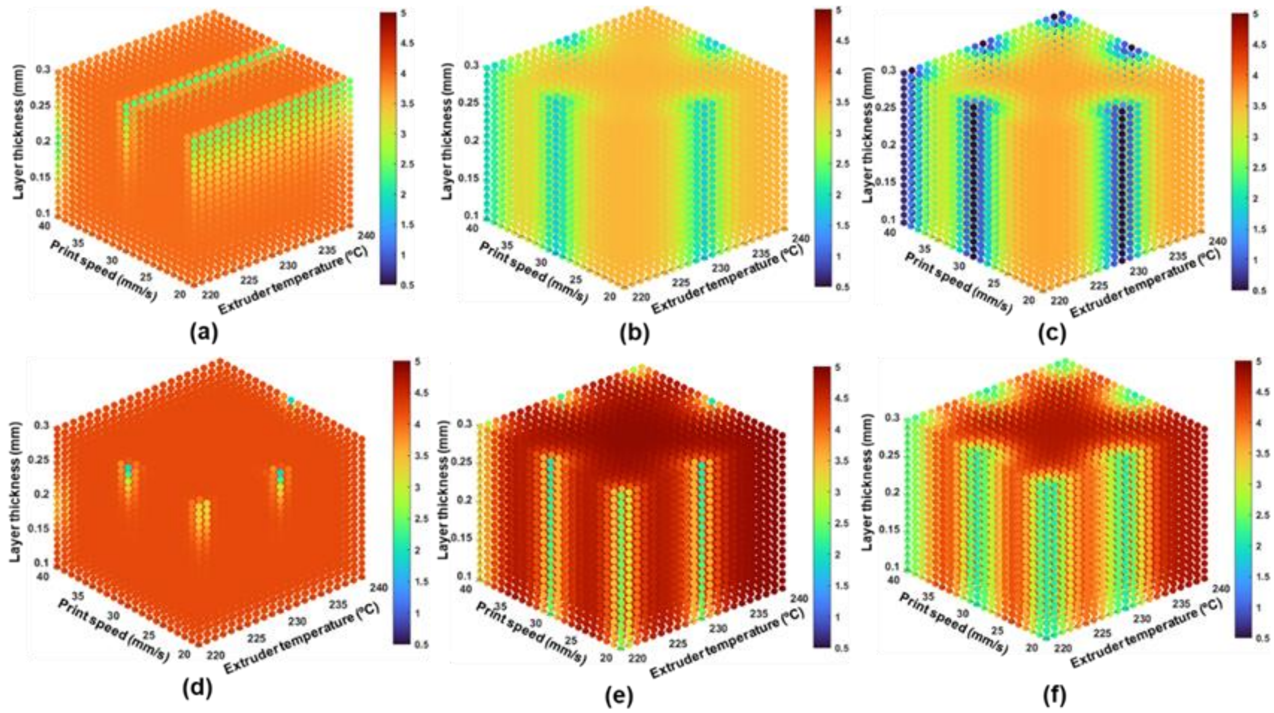

Figure 14 The prediction uncertainty (represented by the standard deviation) of the predicted S_a values by the surrogate models (i.e., GPR models) within the design space of the FFF parameters based on (a) initial four experiments, and after (b) first, (c) second, (d) third, (e) fourth, (f) fifth iteration of the Bayesian optimization.

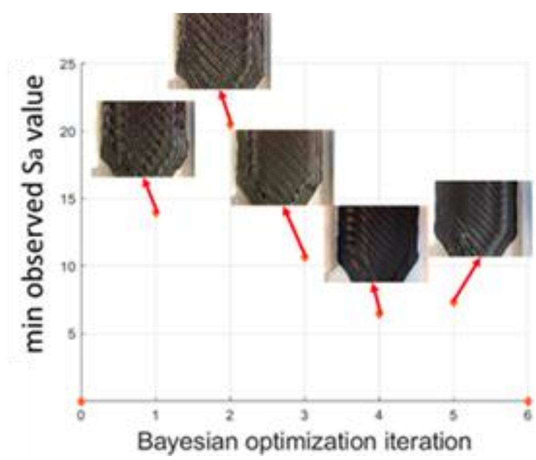

Figure 15 The surface finishes of FFF parts and their observed surface quality values for the five iterations of Bayesian optimization. The observed S_a values remained relatively stable after the third iteration.

3.5 Conclusion and future works

In this chapter, a nonparametric Bayesian framework based on Gaussian process regression (GPR) and Bayesian optimization was proposed to unify nanocomposite design and part fabrication and combine surface quality prediction and process parameter optimization to achieve superior surface roughness of the fabricated parts. The importance of graphene composition, extruder temperature, print speed, and layer thickness on the surface finish was verified and interpreted experimentally and analytically. The surface roughness prediction by using GPR outperformed the other three benchmark predictive methods in terms of the goodness of fit with the highest R^2 value ($R^2 = 0.84$) and the model accuracy with the smallest MAPE value (MAPE = 0.13) and RMSE value (RMSE=2.66). PFI and ALE were incorporated to interpret the relationships among process parameters and graphene composition with surface roughness for "black-box" GPR, revealing that extruder temperature and print speed had a more significant impact on the surface roughness. Furthermore, Bayesian optimization could find the optimal fabrication conditions for the best surface finish within a few experiments (within 5 iterations) within the design space to save time and cost for nanocomposite design.

Given its data-driven nature, this framework can be readily generalized to different materials, properties, and processes for optimizing materials design and additive manufacturing. Compared to trial-and-error or computational approaches, it can explore the design space efficiently, discover new materials, and significantly reduce design time and cost. It could be an indispensable tool for nanocomposites discovery in the data-rich era and profoundly influence their applications and fuel innovations in various industries. The authors' forthcoming research will focus on the five future aspects of this work:

(1) Conduct the Bayesian optimization with an expanded design space of FFF process parameters and more iterations to validate the optimal process parameters found in this work.

(2) Implement prediction and optimization of nanocomposite filament synthesis and FFF manufacturing in the whole production cycle using multistage modeling.

(3) Use a purpose-built surface texture measuring instrument (with appropriate filters), such as a stylus profiler or an optical profiler, to improve the measurement accuracy and modeling results.

(4) Enhance the methodology with transfer learning to extend the knowledge of material and process optimization to a distributed FFF manufacturing network with shared data.

(5) Integrate heterogeneous in-situ sensors, such as cameras and infrared sensors, to monitor the FFF printing process in real-time and formulate feedback control to improve the product quality of nanocomposites in situ.

4 Volumetric defect classification with machine learning augmented X-Ray computed tomography features for laser beam powder bed fusion

4.1 Introduction

Due to different fabrication conditions, there are three major types of defects occurring in the L-PBF process: keyholes (KHs), lack of fusions (LoFs), and gas-entrapped pores (GEPs) [39, 42, 43, 46-49]. They can initiate cracks, leading to impaired mechanical properties and reduced fatigue life of the L-PBF parts [52-55]. To identify them, high-resolution XCT (HR-XCT) scanning [97] can provide precise feature values for the defects [46, 83, 151], resulting in a high defect classification accuracy, yet it can be prohibitively costly and/or time-consuming. For instance, in the authors' previous work [205], defect features extracted from HR-XCT scans (voxel size: 1μm) led to a high defect classification accuracy (above 98%) at the cost of long scanning time (up to 12 hours for each scan). Meanwhile, the availability of HR-XCT scanning for large-sized parts is limited due to its small scanned volume [82, 206, 207]. On the other hand, LR-XCT scanning can be significantly less expensive (e.g., in our case, an LR-XCT scanning takes only 25% or less of the scanning time of an HR-XCT one), however, it typically captures much fewer features. Hence, in this research effort, we consider the question of how accurate defect classification can be performed with LR-XCT.

It is broadly agreed that KHs are large, near-spherical (more precisely, keyhole-looking) defects that occur when the excessive energy input vaporizes the powder near the bottom of the melt pool [39, 47, 98, 99]. LoFs are irregularly-shaped, elongated, and crack-like defects that occur when insufficient energy input fails to fully melt the powder between the adjacent scan tracks of the laser beam or layers [39, 47, 48, 100-102]. In this case, the occurrence of either KHs or LoFs indicates the inappropriate energy input and corresponding rectifications for the L-PBF process. For instance, KHs can be prevented by reducing the energy input [39, 42, 205, 208], while LoFs can be mitigated or prevented by increasing the energy input [39, 42, 46, 205]. GEPs are the smallest and most spherical defects among all three types [39, 42], caused by a small amount of gas – either presented originally in the powders or generated in the printing - trapped in the parts. GEPs may not be completely prevented even with appropriate energy input [42]; they can be mitigated by reducing the gas entrapment in the powder [209, 210] and optimizing the inert gas flow velocity [211].

Moreover, classifying the defects in the L-PBF parts can also assist in a better understanding of their structural integrity [56, 57, 104]. Among these three types of defects, LoFs were found to be the most detrimental to the L-PBF parts when the sharp edges of those irregularly-shaped and large-sized LoFs can induce high stress concentrations in tensile tests or under cyclical loadings [55, 100, 103]. Due to this reason, the L-PBF fabricated Ti-6Al-4V (Ti64) parts with large-sized and non-spherical LoFs exhibited lower ductility (3%-10%) than those with other types of defects (10%-15%) [212]. The stainless steel 316 L parts with irregularly shaped LoFs had an average of 20% lower fatigue limit and 12% lower fatigue life than the ones with spherical and small GEPs [213, 214]. On the contrary, GEPs were found to be the least detrimental ones due to their small sizes and spherical shapes [103]. It is reported that GEPs were harmless to the tensile, fatigue, and hardness of the L-PBF fabricated Ti64 parts when presented in amounts up to one volume percentage [102].

A practical approach for defect classification is to utilize the sizes and morphologies of different types of defects obtained by XCT scanning. Some 3D features, such as dimensions, volume, and surface area of the defects, can be directly measured from the XCT scans to quantify the defects' sizes. Furthermore, these 3D features can be used to derive other features that describe the defects' morphologies. The morphological features (as a combination of some directly measured and derived features) extracted from the XCT scans can effectively assist in distinguishing different defect types.

In this chapter, we propose a data-driven framework to augment LR-XCT with machine learning (ML) to classify the defects in the L-PBF parts with high efficiency and accuracy based on the morphological features of defects extracted from XCT scans. Our proposed framework incorporates (1) morphological features extraction from XCT scans using computer-vision-based feature derivation, (2) morphological features augmentation by regression-based features augmentation models to enhance LR scans, and (3) defect classification through ML-based classifiers. We pose that with appropriately trained augmentation modeling, it may be possible to use the LR-XCT scanning, specifically for larger and more influential defects, to replace the time-consuming HR-XCT scanning without significantly reducing classification accuracy (assuming some HR-XCT scans are also available during training).

The rest of this chapter is organized as follows. The proposed framework for defect classification is presented in Section 4.2, followed by a case study using defects in fabricated L-PBF parts to validate the proposed framework in Section 4.3. Finally, Section 4.4 provides conclusions and a discussion of future work and study limitations.

4.2 Proposed methodology

The overall structure of the proposed framework is depicted in Figure 16. It consists of three key elements: morphological feature extraction from XCT scans, morphological feature augmentation, and ML-driven defect classification, and consists of the following four steps.

Step 1 (Section 4.2.1): Morphological features describing the morphologies and sizes of the defects are extracted and derived from the HR and LR-XCT scans of the same L-PBF parts.

Step 2 (Section 4.2.2): An algorithmic defect matching model is developed to correlate the HR-XCT and LR-XCT morphological features of the same defects in HR and LR-XCT scans, enabling feature augmentation in Step 3.

Step 3 (Section 4.2.2): Regression-based feature augmentation models are built to improve the LR-XCT morphological features base on corresponding HR-XCT morphological features.

Step 4 (Section 4.2.3): ML models are employed to classify the defects into their types (i.e., KH, LoF, and GEP) using the augmented LR-XCT morphological features obtained in Step 3.

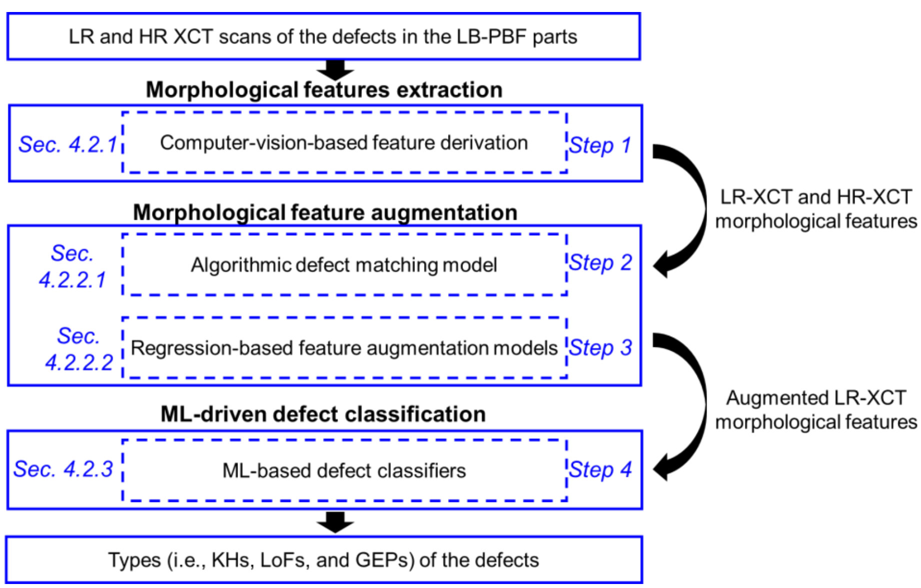

Figure 16 The overall structure of the proposed framework consists of morphological feature extraction, morphological feature augmentation, and ML models to classify the types (i.e., KH, LoF, and GEP) of the defects in the L-PBF parts from XCT scans.

4.2.1 Morphological features extraction

Figure 17 depicts typical KHs, LoFs, and GEPs observed in our experiments (see design details in Section 4.3). As discussed in the literature review, the three defect types exhibit distinct morphologies and sizes. KHs and GEPs are relatively spherical and regular, while KHs have larger sizes than GEPs; LoFs are elongated and irregular-shaped.

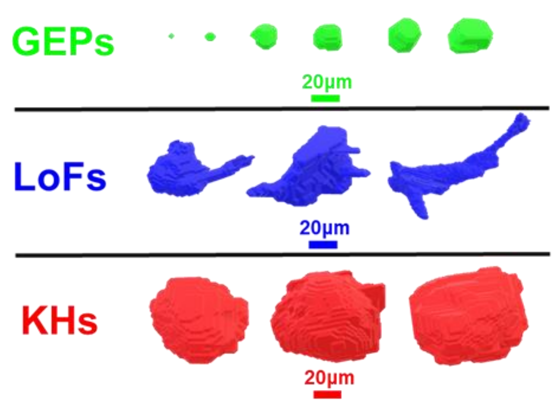

Figure 17 Several typical GEPs, LoFs, and KHs show distinct morphology and size of each type of defect.

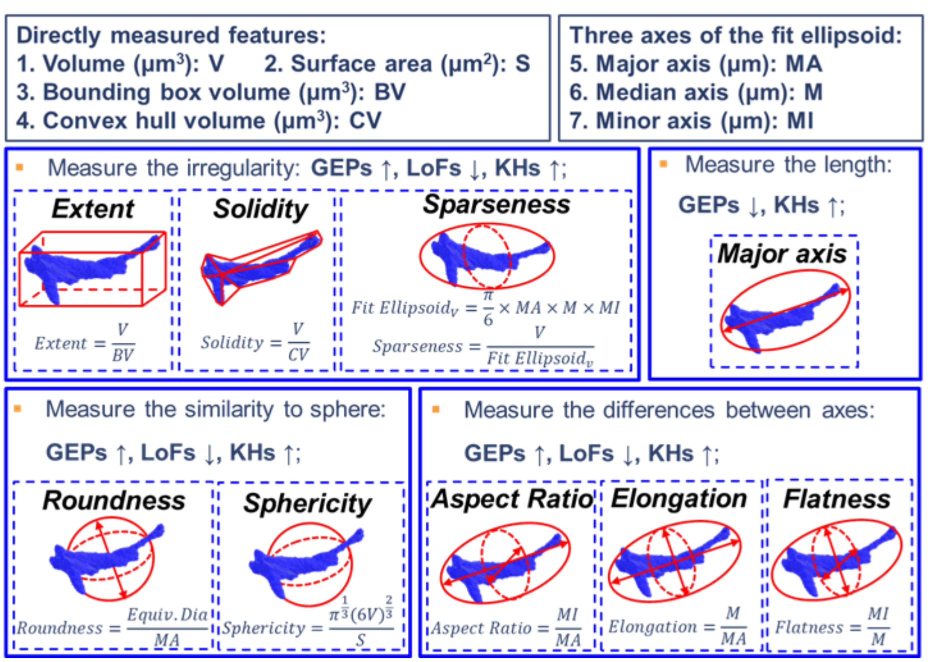

Figure 18 Illustrations of the eight morphological features derived from the directly measured features (i.e., volume, surface area, convex hull volume, bounding box volume, major, median, and minor axis of the fit ellipsoid).

To distinguish different types of defects, we employed nine morphological features: solidity, sparseness, extent, sphericity, roundness, aspect ratio, elongation, flatness, and major axis. Definitions of the features are given in Figure 18. Here, the convex hull refers to the smallest convex polyhedron that contains the defect, the fit ellipsoid is the ellipsoid with the same normalized second central moments as the defect, and the bounding box is the smallest right rectangular prism that fully contains the defect. Solidity, sparseness, and extent measure the irregularity of the defect by comparing the volumes of the convex hull, bounding box, and fit ellipsoid to the volume of the defect, respectively. The aspect ratio, elongation, and flatness measure the differences between two out of three axes of the fit ellipsoid around a defect [39, 79, 151, 160, 215]. The roundness and sphericity measure how closely a defect resembles a perfect sphere [39, 79, 216]: the former uses the ratio of equivalent diameter to the major axis of the defect, while the latter uses the ratio of volume to the surface area. Lastly, the major axis, quantifying the length of a defect, is also included in the morphological features to distinguish the sizes of different defects.

Based on characteristics and observations in the literature [39, 46-48], we surmise that these morphological features can effectively distinguish different types of defects in the L-PBF. First, the irregularly shaped LoFs are expected to have lower solidity, sparseness, and extent values than KHs and GEPs. Second, the elongated LoFs have more significant differences among their three axes and thus are expected to have a lower aspect ratio, elongation, and flatness values. Similarly, KHs and GEPs are expected to have higher roundness and sphericity. Lastly, GEPs and

KHs can be distinguished by their major axis lengths due to their differences in size. A total of nine selected morphological features are extracted from both the HR- and LR-XCT scans.

4.2.2 Morphological features augmentation

In this section, we describe the proposed approach to augmenting the LR-XCT morphological features to achieve a higher accuracy of defect classification by using the discovered relationship between the HR-XCT and LR-XCT morphological features. We first develop an algorithmic defect matching model to pair the defects in LR-XCT and HR-XCT scans and then use the regression-based feature augmentation models to find the relationship between them.

4.2.2.1 Algorithmic defect matching model

To find the relationship between defect features on LR-XCT and HR-XCT scans, it is necessary to develop an automatic way to match the defects from the respective scans. Figure 19 (a) and (b) provide a snapshot of HR and LR scans of the same scanned area, with three defects manually matched by an expect based on their position. Note that due to the limited accuracy of LR scans, mismatch in the scanned volumes, and the presence of noise, this is a non-trivial task.

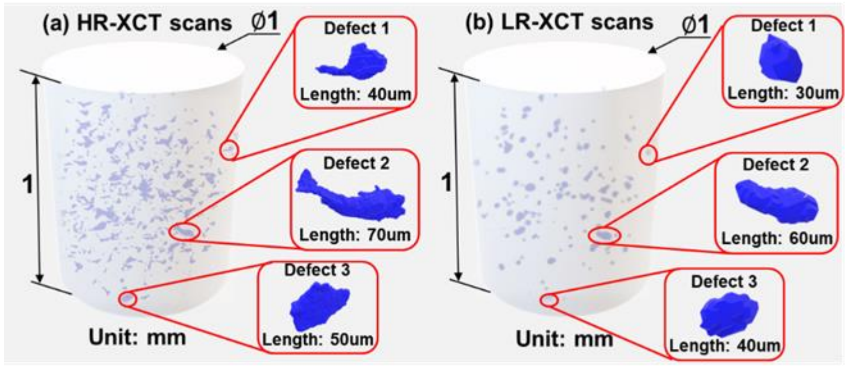

Figure 19 Defects in (a) HR- and (b) LR-XCT scans of the same scanned area with a size of 3.14mm^3. It is observed that morphologies, sizes, and numbers of the defects are changed largely with the reduced resolutions of XCT scanning. For instance, defects 1, 2, and 3 show different morphologies and sizes in HR- and LR-XCT scans.

The proposed matching algorithm is based on the following assumptions: (1) the positions of the same defects, as measured by the coordinates of the defect centroids, are similar in the HR and LR-XCT scans, and (2) the volumes of the same defects in the HR and LR-XCT scans are similar. Note that both assumptions are not necessarily true since the LR-XCT scanning, in particular, can distort the shape of the defect (and hence the position of the centroid and volume), as seen in Figure 19.

The following process is then used for matching. For each large defect (major axis length≥20µm) in the LR-XCT scans used as the target defects (TD), all the large defects in the HR-XCT scans are considered to be the candidates for matching. The match is then selected as the HR defect that minimizes the following expression, which gives the weighted sum of distance and volume ratio between TD and a candidate:

$$Min \ \left[\lambda\left(\frac{d-d_{min}}{d_{max}-d_{min}}\right)+(1-\lambda)\left(\frac{vr-vr_{min}}{vr_{max}-vr_{min}}\right)\right] \tag{10}$$

where d is the distance between the evaluated candidate and the TD, d_{min} and d_{max} are the closest and farthest distance between all the defects to be matched in HR- and LR-XCT scans; vr is the LR/HR defect volume ratio, vr_{min} and vr_{max} are the smallest and largest volume ratio between all the defects to be matched in HR- and LR-XCT scans; λ is the weighting parameter that can be selected to prioritize either the size similarity or position proximity.

4.2.2.2 Regression-based feature augmentation models

The feature augmentation models using both linear and nonlinear regression algorithms are trained to find relationships between the LR-XCT and HR-XCT morphological features. We denote the values of nine LR-XCT morphological features of a defect by X_i, $i = 1,2, \dots, 9$. Correspondingly, the HR-XCT morphological feature values of the defect are denoted by Y_j, $j = 1,2, \dots, 9$. The relationships found by the feature augmentation models are then used to augment the LR-XCT morphological features of a new defect with LR-XCT morphological feature values X_i', $i = 1,2,3, \dots, 9$, by the predicted values $\hat{Y}_j$, $j = 1,2,3, \dots, 9$.

A linear relationship between the values of HR-XCT morphological feature j and nine LR-XCT morphological features can be built by the linear regression-based feature augmentation model (multiple linear regression (MLR))[217, 218] as follows:

$$Y_j = \beta_j^0 + \beta_j^1 X_1 + \beta_j^2 X_2 + \cdots + \beta_j^9 X_9 + \epsilon_j, \quad j = 1,2, \dots, 9 \tag{11}$$

where $\beta_j^0, \beta_j^1, \beta_j^2, \dots, \beta_j^9$ are the model coefficients estimated as $\hat{\beta}_j^0, \hat{\beta}_j^1, \hat{\beta}_j^2, \dots, \hat{\beta}_j^9$, and ϵ_j are the error terms with $\epsilon_j \sim^{iid} N(0, \sigma^2)$, for $j = 1,2, \dots, 9$. The augmented LR-XCT morphological feature values of the new defect can be obtained as the predicted values $\hat{\boldsymbol{Y}}_j$ by the linear relationship:

$$\hat{Y}_j = \hat{\beta}_j^0 + \hat{\beta}_j^1 X_1' + \hat{\beta}_j^2 X_2' + \cdots + \hat{\beta}_j^9 X_9' \quad j = 1,2, \dots, 9 \tag{12}$$

Similarly, the nonlinear relationship can be found by the nonlinear regression-based feature augmentation model as follows:

$$Y_j = F_j(X_1, X_2, \dots, X_9) + \epsilon_j, \;\; j = 1,2, \dots, 9 \tag{13}$$

The function $F_j(\cdot)$ depicts the nonlinear relationship between the HR-XCT and LR-XCT morphological features and is used to augment the LR-XCT morphological features of the new defect by the predicted values $\hat{Y}_j$ as follows:

$$\hat{Y}_j = F_j(X_1', X_2', \dots X_9'), \;\; j = 1,2, \dots, 9 \tag{14}$$

The nonlinear regression algorithms used in this study include the random forest (RF) regression [143, 144, 219] and Gaussian process regression (GPR) [131, 134, 220-222].

The Mean Absolute Percentage Error (MAPE) is used to evaluate the average percent deviation of the augmented LR-XCT morphological feature values (i.e., the predicted values) from the feature augmentation models to the actual HR-XCT morphological features. The augmented LR-XCT morphological feature values with a lower MAPE value are used as predictors for the defect classification in Section 4.2.3.

4.2.3 ML-driven defect classification

In this section, we propose an ML-driven framework to use augmented LR-XCT morphological features for efficient defect classification. ML-based defect classifiers with different classification algorithms are utilized to classify the defects into different types (i.e., KH, LoF, and GEP) based on the augmented LR-XCT morphological features. The defects with similar augmented LR-XCT morphological features are more likely to be classified into the same defect types. This observation is in line with our prior knowledge of the defects in the L-PBF parts: the same type of defects has similar morphology and size.

To conduct defect classification, we use the augmented LR-XCT morphological feature value $\hat{Y}_j$, $j = 1,2,3, \dots, 9$, and type (denoted as c) of a defect as the predictors and response, respectively. A function $G(\cdot)$ is used to classify the defect into its type based on the predictors as follows:

$$c = G(\hat{Y}_1, \hat{Y}_2, \dots, \hat{Y}_9) \tag{15}$$

The ML-based classifiers $G(\cdot)$ used in this study include decision tree [223, 224], random forest (RF) [143, 144, 219], naïve Bayes [139], k-nearest neighbor (k-NN) [219], and linear Support Vector Machine (SVM) [225, 226]. They will be evaluated by classification accuracy.

4.3 Case study

4.3.1 Experiment setup

The L-PBF parts are fabricated by an EOS M290 machine with plasma atomized Ti64 Grade 5 powder (particle size range of 15 to 53µm) supplied by AP&C - a GE Additive company. The recommended process parameters for Ti64 on this machine are 280W laser power, 1300mm/s scanning velocity, 40µm layer thickness, 120µm hatch distance, 67° layer rotation, and 10mm stripe width. To induce the defects (especially KHs and LoFs), we fabricate two parts labeled “K” and “L” with excessive and insufficient energy density by adjusting the laser power and scanning velocity, as summarized in Table 10. The geometry of the fabricated L-PBF parts is shown in Figure 20, with the upper cylindrical portion scanned with XCT, as depicted.

Table 10 The process parameters used to fabricate the L-PBF parts K and L and their deviation (in parenthesis) from the recommended process parameters (i.e., laser power: 280W, scanning velocity: 1300mm/s, and energy density: 44.87J/mm^3).

L-PBF parts	Process parameters		
	Laser power (W)	Scanning velocity (mm/s)	Energy density (J/mm^3)
Part K	336 (+20%)	780 (-40%)	89.74 (+100%)
Part L	252 (-10%)	1560 (+20%)	33.65 (-25%)

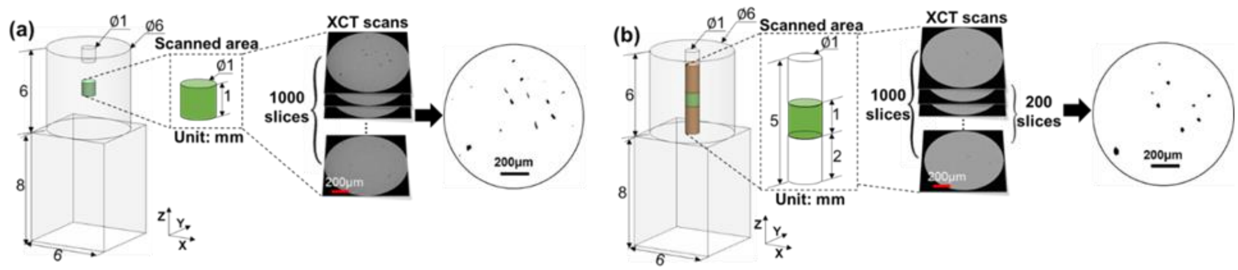

Figure 20 The geometry of the L-PBF part and the scanned areas of (a) the HR-XCT scans and (b) the LR-XCT scans. The scanned area of the LR-XCT scanning is larger than the HR-XCT scanning due to the larger voxel size of the LR-XCT scan. In this case, 200 slices in the middle are selected from the total 1000 slices of the LR-XCT scan for a similar scanned area of the HR- and LR-XCT scans in terms of size and position. The defects (black spots) are isolated from the HR- and LR-XCT scans through binarization.

The HR-XCT scanning is performed by a ZEISS Xradia 620 Versa machine with an X-ray source of 160KV and 25W power passing through a ZEISS "HE1" filter, while the LR-XCT scanning is performed by the same machine with an X-ray source of 100kV voltage and 14W power through a ZEISS "LE1" filter. [48]. For both HR- and LR-XCT scans, 1601 2D projections are collected over a full 360 degrees rotation of the scanned area in each scan. The isotropic voxel sizes of the HR- and LR-XCT scans are 1μm and 5μm, respectively. It takes approximately 12 hours to complete each HR scan and only 3 hours for each LR-XCT scan, even though the LR scans cover a volume 125 times larger than the HR scans. Only a portion of the LR scanned area, matching the HR scanned area, is selected.

The defects are isolated [227] from the XCT scans, and their morphological features are extracted. The volumetric tomography data of the XCT scans are reconstructed by the ZEISS

Reconstruction software. As shown in Figure 20, the defects (black spots) are isolated from these reconstructed images of the HR and LR-XCT scans through a binary function in ImageJ [228]. As summarized in Table 11, the numbers of the isolated defects significantly decrease with the reduced resolution of the XCT scanning, where only 87 and 164 defects are detected in the LR-XCT scans of parts K and L, respectively, compared to 129 and 911 in the HR-XCT scans.

Table 11 The total numbers of defects in the HR- and LR-XCT scans of the L-PBF parts K and L. The defects with a large major axis length (≥20μm) in the LR-XCT scans are used as the target defects (TD) for defect matching.

L-PBF parts	Defect numbers		
	HR-XCT scan	LR-XCT scan	LR-XCT scan (≥20μm)
Part K	129	87	64
Part L	911	164	79

4.3.2 Evaluation of the proposed framework

4.3.2.1 Evaluation of algorithmic defect matching model

The matching algorithm described above is applied to the defects in both Parts K and L. Note that only LR defects with major axis lengths larger than 20μm are selected for matching, i.e., the total of 64 and 79 defects are tested. A manual inspection, which verifies each pair of matched defects, is performed by AM experts to evaluate the accuracy of the algorithm. Figure 21 illustrates an example of the manual inspection to verify a pair of matched defects in part K. The TD occurs from the 12th to 20th slice of the LR-XCT scans, and its match identified by the algorithm is observed from the 53rd to 78th slice of the HR-XCT scans. The slice numbers of these two defects indicate their similar positions in the Z-axis since the height of each slice in the LR-XCT scans approximately equals the height of five slices in the HR-XCT scans (1μm and 5μm voxels). Furthermore, the relative positions of reference defect 1 (RD 1), reference defect 2 (RD 2), and TD (or its match) are similar in both LR and HR-XCT scans. Therefore, it is concluded that these two defects are correctly matched.

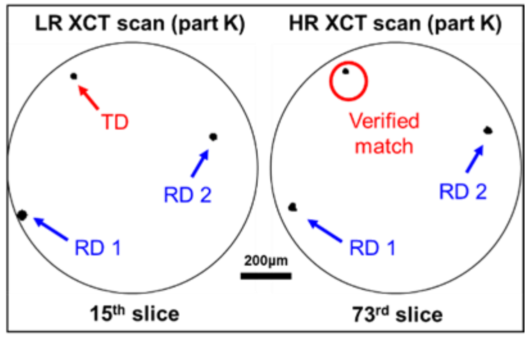

Figure 21 An example of manually verifying a pair of matched defects identified by the algorithmic defect matching model. The TD and its match have similar positions on the Z-axis, and similar relative positions of the reference defect 1(RD 1) and reference defect 2 (RD 2) to the TD (or its match) are observed.

Figure 22 depicts the accuracy of the proposed matching algorithm with different values of weighting parameter λ. The best accuracy is observed to be 98.73% and 90.65% in parts L and K, respectively, which can be simultaneously achieved for λ ranging from 0.48 to 0.5, indicating roughly equal importance of defect position and volume in defect matching. For the rest of the study, we select λ equal to 0.5.

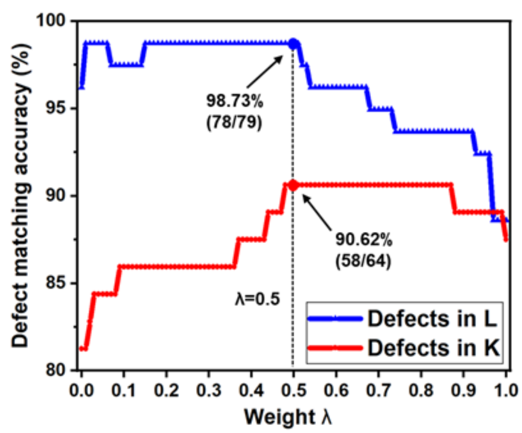

Figure 22 Accuracy of the algorithmic defect matching model to match the defects in the L-PBF parts L and K with weighting parameter λ varying from 0 to 1. The best defect matching accuracy can be simultaneously achieved as 98.73% (78 out of 79 pairs are correctly matched) and 90.65% (58 out of 64 pairs are correctly matched) for the defects in parts L and K, respectively, when λ equals 0.5.

4.3.2.2 Evaluation of feature augmentation models

A separate prediction model is constructed to augment each of the features. For each target feature to be augmented, its corresponding HR-XCT morphological feature is used as the response variable, and the LR-XCT morphological features are the predictors. For each of the nine response variables, we construct multiple linear regression (MLR), random forest (RF), and Gaussian process regression (GPR) models. Only those LR-XCT morphological features statistically significant to the responses are used as predictors in the MLR-based models to improve the prediction accuracy. In contrast, all the LR-XCT morphological features are used as predictors in the RF- and GPR-based feature prediction models. 5-fold cross-validation is employed in all cases. Mean Average Percentage Error (MAPE) is used to evaluate model accuracy.

Table 12 The average MAPE values and standard deviations (in the parenthesis) of the linear regression and nonlinear regression-based feature augmentation models using MLR, RF, and GPR algorithms on nine morphological features.

Morphological features	Mean Average Percentage Error (MAPE) values		
	Linear regression models	Non-linear regression models	
	MLR	RF	GPR
Solidity	0.212 (0.006)	**0.187 (0.003)**	0.204 (0.005)
Sparseness	0.239 (0.005)	**0.201 (0.002)**	0.225 (0.003)
Extent	0.525 (0.012)	**0.418 (0.018)**	0.466 (0.009)
Aspect ratio	0.276 (0.006)	0.263 (0.003)	**0.258 (0.002)**
Elongation	0.240 (0.004)	0.239 (0.001)	**0.233 (0.003)**
Flatness	0.147 (0.003)	0.138 (0.003)	**0.137 (0.001)**
Roundness	0.204 (0.002)	**0.178 (0.001)**	0.186 (0.003)
Sphericity	0.133 (0.004)	**0.117 (0.002)**	0.124 (0.005)
Major axis	**0.207 (0.003)**	0.215 (0.004)	0.214 (0.002)

Table 12 summarizes the results. Overall, the average MAPE values of these feature augmentation models indicate that most augmented LR-XCT morphological features have an average of approximately 20% deviation from the HR-XCT morphological features (assumed to be ground truth) except extent (47%), flatness (14%), and sphericity (12%). It is observed that nonlinear regression-based models outperform MLR in predicting all the derived morphological features except the major axis, with smaller MAPE values. Note that since the derivations of these eight morphological features are through nonlinear calculations (see Figure 18), it is reasonable to expect that a nonlinear ML model may be more suitable. On the other hand, the linear regression model slightly outperformed nonlinear models for the major axis, a directly measured feature. This model has a single predictor as the LR-XCT major axis, which is the only feature being statistically significant to the response and has a relatively stronger linear correlation, and takes the form of:

$$\hat{Y}_{marjor\ axis} = 4.032 + 1.076 X_{major\ axis} \tag{16}$$

The estimated model coefficients indicate that the major axis lengths of defects are shrunk in the LR-XCT scans. It is worth noting that all models' performance is very close in all cases.

Though the obtained average accuracy (20% MAPE) can be viewed as relatively low, since our goal is defect classification, we argue (and experimentally demonstrate in the next section) that even low accuracy prediction could still improve the classification accuracy.

4.2.2.3 Evaluation of defect classification

For the correctly matched pairs of defects, we label the types (i.e., KH, LoF, and GEP) of defects based on their morphologies and sizes in the HR-XCT scans. Five AM experts experienced in defect classification individually label these defects in the HR-XCT scans, and only the defects labeled with a consensus (at least four out of five experts) are included in this study. As a result, a dataset of 131 (out of 136 correctly matched pairs of defects) defects, including 31 KHs (23.7%), 73 LoFs (55.7%), and 27 GEPs (20.6%), along with their morphological features, are integrated for defect classification. The dataset is randomly divided into training (70%) and testing (30%), with the same proportion of each defect type as the whole dataset. Five popular ML models: decision tree, random forest (RF), naïve Bayes, *k*-nearest neighbor (*k*-NN), and linear Support

Vector Machine (SVM) classifiers, have been used for classification and compared according to their accuracy.

Model performance is summarized in Table 13, where the rows correspond to ML models, and the three columns represent the predictors used: LR-XCT morphological features, augmented LR-XCT morphological features, and HR-XCT morphological features. Naturally, predictors trained and tested on HR scans show the best performance (94%-97% depending on the models) since the HR scans provide the most accurate representation of the actual shape and size of the defects. On the other hand, if LR data only is available, the defect classification accuracy drops to only 77%-82%. Most importantly, for 4 out of 5 tested models (except the decision tree classifier), the introduction of augmented LR-XCT morphological features significantly improves the accuracy. For the best model (*k*-NN), the accuracy improves from 82.9% to 90.9%. While augmentation cannot completely overcome the limitations of the LR images (since the accuracy is still lower than what is possible with HR scans, i.e., 94% for *k*-NN), the proposed framework can vastly reduce the time of defect classification with the time-consuming HR-XCT scanning (12 hours for each scan) to the LR-XCT scanning (3 hours for each scan).

Table 13 Average defect classification accuracy and standard deviation (in the parenthesis) of the classifiers using the LR-XCT, augmented LR-XCT (ALR-XCT), and HR-XCT morphological features.

Classifiers	Predictors		
	LR-XCT	ALR-XCT	HR-XCT
Decision tree	0.804(0.030)	0.804(0.030)	0.972(0.004)
RF	**0.829(0.039)**	0.880(0.059)	**0.974(0.027)**
Naïve Bayes	0.778(0.064)	0.838(0.029)	0.966(0.014)
k-NN	**0.829(0.039)**	**0.906(0.039)**	0.940(0.029)
SVM (linear)	0.795(0.026)	0.872(0.044)	0.940(0.039)

Since the *k*-NN classifiers using LR-XCT and augmented LR-XCT morphological features have the highest average accuracies among all the classifiers using the same predictors, they will be used as the classifiers in the proposed framework. The *k*-NN classifiers measure the distances among the defects in the multi-dimensional augmented LR-XCT morphological feature space and classify them by the majority of defect types among their *k* nearest neighbors. In this study, ten nearest neighbors (i.e., defects in the training datasets) measured by Euclidean distance are used in the vote to classify the new defects (i.e., defects in the test dataset). Each neighbor is inverse distance weighted (i.e., weight=1/distance), where the defects closer to the new defects have more impact on the classification result.

To further validate the improvement in defect classification accuracy resulting from the proposed framework, we present the confusion matrices of the *k*-NN-Augmented LR (ALR) and *k*-NN-LR classifiers on the test dataset shown in Table 14. Compared to the *k*-NN-LR classifier, the *k*-NN-ALR classifier correctly distinguishes all the LoFs from the other two types of defects and identifies more KHs. These improvements indicate that the proposed framework can augment the LR-XCT morphological features to identify more detrimental LoFs, which are more likely to initiate cracks due to their irregular shape and sharp edges [47, 55, 101], and KHs, which negatively impact the fatigue life of the L-PBF parts more due to their larger sizes than GEPs [50, 129].

Table 14 Confusion matrices of classification performance of the k-NN-ALR classifier (a) and k-NN-LR classifier (b) on the test dataset consisting of 8 GEPs, 22 LoFs, and 9 KHs.

(a) Confusion matrix of *k*-NN-ALR

Actual \ Predicted: Types	GEP	LoF	KH
GEP	**7**	0	1
LoF	0	**22**	0
KH	1	2	**6**

(b) Confusion matrix of *k*-NN-LR

Actual \ Predicted: Types	GEP	LoF	KH
GEP	**6**	1	1
LoF	1	**21**	0
KH	1	3	**5**

Lastly, to examine the effect of the proposed framework on classifying the largest defects, which are most important to the structural integrity of the L-PBF parts among all the defects [103, 104], we conduct another defect classification based on the defects with their major axes larger than 50μm using the *k*-NN classifier. Note that this is a binary classification since only 17 labeled LoFs and 11 labeled KHs are longer than 50μm among all the 131 defects used in this study. The average classification accuracy summarized in Table 15 shows that the *k*-NN-LR classifier has a high accuracy of 96.3%, which indicates that even though the LR-XCT morphological features are less accurate in presenting actual morphologies and sizes of defects, these features can still be used to classify most of the largest defects accurately. Besides, no improvement in the accuracy of the *k*-NN-ALR classifier over the *k*-NN-LR one to classify the largest defects is observed, which indicates that the proposed framework is more effective in augmenting the LR-XCT morphological features of defects between 20μm to 50μm for a higher defect classification accuracy.

Table 15 Average defect classification accuracy and standard deviation (in the parenthesis) of the k-NN classifiers using the LR-XCT, ALR-XCT, and HR-XCT morphological features to classify the largest defects (major axis⩾50μm).

Classifiers	Predictors		
	LR-XCT	ALR-XCT	HR-XCT
k-NN	0.963(0.064)	0.963(0.064)	**1(0.000)**

4.4 Conclusion and future works

In this study, we propose a data-driven framework to augment LR-XCT defect inspection and classification using limited HR-XCT data. This can greatly improve the efficiency and accuracy of LR-XCT inspection and classification, promote the nondestructive inspection of L-PBF parts, and pave the way to understand the impacts of defect on fatigue performance of L-PBF parts. It centers on time-efficient LR-XCT scanning to improve its efficiency and utilizes ML to augment the morphological features extracted from the LR-XCT scans for improved accuracy of defect classification. Specifically, nine morphological features (solidity, sparseness, extent, sphericity, roundness, aspect ratio, elongation, flatness, and major axis length), which describe the morphologies and sizes of defects, are derived to distinguish different defect types and extracted from the LR- and HR-XCT scans. An algorithm for matching the same defects observed in LR-XCT and HR-XCT images is developed, which uses the defect positions and volumes to match with an accuracy exceeding 95%. The LR-XCT morphological features are augmented with regression-based features augmentation models, which build linear (using the MLR algorithm) or non-linear (using RF and GPR algorithms) relationships between the LR-XCT and HR-XCT measurements. It is then observed that for a collection of classification models, using augmentation does indeed significantly improve the classification accuracy. We conclude that the *k*-NN classifier exhibits the best performance, with 82.9% accuracy for LR features only, which can be improved to 90.6% with augmentation. Furthermore, for the largest defects that are more important for the structural integrity, specifically the fatigue performance, the *k*-NN classifier can classify them with high accuracy of 96.3% using LR features with or without augmentation.

The classification results showing the types of defects can be used as an effective method to identify and improve the quality of fabricated parts by the L-PBF process. Since large-scale HR-XCT scanning is not feasible for most practical applications due to inherent limitations (long scanning time, limited scanned area, and high cost), the proposed framework can be an efficient but sufficiently accurate way for defect classification with LR-XCT scans.

It should be noted that KH, LoF and GEP are the only three types of internal defects considered in this research. Some authors distinguish other possible types, such as unmelted powder particles or internal cracking [49, 138, 229]. For the samples manufactured in this study, such less often identified types were not present (as analyzed by the experts involved in labeling the defects). Hence, we believe that this choice does not significantly limit our conclusions. At the same time, it may pose a challenge for application of the proposed methodology to other datasets with other defect types present. Specifically, as defined, the algorithms proposed here are not restricted to the three defect types considered. Indeed, as long as the defect types can be distinguished based on morphological features, the proposed ML methods can be expected to retain some level of predictive power, and augmenting LR-XCT with HR-XCT can be expected to improve accuracy. For example, the internal cracking is reported to be irregularly shaped, and both longer and more elongated than other types of defects with a larger major axis and lower aspect ratio [230-232]. Consequently, if such cracking is present in the training dataset (and appropriately labelled), then a new 4-class (KH, LoF, GEP, and internal cracking) *k*-NN classifier, which can distinguish the internal crack from other types of defects by a combination of morphological features, can be trained according to the framework described here. However, it is difficult to establish a priori whether such a classification problem may be more difficult than the 3-class classification considered so far, and hence, whether the proposed classification method will retain the high accuracy observed so far. Given the reported distinct morphological features of cracking, we can surmise that in principle the approach may be expected to perform well, but ultimately, further experiments are need to reveal the accuracy in cases where other types of defects are of interest.

In addition to expanding the types of defects considered, a number of other promising future research directions can be proposed, including:

(1) Evaluate the proposed framework by the defect classification accuracy with a large number of defects in the newly fabricated L-PBF parts.

(2) Enhance the accuracy of the algorithmic defect matching model by filtering the target defects in the LR-XCT scans and the features augmentation models by using more features extracted from the XCT scans.

(3) Expand the proposed framework to other defect types, e.g., internal cracks, with our experimental data and publicly available datasets.

(4) Apply the proposed framework to search for the optimal fabrication conditions of L-PBF parts through the defect classification results.

Appendix

A. The discussion of incorrect defect matches by the algorithmic defect matching model

The incorrect matches computed by the algorithmic defect matching model to the TDs are investigated individually for potential improvement of the model. Since the reasons (e.g., unable to be verified, different scanned areas, scanning problems) for the mismatched pairs are not directly caused by the algorithmic defect matching model, we will temporarily stick to the current model and leave the potential improvement in the future works.

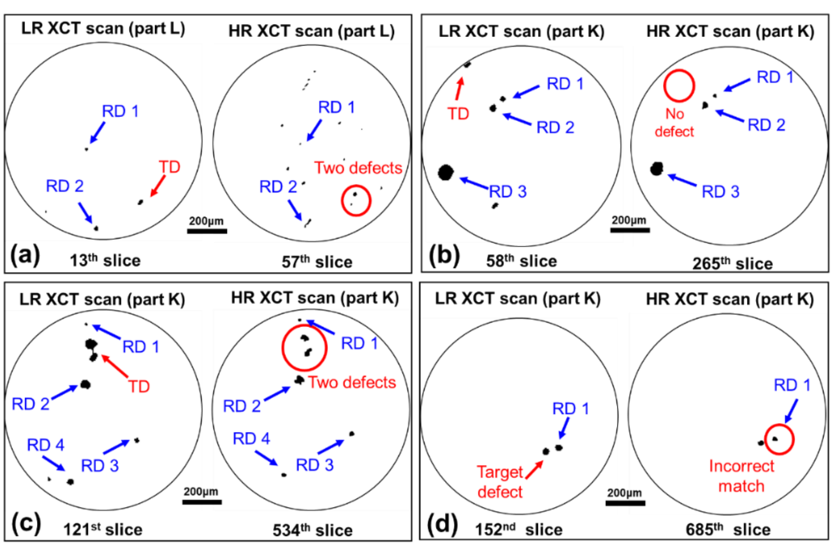

Figure 23 Illustrations of four mismatched pairs of defects computed by the algorithmic defect matching model.

Only one pair of defects is incorrectly matched for the defects in part L. As shown in Figure 23(a), two possible matches have similar positions in the Z-axis and relative positions to RD 1 and RD 2 with the TD. Hence, they cannot be verified by manual inspection and are deemed as incorrect matches.

Besides, six pairs of defects are incorrectly matched for the defects in part K due to three different reasons. First, four TDs are at the edge of the LR-XCT scan, and their HR counterparts may not be in the scanned area of the HR-XCT scan. For example, as shown in Figure 23(b), no possible match is found to have a similar position in the Z-axis and relative positions to three reference defects. Therefore, the matches to these four TDs are deemed incorrect. Second, as shown in Figure 23(c), one TD in the LR-XCT scan is a connected defect of two separate defects in the HR-XCT scan. Therefore, the match to this TD is deemed incorrect. Another mismatched pair is caused by a close distance between two defects. As shown in Figure 23(d), the RD 1 in HR-XCT is simultaneously matched to the RD 1 and TD, which are close to each other in the LR-XCT scan, leading to one mismatched pair.

5 Cross-dimensional defect matching process for Laser Beam Powder Bed Fusion fabricated parts: identifying the critical defects within the volumetric defects in the X-ray computed tomography scans

5.1 Introduction

The fatigue life of L-PBF parts under cyclic loadings is inferior to their wrought counterparts, affecting their functionality and durability [78, 233, 234]. Among the main factors (i.e., surface roughness, residual stress, process-induced volumetric defect) affecting the fatigue life of the L-PBF parts, the effects of the surface roughness or residual stress can be mitigated through machining or heat treatments, respectively. In this case, for the machined L-PBF parts with residual stress-relieving heat treatments, the process-induced volumetric defects are the most significant factor affecting the fatigue life since cracks initiated from those defects can lead to the fatigue failure of the L-PBF parts [44, 50, 61, 65-67]. More specifically, sizes, morphologies, and positions of the defects play important roles in the initiation and propagation of the cracks [44, 51, 68-70]. For instance, large and irregularly shaped defects can easily initiate cracks from their sharp edges or corners due to high-stress concentrations [44, 45]. Besides, cracks initiated from the defects being close to the surface can cause fatigue failure of the L-PBF parts with less propagation time [44].

Three-dimensional (3D) features characterizing the positions, sizes, and morphologies (e.g., spatial distribution, volume, and sphericity) of the defects can be obtained by computer vision-based feature extraction from non-destructive X-ray computed tomography (XCT) scans of the L-PBF parts [81-84, 105]. However, critical defects (i.e., the defects at the fracture origin), which are more influential to the fatigue life of the L-PBF parts than other defects, cannot be specifically identified among numerous volumetric defects in the XCT scanned areas. On the other hand, the critical defects can be observed on the scanning electron microscope (SEM)-based fractography images of the fracture surfaces of the L-PBF parts [77-79]. Some two-dimensional (2D) features (e.g., distance from the surface and area) of the critical defects can be extracted from their contours outlined on the fracture surfaces, which provide useful information for identifying the matches to the critical defects among the volumetric defects in the XCT scans.

In this chapter, we aim to propose a cross-dimensional defect matching process to specifically find the match to the critical defect among the volumetric defects in XCT scans based on defect features. The proposed procedure consists of three steps:

(1) Defect features characterizing the positions, sizes, and morphologies are extracted from the critical defect and volumetric defects.

(2) Candidate defects with similar positions as the critical defect are selected from the volumetric defects by thresholds of their positions.

(3) The selected candidate defects are ranked by the Dissimilarity Scores (DSs), which quantify their pairwise similarities to the critical defect in positions, sizes, and morphologies.

The candidate defect in 3D XCT scans with the highest similarity is identified as the match to the critical defect. Identifying the match to the critical defect not only reveals the important features of the critical defect, which contributes to the fatigue life of L-PBF parts, but also opens the possibility of critical defect identification and fatigue life prediction non-destructively.

The rest of this chapter is organized as follows: the proposed defect matching process for critical defect identification is elaborated in Section 5.2. It is then implemented in a case study of

L-PBF parts in Section 5.3 with identification results and discussions; lastly, the conclusion and future works are presented in Section 5.4.

5.2 Proposed methodology

In this chapter, we propose a cross-dimensional (3D/2D) defect matching process to identify the match to the critical defect on the fractography (2D) image among all the 3D volumetric defects in the XCT scans, which have the most similar positions, sizes and morphologies as the critical defect. Note that this work only considers single critical defect for crack initiation without the interaction between neighboring defects [50]. Figure 24 shows the three steps of the proposed procedure for each L-PBF part as follows:

Step 1 (Section 5.2.1): Defect features characterizing the positions, sizes, and morphologies are extracted from the critical defect and volumetric defects.

Step 2 (Section 5.2.2): Candidate defects with similar positions as the critical defect are selected from the volumetric defects by thresholds of their positions.

Step 3 (Section 5.2.3): The selected candidate defects are ranked by the Dissimilarity Scores (DSs), which quantify their pairwise similarities to the critical defect in positions, sizes, and morphologies.

As a result, the candidate defect with the lowest pairwise DS is identified as the match to the critical defect.

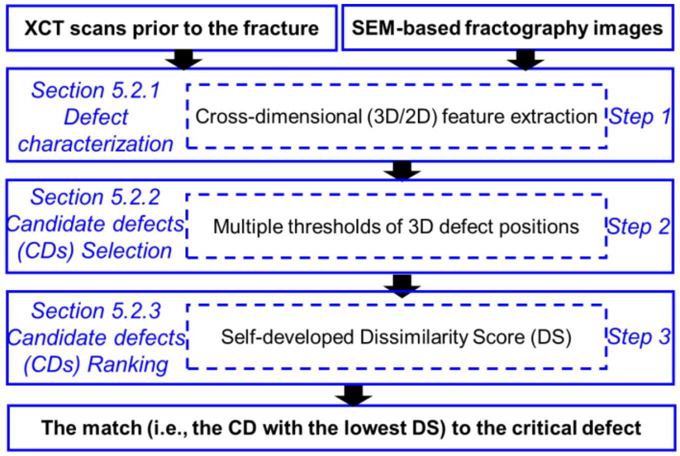

Figure 24 The overall structure of the proposed procedure consisting of the characterization of defects, selection, and ranking of the candidate defects for identifying the match to the critical defect among all the volumetric defects for each L-PBF part.

5.2.1 Defect characterization by feature extraction

5.2.1.1 Feature extraction of the critical defect

As shown in Figure 25, for the critical defect observed on the fracture surface, its position features can be mainly represented by its distance from the surface, the place of fracture surface (i.e., Z-location), and relative position information from a reference. The distance from the surface of the critical defect is measured as the distance from the centroid of its contour to the surface. The Z-location of the critical defect is estimated by the layer of the fracture surface in the L-PBF parts. In this study, a copper tape is attached to the part as a reference to indicate the position of the critical defect by their relative angular position. Those three position features are used to represent the 3D position of the critical defect for selecting the candidate defects with similar positions in the second step. Furthermore, the distance from the surface showing the 2D position of the critical defect is used in the third step for calculating the DS between the critical defect and each candidate defect.

To characterize the sizes and morphologies of the critical defect, we extract seven 2D defect features from its contour (as shown in Figure 25(b)) on the fracture surface. The first three features, i.e., area, perimeter, and Feret diameter (the longest distance between any two parallel lines tangent to the edge of an object [235]), characterize the size of the critical defect. The other four, including aspect ratio, circularity, extent, and solidity [79, 236, 237], quantify the morphologies of the critical defect. The aspect ratio measures how elongated a defect is by the ratio between the major and minor axis (of the fit ellipse) of the critical defect. Circularity measures how closely a defect resembles a circle by comparing the area to the perimeter. The extent and solidity measure the irregularities in the geometry of a defect by the ratio of its bounding box and convex hull area to the area, respectively. Those seven defects are used in the third step for calculating the DS.

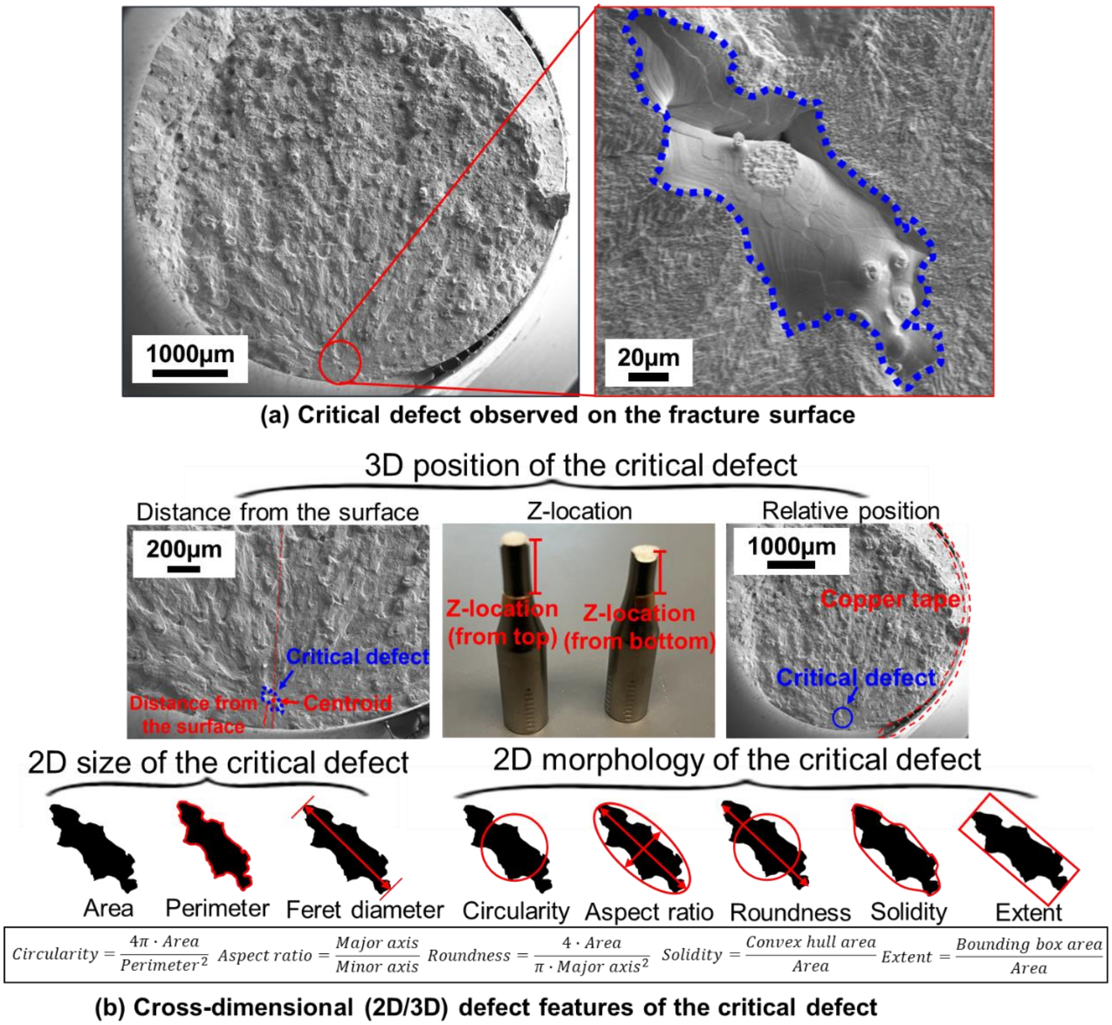

Figure 25 Illustration of (a) a critical defect identified on the fracture surface and (b) defect features that characterize the 3D position, 2D size, and morphology of the critical defect being extracted in the first step of the proposed procedure.

5.2.1.2 Feature extraction of the volumetric defects

For the volumetric defects in 3D XCT scans, their positions can be directly obtained by the X-, Y-, and Z-locations of their centroids. With the positional information, candidate defects with similar 3D positions as the critical defect can be selected from the volumetric defects in Step 2 of the proposed procedure. The distances from the surface of the candidate defects calculated by their X- and Y-locations are further used in Step 3 for calculating the DSs.

For comparable comparisons between the features of the critical defect and candidate defects, we extract the same 2D defect features from the candidate defects using two different methods. First, as illustrated in Figure 26, the 2D defect features are extracted from the projection of each candidate defect on the plane perpendicular to the stress (i.e., XY plane). Second, as illustrated in Figure 27, the 2D defect features extracted from all the slices of each candidate defect on the XY plane. Noted the candidate defect is rotated around the X-axis with a certain angle, which leads to the largest projected area of its slice, for more accurate representation of the candidate defect on the fracture surface. Those seven features extracted by the two different methods are used in Step 3 to evaluate the similarities between each candidate defect and the critical defect in DS. For feature extraction using the first method, it is expected that the projection of the match is similar to the critical defect on the fracture surface. For feature extraction using the second method, at least one slice of the match is expected to be similar to the critical defect on the fracture surface.

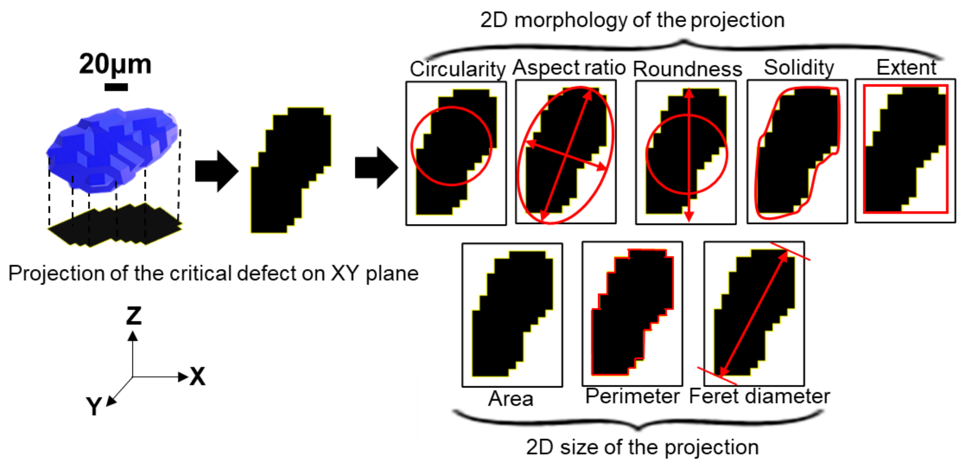

Figure 26 Illustration of the defect features, which characterize the 2D size and morphology of a candidate defect in the XCT scans, being extracted from its projection on the XY plane.

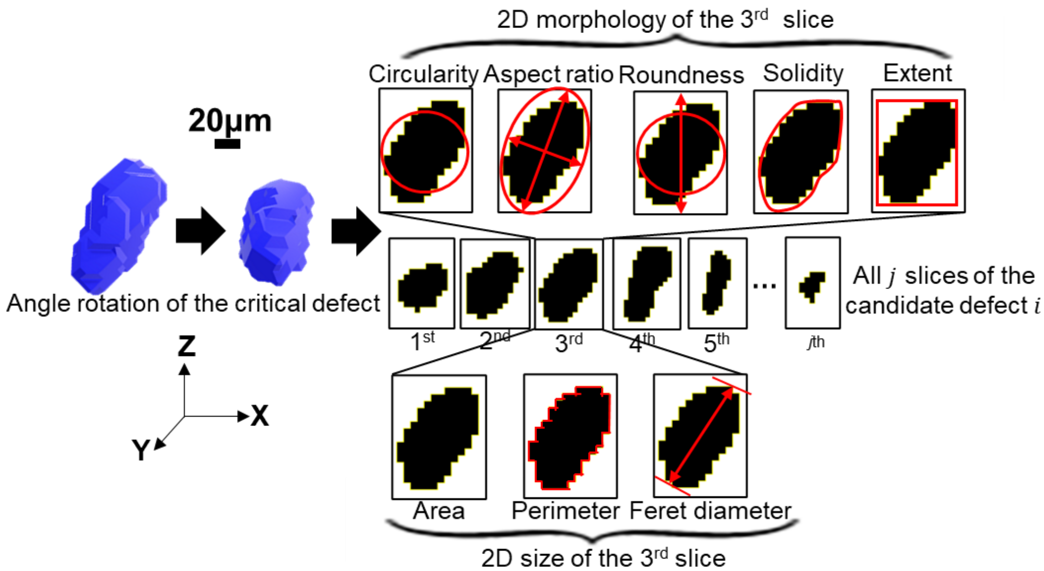

Figure 27 Illustration of angle rotation of a candidate defect in the XCT scans around X-axis and defect features, which characterize the 2D size and morphology of the candidate defect, being extracted from the projected areas of its slices on the XY plane.

5.2.2 Candidate defect selection by thresholds of positions

In this step, thresholds that limit the differences in the Z-locations and distances from the surface between the critical defect and the volumetric defects are set to select candidate defects with similar positions as the critical defect. In this study, a large difference (i.e., ±1000μm) is allowed between the Z-locations of the critical defect and the candidate defects (the Z-location of the critical defect is estimated by the Z-location of the fracture surface with moderate errors), while a relatively smaller difference (i.e., ±50μm) between their distances from the surface (the distance from the surface is measured accurately from the defects).

Moreover, if available, the relative position between the critical defect to the reference (e.g., a copper tape) is also used to navigate the X- and Y-locations of the selected candidate defects in XCT scans. Figure 28 illustrates an example of using the relative position information to select a candidate defect with certain X- and Y-locations. In Figure 28(a), the copper tape attached to the surface (as the bright stripe) can be detected in the XCT scans of the L-PBF part. Meanwhile, as shown in Figure 28(b), the copper tape and critical defect are captured on the fracture surface, where the X- and Y-locations of the copper tape end (designated as $(x^{f}_{tape\_end},\ y^{f}_{tape\_end})$) and the centroid of the critical defect (designated as $((x_c, y_c))$ can be acquired. The Euclidean distance R between the copper tape end and the centroid of the critical defect can be calculated as follows:

$$R = \sqrt[2]{(x^{f}_{tape\_end} - x_c)^2 + (y^{f}_{tape\_end} - y_c)^2} \tag{16}$$

The position of the copper tape end on the XCT scans in Figure 28(a) can also be acquired as $(x^{XCT}_{tape\_end},\ y^{XCT}_{tape\_end})$. A possible area for the correct match with X- and Y-positions (designated as (x, y)) can be identified in Figure 28(a) by satisfying the following two constraints:

$$\begin{aligned}&(1)\sqrt[2]{(x^{XCT}_{tap\_end} - x)^2 + (y^{XCT}_{tape\_end} - y)^2} \leq R + R' \\ &(2)\ x < x^{XCT}_{tape\_end}\ and\ y > y^{XCT}_{tape\_end}\end{aligned} \tag{17}$$

where a threshold R' is set to 100μm in this work for the tolerance of the positional errors. Note that the second constraint needs to be adjusted according to different relative positions between the copper tape end and critical defect for other specimens. This possible area is used to facilitate the matching by selecting the candidate defects within this area. For instance, as shown in Figure 28(c), the volumetric defect in this area is selected as a candidate defect, which has similar relative positions to the copper tape as the critical defect.

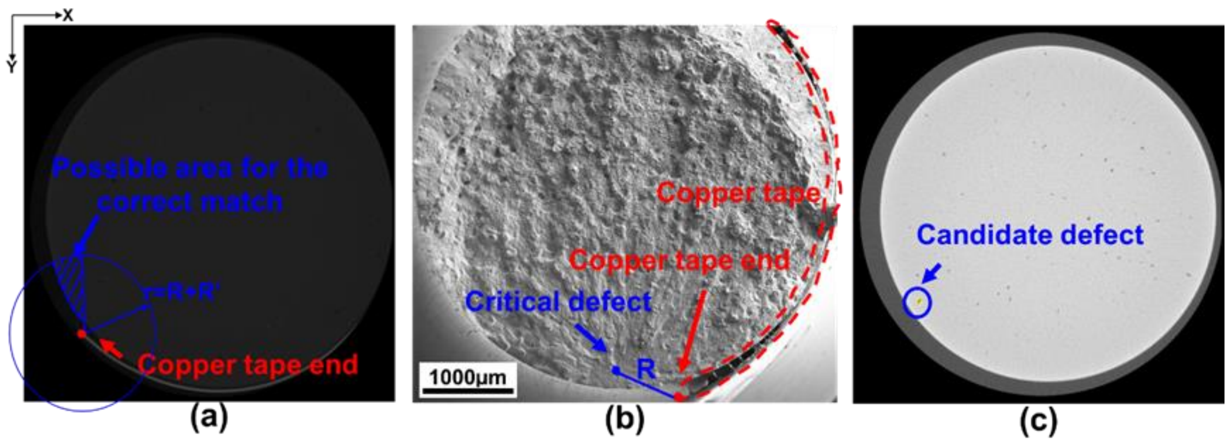

Figure 28 Illustration of using relative position between the critical defect and the copper tape to select a candidate defect with a similar position as the critical defect.

Through thresholding positions, we narrow the scope and significantly reduce the number of possible candidate volumetric defects for the critical defects, therefore improving the chance of identifying the correct match among the selected candidate defects for the critical defect. In the next step, the seven features describing the sizes and morphologies of the volumetric defects will also be used to calculate their DSs for identifying the correct match.

5.2.3 Candidate defect ranking by the Dissimilarity Scores

In this step, we aim to identify the candidate defect with the highest similarity to the critical defect in positions, sizes, and morphologies as the match. To fulfill this task, we develop a Dissimilarity Score (DS) to quantify the similarity between the critical defect and each candidate defect. It is noted that calculations of DS are slightly different with different feature extraction methods. For feature extraction from the projection, the DS of each candidate *i* is calculated by the following function:

$$DS_i^{projection} = w_1 \times D_i + w_2 \times S_i + (1 - w_1 - w_2) \times M_i \tag{18}$$

The adjustable weights w_1 and w_2, which determine the importance of positional, dimensional, and morphological dissimilarities in calculating the DS, range from 0 to 1. Besides, the sum of w_1 and w_2 is smaller and equal to one to guarantee the non-negative weight of the morphological dissimilarity. As a result, the candidate defect with the lowest DS is supposed to have the highest similarity to the critical defect, thus being identified as the match.

In this function, D_i is defined as positional dissimilarity, which measures the difference in the distances from the surface of the candidate defect *i* and the critical defect:

$$D_i = \sqrt[2]{(cd_i - d)} \tag{19}$$

where cd_i and d are the normalized distances from the surface of the candidate defect i and the critical defect, respectively. In this work, the min-max normalization is applied to scales all the eight features (i.e., distance from the surface, area, perimeter, Feret diameter, circularity, aspect ratio, extent and solidity) of the candidate defects and critical defect to a common range (e.g., from 0 to 1). In this case, the contribution of each feature to the calculation of DS can be more balanced and comparable, regardless of its original scale.

S_i is defined as dimensional dissimilarity, which measures the differences in the sizes of the projection of candidate defect *i* on the XY plane and the critical defect on the fracture surface, taking form of:

$$S_i = \sqrt[2]{\sum_{k=1}^{3} (cs_i^k - s^k)^2} \tag{20}$$

where cs_i^k and s^k (k =1,2,3) are the k^{th} normalized 2D feature (i.e., area, perimeter, Feret diameter) describing the size of the projection of the candidate defect i, and critical defect, respectively.

M_i is defined as the morphological dissimilarity, which measures the differences in the morphologies between all the projection of candidate defect *i* on the XY plane and the critical defect on the fracture surface, taking the form of:

$$M_i = \sqrt[2]{\sum_{l=1}^{5}(\, cm_i^l - m^l)^2} \tag{21}$$

where cm_i^l and m^l ($l = 1,2,34$) are the normalized l^{th} 2D features (i.e., circularity, aspect ratio, roundness, extent, and solidity) characterizing the morphologies of the projection of the candidate defect i, and the critical defect.

For feature extraction from the slices, the DS of each candidate *i* with *j* slices is calculated using the following function:

$$DS_{ij}^{slices} = w_1 \times D_i + w_2 \times S_{ij} + (1 - w_1 - w_2) \times M_{ij} \tag{22}$$

In this function, D_i is the positional dissimilarity calculated by the equation 18. S_{ij} and M_{ij} are the dimensional and morphological dissimilarities between the j^{th} slice of the candidate defect *i* and the critical defect. Among all *j* DSs for the candidate defect *i*, the smallest one is selected as the DS for the candidate defect *i*. Similarly, the candidate defect with the lowest DS is identified as the match to the critical defect.

$$DS_i^{slices} = Min(DS_{i1}^{slices}, DS_{i2}^{slices}, DS_{i3}^{slices} \ldots DS_{ij}^{slices}) \tag{23}$$

5.3 Case study

5.3.1 Experimental setup

In this work, an EOS M290 machine is employed to fabricate Ti-6Al-4V (Ti64) cylindrical parts for critical defect identification. The recommended process parameters of this machine for the Ti64 fabrication are 280W laser power, 1300mm/s scanning velocity, 40µm layer thickness, 120µm hatch distance, 67° layer rotation, and 10mm stripe width. Six different fabrication conditions are utilized to fabricate fourteen Ti64 parts with different types of defects (i.e., keyhole or lack of fusion) by non-optimal energy density, as summarized in Table 16. The as-built parts are stress-relived at 705°C for 1 hour with a heating rate of 5°C/minute in an electric furnace and furnace cooled before being removed from the build plate. Sequentially, they are machined to round fatigue testing specimens following standard ASTM E466 [238], shown in Figure 29.

Table 16 Three fabrication directions and six fabrication conditions used to fabricate sixteen L-PBF Ti64 for critical defect identification. To test the proposed procedure to identify different types of critical defects (i.e., keyholes or lack of fusion), those two types of defects are intentionally induced by non-optimal energy density levels.

Fabrication direction	Designation	Defect type	Energy density (J/mm^3)	Laser Power (W)	Scanning velocity (mm/s)	Hatch spacing (µm)	Fabricated specimens
Vertical	LaV	Lack of fusion	50.00	252	1200	140	LaV01, LaV02
	LbV	Lack of fusion	44.44	224	1200	140	LbV01
	LcV	Lack of fusion	46.29	280	1200	168	Lc01, Lc02, LcV03, LcV04, LcV05
	RV	Recommended	55.55	280	1200	140	RV01
	KaV	Keyhole	95.24	336	840	140	KaV01, KaV02, KaV03
	KbV	Keyhole	90.28	364	960	140	KbV01, KbV02
Horizontal	RH	Recommended	55.55	280	1200	140	RH01
Diagonal	RD	Recommended	55.55	280	1200	140	RD01

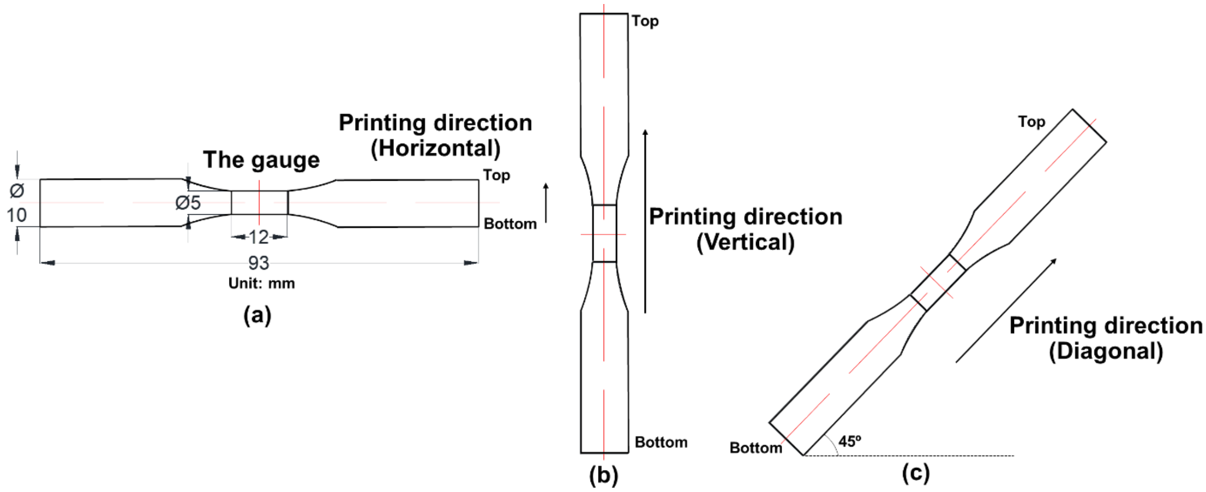

Figure 29 Geometry and dimension of the L-PBF fatigue test specimens (standard ASTM E466) used for critical defect identification in this study. Those L-PBF specimens are fabricated (a) horizontally, (b) vertically, and (c) diagonally from the bottom to the top.

The middle of the gage section (12mm length) of the specimen is XCT scanned by a Zeiss Xradia 620 Versa XCT machine. The XCT scanning is performed at 160 KV voltage and 21 W power, along with an X-ray filter to reduce the count of low-energy photons. For each scan, the voxel size is kept at ~ 5.5μm under all conditions. After XCT scanning, the volumetric tomography data are reconstructed by the Zeiss Xradia Reconstruction software to inspect the internal defects of the specimens. The reconstructed images of the XCT scans (i.e., the grayscale images) are binarized in ImageJ software for defect segmentation [239]. The binary function of ImageJ utilizes a fixed threshold of the intensity values to segment the volumetric defects (i.e., the voxel with low-intensity values below the threshold) from the surrounding materials in the grayscale images. Note that the features of the volumetric defects in the XCT scans are extracted from the segmented defects in the binary images.

5.3.2 The results of critical defect identification

To evaluate the accuracy of the proposed procedure, we validate the identification results manually by comparing the positions and morphologies of the critical defects and the identified matches in the original XCT scans (i.e., the grayscale images) with high confidence (original XCT scans will not sacrifice details of any defects). In contrast, the binarized images from the XCT scans might not accurately display some defects, as illustrated in Figure 30.

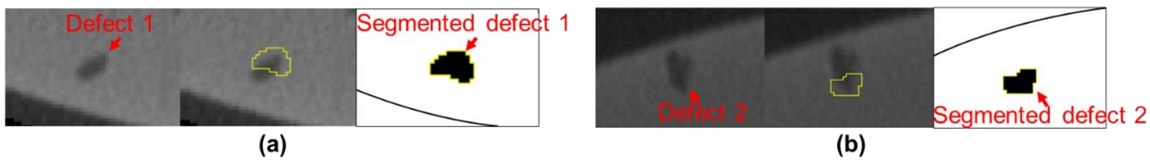

Figure 30 Illustration of inaccurate segmentation of two volumetric defects in the XCT scans. It is observed that the segmented defects in the binary images have different morphologies and positions compared to the volumetric defects in the grayscale images.

To compare with using Dissimilarity Score (DS) to identify the match among the candidate defects, a benchmark method, where the candidate defect with the lowest positional dissimilarity to the critical defect is identified as the match, is incorporated). For critical defect identification by the DS, the optimal weights w_1 and w_2 (representing the importance of positional, dimensional, and morphological dissimilarities in calculating the DS, see equation 17 and 21) are found by grid searches. Table 17 summarizes the critical defect identification results for sixteen L-PBF specimens with the benchmark method and DS calculated with two feature extraction methods (i.e., from the projection or slides). The benchmark method has an accuracy of 37.5% (6 out of 16) in critical defect identification. The highest accuracy of critical defect identification using the features extracted from the projection is 68.75% (11 out of 16) when w_1=0.2, w_2 =0.6 or 0.7 and w_1 =0.3, w_2=0.6 or 0.7, indicating the highest weight of the dimensional dissimilarity (60~70%), lower weight of the positional dissimilarity (20~30%) and the morphological dissimilarity (0~30%) in calculating the DS. For using the features extracted from the slices, the highest accuracy of critical defect identification is 81.25% (13 out of 16) when w_1=0.1, w_2=0.9, indicating the highest weight of the dimensional dissimilarity (90%), lower weight of the positional dissimilarity (10%) and no weight of the morphological dissimilarity (0%). Based on the optimal values of the weights w_1 and w_2, using features extracted from the projection leads to a more robust way to calculate the DS for critical defect identification by incorporating the positional, dimensional and morphological dissimilarities. However, using the features extracted from the slices results in higher identification accuracy without the morphological dissimilarity. In this case, this method is used in the proposed defect matching process to identify the matches among the candidate defects.

Table 17 Critical defect identification results for the sixteen L-PBF specimens with benchmark method, using Dissimilarity Score (DS) calculated by features extracted from the projection and slices. To calculate the DS for identifying the matches, the weights w_1 and w_2 are optimized to achieve the highest accuracy. For feature extraction from the slices, the rotated angles, which lead to the largest projected areas of the matches on certain slices, are also included.

Feature extraction method	Critical defect identification results (Y: correctly identified)															
	LbV01	LcV01	LcV02	LcV03	LcV04	LcV05	LaV01	LaV02	RV01	KaV01	KaV02	KaV03	KbV01	KbV02	RH01	RD01
Benchmark							Y		Y		Y		Y	Y	Y	
Projection				Y	Y	Y	Y	Y	Y	Y	Y		Y	Y	Y	
Slices	Y	Y			Y	Y	Y	Y	Y	Y	Y	Y	Y	Y	Y	
Rotated angles	23.5 º	15.4 º	-	11.1 º	16.6 º	21.0 º	37.5 º	14.9 º	-	23.5 º	12.9 º	46.1 º	-	-	-	-

Besides, Table 17 also summarizes the rotated angles for the identified match to the critical defect in each specimen. Since only single candidate defect with similar position as the critical defect has been selected by thresholds of positions, it is unnecessary to calculate the DSs of those candidate defects from the features extracted from their projections or slices. On the other hand, no candidate defect with similar position as the critical defect can be found within the XCT scans of the gauge for specimens LcV02 and RD01. More detailed identification results will be discussed in Section 5.3.2.1 and 5.3.2.2.

5.3.2.1 Specimens with the correctly identified matches to the critical defects

Among the thirteen specimens with the matches being correctly identified by the proposed process, the relative position information (provided by the copper tape) between the critical defects and the candidate defects are unavailable for the candidate defect selection of two specimens (i.e., La02 and Lc01). In this case, those thirteen specimens can be divided into two scenarios by the availability of the relative position information: Scenario 1: two specimens without relative position information. Scenario 2: eleven specimens with relative position information. Given the useful information provided by the relative position information to narrow down the X- and Y-locations of the candidate defects, we are more confident about the identification results for the eleven specimens in Scenario 2.

Scenario 1. Two specimens without relative position information

The relative position information is unavailable for two specimens La02 and Lc01, when the copper tape is removed before fatigue testing. Figure 31 illustrates the critical defects of these two specimens and their contours on the fracture surfaces. Figure 32 shows the matches identified by the proposed process and their contours in the grayscale images.

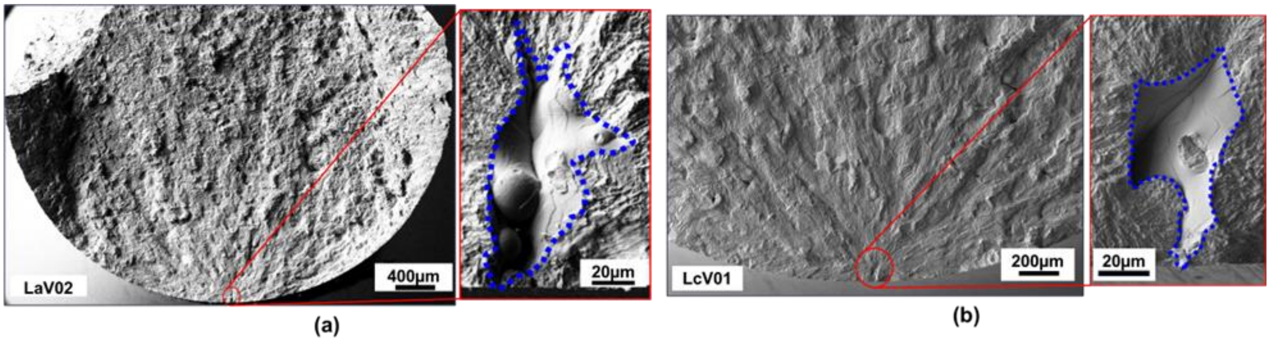

Figure 31 The critical defects of the specimens (a) LaV02 and (b) LcV01on the fracture surfaces and their contours. The relative position information is unavailable for these two specimens when the copper tape is removed before fatigue testing.

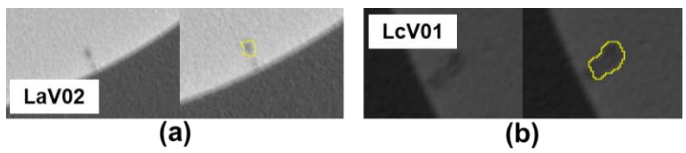

Figure 32 The identified matches to the critical defects of specimen (a) LaV02 and (b) LcV01 in the grayscale images. The yellow contours show the morphologies of those CDs in the binary images.

For specimen LaV02, it can be observed in Figure 31(a) and Figure 32(a) that the identified match shows a similar position (i.e., distance from the surface) and morphology in the grayscale images as the critical defect on the fracture surface. Like the critical defect, the match is also a surface defect, elongated and oriented towards the center of the specimen. Although it can also be observed from the defect contour in Figure 31(a) that the identified match is incompletely represented in the binary image, the proposed process can correctly identify the match to the critical defect using the DS calculated by the 2D features extracted from the slices. Besides, for specimen LcV01, it can also be observed in Figure 31(b) and Figure 32(b) that the identified match is similarly close to the surface and elongated as the critical defect on the fracture surface.

Scenario 2. Eleven specimens without relative position information

For the other eleven specimens (i.e., LaV01, LbV01, LcV04, LcV05, RV01, RH01, KaV01, KaV02, KaV03, KbV01, and KbV02) with relative position information, the correct matches to the critical defects can also be identified among the candidate defects by the proposed process.

The fabrication conditions (see Table 16) of these eleven specimens and the critical defects and their contours illustrated in Figure 33 and Figure 34 indicate that energy density levels of the specimens mostly determine the types (i.e., lack of fusion or keyhole) of those critical defects. Based on the 2D sizes and morphologies observed from the contours, the critical defects of four specimens fabricated with insufficient energy density levels (i.e., LaV01, LcV05, LbV01, LcV04) and two recommended ones (i.e., RV01 and RH01) can be classified as lack of fusions due to their irregular or elongated shapes [39, 46, 55]. On the other hand, the critical defects of the four specimens fabricated with excessive energy density levels (i.e., KaV01, KaV02, KbV01, and KbV02) can be classified as keyholes based on their relatively spherical shapes [39, 152, 205]. It is difficult to classify the critical defect of specimen KaV03 to lack of fusion or keyhole only based on its contour outlined on the fracture surface. Besides, all those critical defects have a large size (Feret diameter≥50μm) and are the most detrimental to the structural integrity of the L-PBF parts, which agrees with the observation in studies [103, 104].

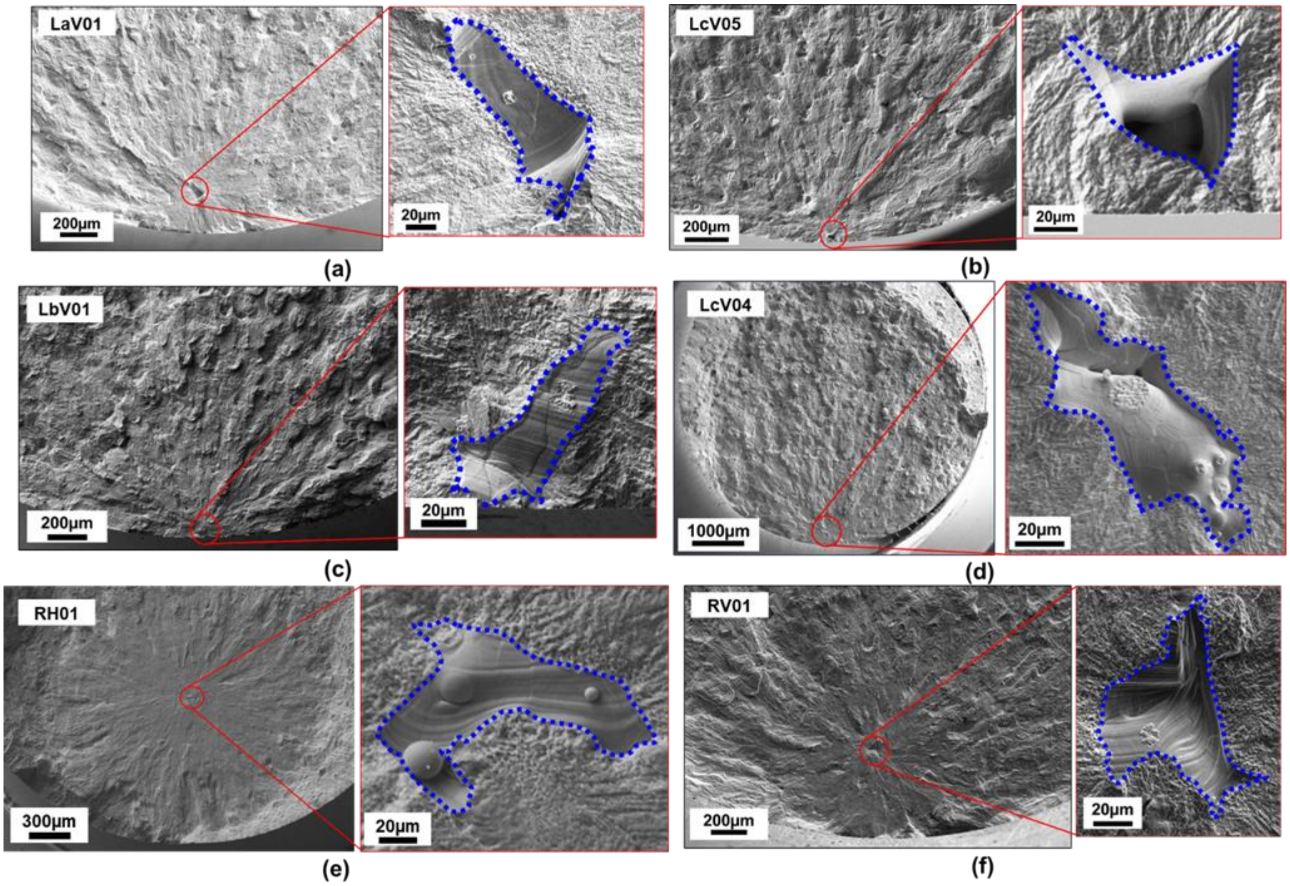

Figure 33 The critical defects of specimens (a) LaV01, (b) LcV05, (c) LbV01, (d) LcV04, (e) RH01 and (f) RV01 observed on the fracture surfaces and their contours. These six critical defects can be classified as lack of fusions due to their elongated or irregular shapes.

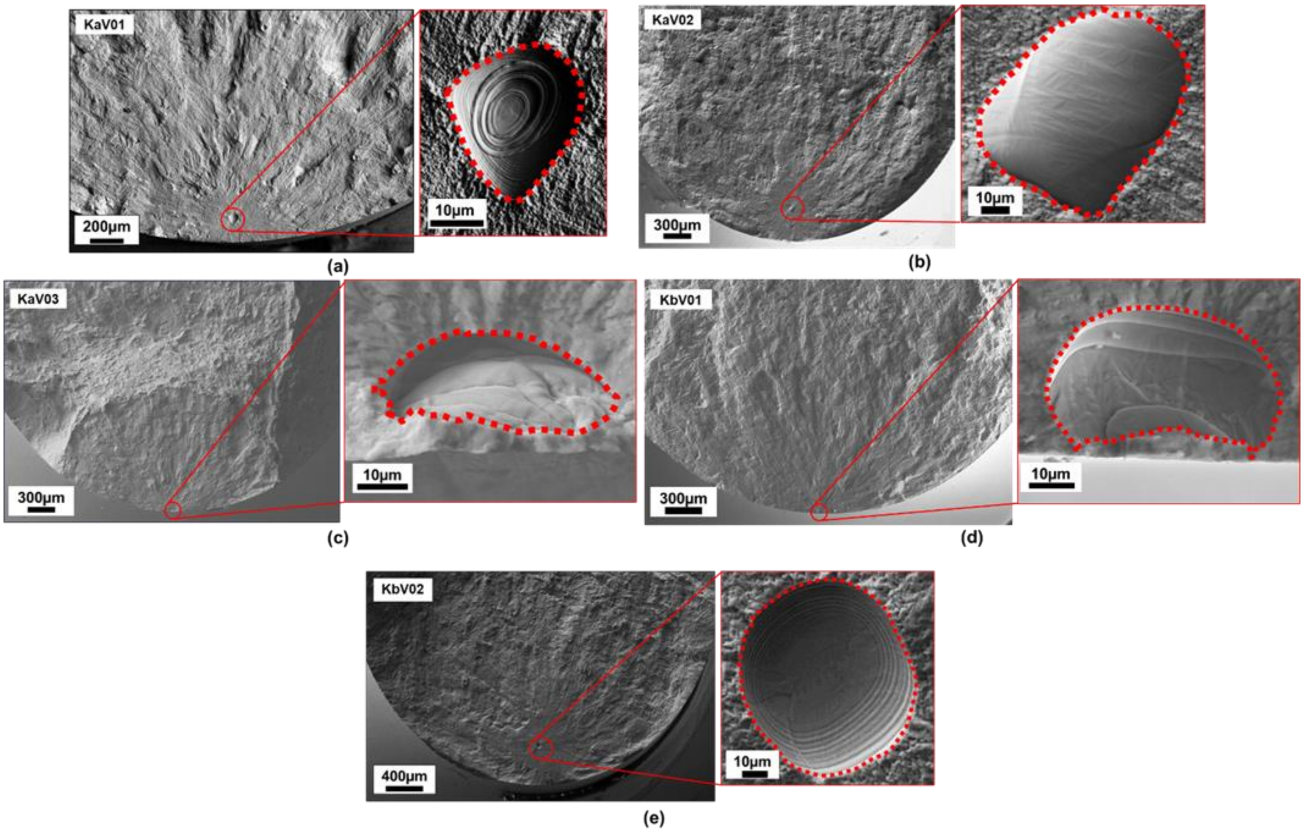

Figure 34 The critical defects of specimens (a) KaV01, (b) KaV02, (c) KaV03, (d) KbV01, and (e) KbV02 observed on the fracture surfaces and their contours. These five critical defects (except the one of specimen KaV03) can be classified as keyholes due to their relatively spherical shapes. It is difficult to classify the type of critical defect in specimen KaV03 only based on its contour outlined on the fracture surface.

The total numbers of volumetric defects in those eleven specimens are also related to the energy density levels, which can further affect the identification results. Table 18 summarizes the total numbers of the volumetric defects and the candidate defects from those eleven specimens fabricated with different energy density levels. A large number of volumetric defects are detected in the specimens fabricated with insufficient energy density levels (i.e., specimens LbV01, LcV04, LcV05, and LaV01).

With increased energy density levels, the numbers of volumetric defects reduce significantly and reach the lowest of 177 when the energy density is 90.28J/mm^3 for specimen

KbV02. It is probably because high energy density results in sufficient heat transfer and good fluidity to diminish the lack of fusions caused by partially melted powder particles [240]. However, a higher energy density of 95.24J/mm^3 can induce more keyholes to increase the number of volumetric defects [98, 208]. It seems fewer candidate defects with similar positions as the critical defects can be selected from the specimens with fewer volumetric defects. For instance, for specimens RV01, RH01, KbV01 and KbV02 with fewer volumetric defects being detected in the XCT scans, only single candidate defect has been selected in the proposed process for critical defect identification.

Table 18 The numbers of volumetric defects and candidate defects with similar positions as the critical defects for the specimens fabricated with different energy density levels.

Specimens	Energy density (J/mm3)	Volumetric defect numbers	Candidate defect number(s)
LbV01	44.44	44027	12
LcV04	46.29	27732	10
LcV05	46.29	50400	14
LaV01	50.00	10058	9
RV01	55.55	1301	1
RH01	55.55	1508	1
KbV01	90.28	340	1
KbV02	90.28	177	1
KaV01	95.24	5731	7
KaV02	95.24	2664	4
KaV03	95.24	3751	6

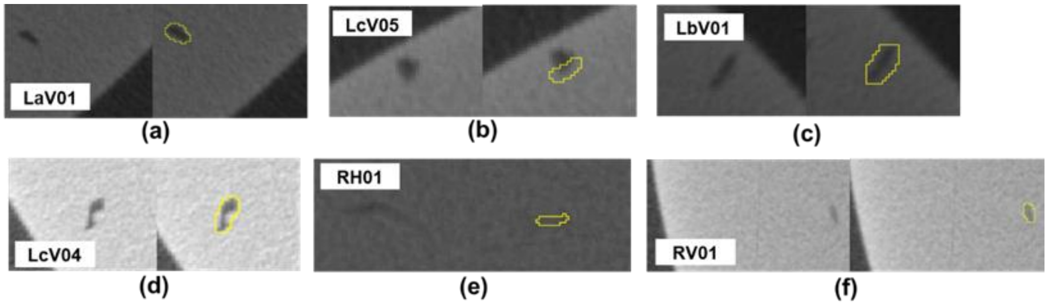

Figure 35 The inspection of identified matches for specimens (a) LaV01, (b) LcV05, (c) LbV01, (d) LcV04, (e) RH01, and (f) RV01 in the grayscale images of the XCT scans for validating the identification results. The yellow contours show the morphologies of those identified matches in the binary images. The identified matches in this Figure correspond to the critical defects in Figure 33.

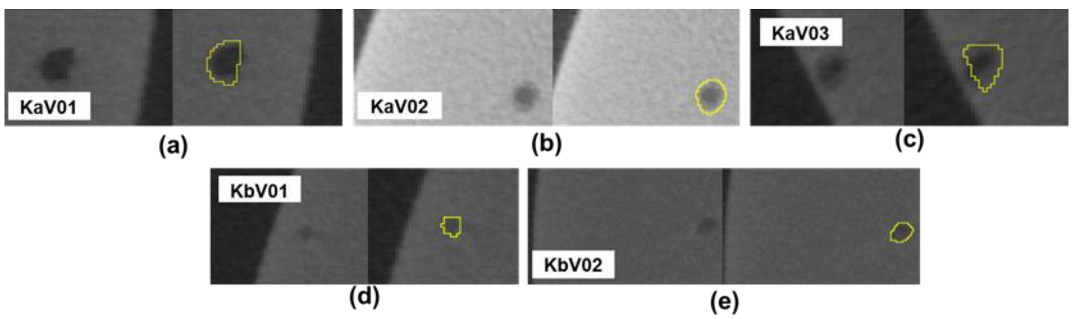

Figure 36 The inspection of identified matches for specimens (a) KaV01, (b) KaV02, (c) KaV03, (d) KbV01, and (e) KbV02 in the grayscale images of the XCT scans for validating the identification results. The yellow contours show the morphologies of those identified matches in the binary images. The identified matches in this Figure correspond to the critical defects in Figure 34.

To validate the identification results, we mainly compare the 2D morphologies and positions of the critical defects on the fracture surfaces (see Figure 33 and Figure 34) and the identified matches in the grayscale images of XCT scans (see Figure 35 and Figure 36). Figure 35 shows the identified matches corresponding to the six critical defects being classified as lack of fusions shown in Figure 33. It is observed that the identified matches of specimen LaV01, LcV04, and LbV01 are similarly elongated as the critical defects and one of specimen LcV05 also displays a similar triangle-like morphology as the critical defect. However, the identified matches of specimens RH01 and RV01 show a different morphology from the critical defects. Since only a single candidate defect is being selected for these two specimens, we still consider the identified matches the correct ones for the critical defect. A possible reason could be that the fineness of features of the irregularly shaped lack of fusions cannot be fully captured by the XCT scanning with low resolution, leading to inaccurate sizes and morphologies of those lack of fusions in the XCT scans, which has been reported in authors' previous work [152]. Moreover, those six identified matches can be observed to have a similar distance from the surface as the critical defects. Therefore, conclude that the matches are correctly identified to the critical defects of those six specimens.

Similarly, the rest five identified matches illustrated in Figure 36 also show similar morphology and position as critical defects except the ones for specimen KbV06. Since only one candidate defect has been selected for specimen KbV06, we consider it more likely to be the correct one than other volumetric defects in the XCT scans.

5.3.2.2 Specimens without correctly identified matches to the critical defects

The three specimens (LcV02, LcV03, and RD01) for which the proposed process fails to identify the correct matches to the critical defects can also be divided into two scenarios. Scenarios 1: for specimen LcV03, the correct match cannot be identified from the candidate defects due to a higher DS than other candidate defects. Scenarios 2: for specimen LcV02 and RD01, no candidate defects with similar positions to the critical defects can be found for the critical defect identification.

Scenario 1. One specimen with incorrectly identified match to the critical defect

For specimen LcV03, the correct match can be found among the candidate defects. However, an incorrect match is identified by the proposed process due to its lowest DS calculated with the optimized weights w_1 and w_2 (i.e., w_1=0.1 and w_2=0.9). Figure 37 illustrates the critical defect for specimen LcV03 and its contour. Figure 38 shows the five candidate defects (CDs) with the lowest DSs in the grayscale images of the XCT scans and their contours. It can be observed that CD2 is more likely to be the current match due to its similar position and morphology as the critical defect. However, it is found that a certain slice of CD1 has a lower dimensional dissimilarity (0.80) than CD2 (0.84) to the critical defect. Given the large weight of the dimensional dissimilarity (w_2=0.9) to calculate the DS, CD1 has the lower DS than CD2, thus being mistakenly identified as the match to the critical defect.

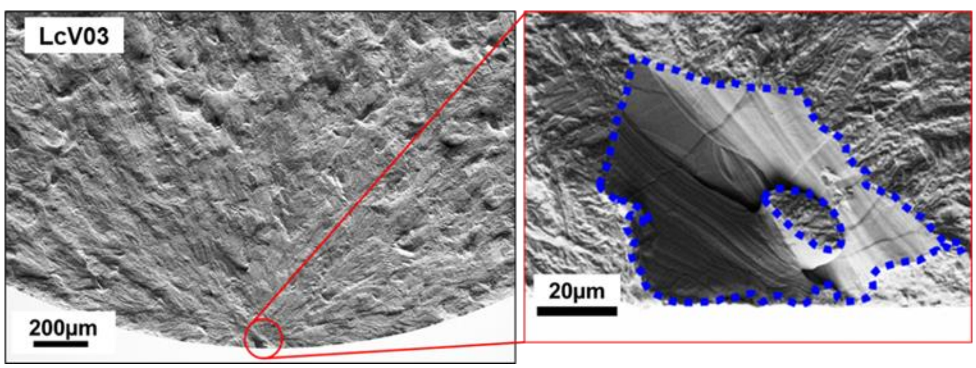

Figure 37 The critical defects of specimen LcV03 observed on the fracture surface and its contours.

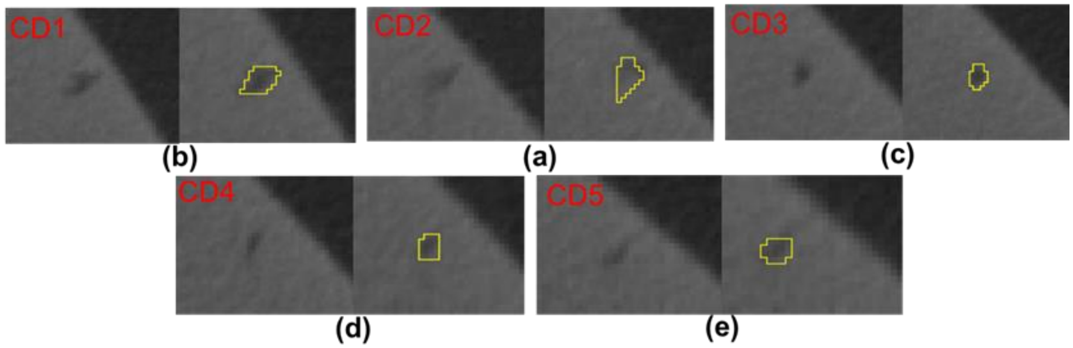

Figure 38 Inspection of the five candidate defects (CDs) with the lowest DSs for specimen LcV03 through the grayscale images of the XCT scans. The yellow contours show the morphologies of those CDs in the binary images. According to the grayscale images and contours of these five CDs, CD2 is most likely to be the correct match for the critical defect of specimen LcV03.

Scenario 2. Two specimens with no candidate defect for critical defect identification

For specimen LcV02 and RD01, no candidate defect with similar positions as the critical defects can be selected from the volumetric defects for critical defect identification. Figure 39 illustrates the critical defects and their contours outlined on the fracture surfaces. Given the critical defects of these two specimens are on the fracture surface located at the bottom of the gauge, we suspect that the matches might be out of the XCT scans of the gauge. For the critical defect of specimen LcV02, by inspecting the XCT scans with a larger scanned area, we find a volumetric defect with a similar distance from the surface and relative position to the copper tape as the critical defect, as shown in Figure 40. However, this defect has a Z-location roughly 1000μm below the gauge. In this case, it cannot be identified by the proposed process. For the critical defect of specimen RD01, given the relatively smaller size of the critical defect (see Figure 39(b)), we are unable to find a possible match even within a larger scanned area of the XCT scans.

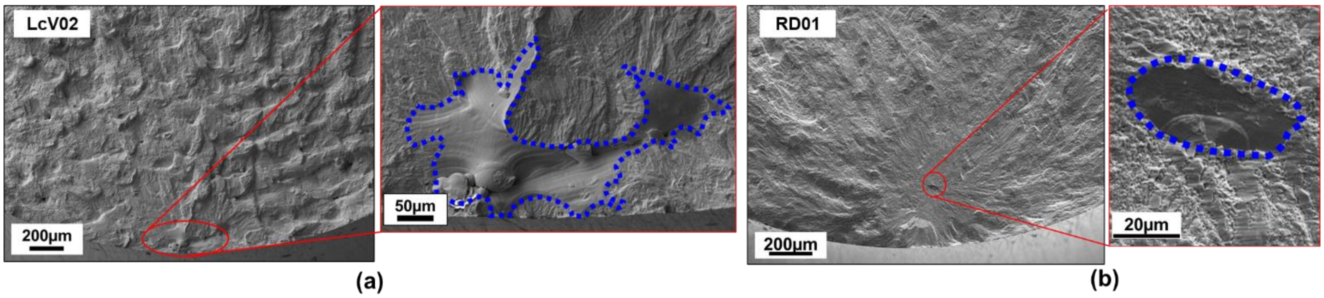

Figure 39 The critical defects of specimens (a) LcV02 and (b) RD01 observed on the fracture surface and its contours.

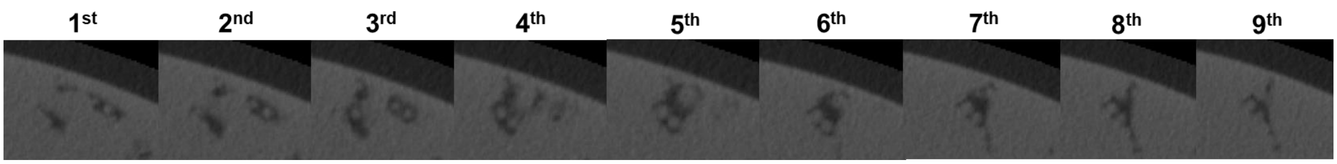

Figure 40 All slices of a possible match to the critical defect for specimen LcV02 in the grayscale images of the XCT scans. This possible match is observed to have a large size, similar relative position to the reference, and distance from the surface as the critical defect. However, it is located at 1000μm below the gauge in the XCT scans.

5.4 Conclusion and future works

In this chapter, we proposed a cross-dimensional (3D/2D) defect matching process to specifically identify the matches to the critical defects among numerous volumetric defects in the XCT scans for the L-PBF parts. Identifying the match to the critical defect not only reveals the important features of the critical defect, which contributes to the fatigue life of L-PBF parts but also opens the possibility of critical defect identification and fatigue life prediction non-destructively. The proposed process characterized the critical defect and the volumetric defects with their positions, sizes, and morphologies. Candidate defects with similar positions as the critical defect are selected from the volumetric defects. The proposed process used a self-developed Dissimilarity Score (DS) calculated from the weighted pairwise similarities between the critical defect observed on the fracture surface and the 2D projection or slices of each candidate defect to find the correct match with the lowest DS value. As a result, the proposed process achieved the highest accuracy of 81.25% to correctly identify the matches to the critical defects for thirteen out of sixteen specimens. Two misidentifications could be caused by the match not being in the XCT scans of the gauge. Another misidentification was caused by the inaccurate features of the volumetric defects due to the XCT scanning with low resolution.

To further improve the robustness and accuracy of critical defect identification and leverage the identification results for fatigue life analysis, two future research directions are proposed: To further improve the robustness accuracy of critical defect identification and leverage the identification results for fatigue life analysis, two future research directions are proposed:

(1) Develop new methods to extract features directly from the grayscale images for more accurate representations of the volumetric defects.
(2) Use the critical defect identification results to obtain the 3D defect features of the critical defects for fatigue performance analysis of the L-PBF parts.

6 Conclusion and future works

In this dissertation, three methodologies have been proposed and applied to two commonly used additive manufacturing (AM) processes, namely, fused filament fabrication (FFF) and laser beam powder bed fusion (L-PBF) processes for process optimization and quality prediction, respectively. The proposed methodologies collected the data of the FFF and L-PBF parts through photomicrography (i.e., optical microscope and scanning electron microscope) and tomography (i.e., X-ray computed tomography (XCT)) and integrated machine learning modeling (e.g., Gaussian process regression (GPR), *k*-nearest neighbor (*k*-NN)) and computational programming (e.g., Bayesian optimization algorithm, algorithmic models) to achieve process optimization and quality prediction in a data-driven manner. Some common challenges in the AM processes, such as the waste of time and materials in the design iterations of the trial-and-error approaches, the obstacles to non-destructive quality inspection and fatigue performance assessment, are addressed by the proposed methodologies, which can be more efficient than the conventional methods and applicable to different AM processes.

Specifically, in Chapter 3 of this dissertation, a nonparametric Bayesian framework is proposed to address two major limitations in designing and fabricating FFF ABS/graphene nanocomposite parts with superior surface quality: (1) the effects of graphene compositions on the quality of FFF parts are not fully revealed by limited experiments; (2) the role of FFF process parameters on successful nanocomposite design and fabrication is largely neglected. To this end, the proposed framework centering on the GPR and Bayesian optimization unified nanocomposite design and part fabrication and simultaneously optimized graphene composition and process parameters to achieve superior surface roughness of the FFF ABS/graphene parts. It verified and interpreted the impact of graphene composition and key process parameters (i.e., extruder temperature, print speed, and layer thickness) on the surface finish of the FFF parts experimentally and analytically. The GPR model outperformed the other three benchmark predictive methods to predict the surface roughness of the FFF parts in terms of the goodness of fit with the highest R2 value of 0.84) and the model accuracy with the smallest mean absolute percentage error of 0.13 and root mean squared error of 2.66. Permutation feature importance and accumulated local effects were incorporated to interpret the relationships among process parameters and material composition with surface roughness for “black-box” GPR, revealing that extruder temperature and print speed significantly impacted the surface roughness. Lastly, the optimal fabrication conditions could be found by the Bayesian optimization within six iterations of the FFF fabrication, which saves time and cost for the nanocomposite design. Compared to the trial-and-error approaches, it can explore the design space efficiently, discover new materials, and significantly reduce design time and cost. Besides, given its data-driven nature, the proposed framework can be readily generalized to different materials, properties, and processes for optimizing materials design and additive manufacturing.

In Chapter 4, a data-driven framework is proposed to bridge the existing research gaps of prohibitively high cost and inefficiency of the high resolution (HR)-XCT for non-destructive defect inspection and lack of defect characteristics-based defect classification for the L-PBF parts. The proposed framework augmented the low resolution (LR)-XCT defect inspection and classification with limited HR-XCT data to improve the efficiency and accuracy of the non-destructive defect inspection and classification for the L-PBF parts with LR-XCT scanning, paving the way to understand the impacts of defect on fatigue performance of L-PBF parts. Specifically, nine morphological features (solidity, sparseness, extent, sphericity, roundness, aspect ratio, elongation, flatness, and major axis length), which describe the morphologies and sizes of defects, are derived to distinguish different defect types and extracted from the LR- and HR-XCT scans. An algorithm for matching the same defects in LR-XCT and HR-XCT images is developed, which uses the defect positions and volumes to match with an accuracy exceeding 95%. The LR-XCT morphological features are augmented with regression-based features augmentation models, which build linear (using the multiple linear regression algorithm) or non-linear (using random forest and GPR algorithms) relationships between the LR-XCT and HR-XCT measurements. Significant improvements in defect classification accuracy by augmentation can be observed from a collection of classification models used in this chapter. Among those models, the k-NN classifier exhibits the best performance, with 82.9% accuracy for LR features only, which can be improved to 90.6% with augmentation. Furthermore, for the largest defects that are more important for the structural integrity, specifically the fatigue performance, the k-NN classifier can classify them with high accuracy of 96.3% using LR features with or without augmentation. The classification results showing the types of defects can be used as an effective non-destructive method to identify and improve the quality of L-PBF fabricated parts in future manufacturing.

In Chapter 5, a cross-dimensional (3D/2D) defect matching process is proposed to identify the critical defect from the numerous volumetric defects and enable non-destructive fatigue performance assessment. The proposed procedure characterized the 3D positions and 2D sizes and morphologies of the critical defect and volumetric defects and developed a Dissimilarity Score (DS) to quantify the pairwise similarities between the critical and each candidate defect to identify the correct match with the lowest DS value. The proposed procedure correctly identified the matches to the critical defects for eight out of fourteen L-PBF parts. Five misidentifications are caused by the inaccurate segmentation of near-surface or surface defects after binarization due to post-processing operations (e.g., boundary removal), and partial volume effect and another misidentification could be caused by the match not being in the XCT scans of the gauge. Identifying the match to the critical defect not only reveals the important features of the critical defect, which contributes to the fatigue life of L-PBF parts, but also opens the possibility of critical defect identification and fatigue life prediction non-destructively.

For future works, two research areas are of great interest based on this dissertation:

(1) Enhancement and validation of the proposed methodologies

For the first contribution (in Chapter 3), some advanced surface measuring instruments, such as optical profiler or stylus profiler, can be used for more precise measurement of the surface roughness, leading to improved modeling outcomes. For the second (in Chapter 4) and third (in Chapter 5) contributions, the proposed methodologies will be validated by the accuracy of the defect classification and critical defect identification, respectively, based on more data collected from the L-PBF parts. Besides, advanced approaches such as Convolutional Neural Networks and Semantic segmentation will be the candidates to obtain the defect features directly from the grayscale images of the XCT scans to prevent inaccurate defect features from the binary images. Applying those cutting-edge techniques can enhance the overall quality of the proposed methodologies with more reliable and accurate data.

(2) Extension of the works for further AM applications

The first contribution can be applied to the whole production cycle of the FFF process for quality prediction and process optimization of the nanocomposite filament synthesis and FFF manufacturing. Meanwhile, heterogeneous in-situs sensors, such as cameras and infrared sensors, will be integrated into the proposed nonparametric Bayesian framework to monitor the FFF fabrication process in real time and achieve feedback control to improve the product quality of nanocomposites in situ. The second contribution can be utilized to explore the optimal fabrication conditions of L-PBF parts with some innovative materials through the defect classification results. The third contribution can be employed for the nondestructive fatigue performance analysis of the L-PBF parts through the 3D defect features of the critical defects obtained after the critical defect identifications.

References

[1] W. E. Frazier, "Metal additive manufacturing: a review," *Journal of Materials Engineering and performance,* vol. 23, no. 6, pp. 1917-1928, 2014.

[2] H. Bikas, P. Stavropoulos, and G. Chryssolouris, "Additive manufacturing methods and modelling approaches: a critical review," *The International Journal of Advanced Manufacturing Technology,* vol. 83, no. 1, pp. 389-405, 2016.

[3] K. V. Wong and A. Hernandez, "A review of additive manufacturing," *International scholarly research notices,* vol. 2012, 2012.

[4] S. Vock, B. Klöden, A. Kirchner, T. Weißgärber, and B. Kieback, "Powders for powder bed fusion: a review," *Progress in Additive Manufacturing,* vol. 4, no. 4, pp. 383-397, 2019.

[5] S. Sing and W. Yeong, "Laser powder bed fusion for metal additive manufacturing: perspectives on recent developments," *Virtual and Physical Prototyping,* vol. 15, no. 3, pp. 359-370, 2020.

[6] V. Bhavar, P. Kattire, V. Patil, S. Khot, K. Gujar, and R. Singh, "A review on powder bed fusion technology of metal additive manufacturing," *Additive manufacturing handbook,* pp. 251-253, 2017.

[7] R. Singh *et al.*, "Powder bed fusion process in additive manufacturing: An overview," *Materials Today: Proceedings,* vol. 26, pp. 3058-3070, 2020.

[8] A. P. Nagalingam, J.-Y. Lee, and S. Yeo, "Multi-jet hydrodynamic surface finishing and X-ray computed tomography (X-CT) inspection of laser powder bed fused Inconel 625 fuel injection/spray nozzles," *Journal of Materials Processing Technology,* vol. 291, p. 117018, 2021.

[9] R. Liu, Z. Wang, T. Sparks, F. Liou, and J. Newkirk, "Aerospace applications of laser additive manufacturing," in *Laser additive manufacturing*: Elsevier, 2017, pp. 351-371.

[10] J. C. Najmon, S. Raeisi, and A. Tovar, "Review of additive manufacturing technologies and applications in the aerospace industry," *Additive manufacturing for the aerospace industry,* pp. 7-31, 2019.

[11] S. Singh, S. Ramakrishna, and R. Singh, "Material issues in additive manufacturing: A review," *Journal of Manufacturing Processes,* vol. 25, pp. 185-200, 2017.

[12] M. Seifi, A. Salem, J. Beuth, O. Harrysson, and J. J. Lewandowski, "Overview of materials qualification needs for metal additive manufacturing," *Jom,* vol. 68, no. 3, pp. 747-764, 2016.

[13] T. D. Ngo, A. Kashani, G. Imbalzano, K. T. Nguyen, and D. Hui, "Additive manufacturing (3D printing): A review of materials, methods, applications and challenges," *Composites Part B: Engineering,* vol. 143, pp. 172-196, 2018.

[14] I. Campbell, D. Bourell, and I. Gibson, "Additive manufacturing: rapid prototyping comes of age," *Rapid prototyping journal,* 2012.

[15] K. S. Intelligence, "Additive Manufacturing Market Size, Share, Opportunities, COVID 19 Impact, And Trends By Component (Hardware, Software, Services, Material), By Technology (Selective Laser Sintering (SLS), Laser Sintering (LS), Electron Beam Melting (EBM), Fused Disposition Modelling, Stereolithography (SLA)), By End-User Industry (Aerospace And Defense, Healthcare, Automotive, Construction, Consumer, Others), And By Geography - Forecasts From 2022 To 2027," 2022. [Online]. Available: https://www.knowledge-sourcing.com/report/additive-manufacturing-market

[16] A. J. Morgan *et al.*, "Simple and versatile 3D printed microfluidics using fused filament fabrication," *PloS one,* vol. 11, no. 4, p. e0152023, 2016.
[17] G. A. Longhitano, G. B. Nunes, G. Candido, and J. V. L. da Silva, "The role of 3D printing during COVID-19 pandemic: a review," *Progress in additive manufacturing,* vol. 6, no. 1, pp. 19-37, 2021.
[18] R. C. Advincula *et al.*, "Additive manufacturing for COVID-19: devices, materials, prospects, and challenges," *Mrs Communications,* vol. 10, no. 3, pp. 413-427, 2020.
[19] E. Larrañeta, J. Dominguez-Robles, and D. A. Lamprou, "Additive manufacturing can assist in the fight against COVID-19 and other pandemics and impact on the global supply chain," *3D Printing and Additive Manufacturing,* vol. 7, no. 3, pp. 100-103, 2020.
[20] R. Tino *et al.*, "COVID-19 and the role of 3D printing in medicine," vol. 6, ed: BioMed Central, 2020, pp. 1-8.
[21] C. Liu, A. C. C. Law, D. Roberson, and Z. J. Kong, "Image analysis-based closed loop quality control for additive manufacturing with fused filament fabrication," *Journal of Manufacturing Systems,* vol. 51, pp. 75-86, 2019.
[22] K. Rashed, A. Kafi, R. Simons, and S. Bateman, "Fused filament fabrication of nylon 6/66 copolymer: Parametric study comparing full factorial and Taguchi design of experiments," *Rapid Prototyping Journal,* 2022.
[23] A. C. de Bruijn, G. Gómez-Gras, and M. A. Pérez, "On the effect upon the surface finish and mechanical performance of ball burnishing process on fused filament fabricated parts," *Additive Manufacturing,* vol. 46, p. 102133, 2021.
[24] R. Anitha, S. Arunachalam, and P. Radhakrishnan, "Critical parameters influencing the quality of prototypes in fused deposition modelling," *Journal of materials processing technology,* vol. 118, no. 1-3, pp. 385-388, 2001.
[25] Z. Zhang, I. Fidan, and M. Allen, "Detection of Material Extrusion In-Process Failures via Deep Learning," *Inventions,* vol. 5, no. 3, p. 25, 2020. [Online]. Available: https://www.mdpi.com/2411-5134/5/3/25.
[26] B. N. Narayanan, K. Beigh, G. Loughnane, and N. Powar, "Support vector machine and convolutional neural network based approaches for defect detection in fused filament fabrication," in *Applications of Machine Learning*, 2019, vol. 11139: SPIE, pp. 283-291.
[27] S. Singh, G. Singh, C. Prakash, and S. Ramakrishna, "Current status and future directions of fused filament fabrication," *Journal of Manufacturing Processes,* vol. 55, pp. 288-306, 2020.
[28] M. Taufik and P. K. Jain, "A study of build edge profile for prediction of surface roughness in fused deposition modeling," *Journal of Manufacturing Science and Engineering,* vol. 138, no. 6, 2016.
[29] J. Liu, J. Ye, D. Silva Izquierdo, A. Vinel, N. Shamsaei, and S. Shao, "A review of machine learning techniques for process and performance optimization in laser beam powder bed fusion additive manufacturing," *Journal of Intelligent Manufacturing,* pp. 1-27, 2022.
[30] N. Sohrabi *et al.*, "Characterization, mechanical properties and dimensional accuracy of a Zr-based bulk metallic glass manufactured via laser powder-bed fusion," *Materials & Design,* vol. 199, p. 109400, 2021.
[31] S. C. Altıparmak, V. A. Yardley, Z. Shi, and J. Lin, "Challenges in additive manufacturing of high-strength aluminium alloys and current developments in hybrid

additive manufacturing," *International Journal of Lightweight Materials and Manufacture,* vol. 4, no. 2, pp. 246-261, 2021.
[32] T. I. team. "Aerospace Sector." https://www.investopedia.com/ask/answers/041415/what-aerospace-sector.asp (accessed.
[33] T. Kellner, "An epiphany of disruption: GE additive chief explains how 3D printing will upend manufacturing," *GE Reports,* vol. 13, 2017.
[34] M. Sow *et al.*, "Influence of beam diameter on Laser Powder Bed Fusion (L-PBF) process," *Additive Manufacturing,* vol. 36, p. 101532, 2020.
[35] H. Lee, C. H. J. Lim, M. J. Low, N. Tham, V. M. Murukeshan, and Y. Kim, "Lasers in additive manufacturing: A review," *International Journal of Precision Engineering and Manufacturing-Green Technology,* vol. 4, no. 3, pp. 307-322, 2017.
[36] S. A. Khairallah, A. T. Anderson, A. Rubenchik, and W. E. King, "Laser powder-bed fusion additive manufacturing: Physics of complex melt flow and formation mechanisms of pores, spatter, and denudation zones," *Acta Materialia,* vol. 108, pp. 36-45, 2016.
[37] A. Mostafaei *et al.*, "Defects and anomalies in powder bed fusion metal additive manufacturing," *Current Opinion in Solid State and Materials Science,* vol. 26, no. 2, p. 100974, 2022.
[38] P. Nezhadfar, K. Anderson-Wedge, S. Daniewicz, N. Phan, S. Shao, and N. Shamsaei, "Improved high cycle fatigue performance of additively manufactured 17-4 PH stainless steel via in-process refining micro-/defect-structure," *Additive Manufacturing,* vol. 36, p. 101604, 2020.
[39] R. Snell *et al.*, "Methods for rapid pore classification in metal additive manufacturing," *JOM,* vol. 72, no. 1, pp. 101-109, 2020.
[40] H. Gong, K. Rafi, H. Gu, T. Starr, and B. Stucker, "Analysis of defect generation in Ti–6Al–4V parts made using powder bed fusion additive manufacturing processes," *Additive Manufacturing,* vol. 1-4, pp. 87-98, 2014.
[41] G. Kasperovich, J. Haubrich, J. Gussone, and G. Requena, "Correlation between porosity and processing parameters in TiAl6V4 produced by selective laser melting," *Materials & Design,* vol. 105, pp. 160-170, 2016.
[42] J. V. Gordon *et al.*, "Defect structure process maps for laser powder bed fusion additive manufacturing," *Additive Manufacturing,* vol. 36, p. 101552, 2020.
[43] J. Zhu, E. Borisov, X. Liang, E. Farber, M. Hermans, and V. Popovich, "Predictive analytical modelling and experimental validation of processing maps in additive manufacturing of nitinol alloys," *Additive Manufacturing,* vol. 38, p. 101802, 2021.
[44] A. Yadollahi and N. Shamsaei, "Additive manufacturing of fatigue resistant materials: Challenges and opportunities," *International Journal of Fatigue,* vol. 98, pp. 14-31, 2017.
[45] Y. Yamashita, T. Murakami, R. Mihara, M. Okada, and Y. Murakami, "Defect analysis and fatigue design basis for Ni-based superalloy 718 manufactured by selective laser melting," *International Journal of Fatigue,* vol. 117, pp. 485-495, 2018.
[46] R. Cunningham, S. P. Narra, C. Montgomery, J. Beuth, and A. Rollett, "Synchrotron-based X-ray microtomography characterization of the effect of processing variables on porosity formation in laser power-bed additive manufacturing of Ti-6Al-4V," *Jom,* vol. 69, no. 3, pp. 479-484, 2017.
[47] B. Zhang, Y. Li, and Q. Bai, "Defect formation mechanisms in selective laser melting: a review," *Chinese Journal of Mechanical Engineering,* vol. 30, no. 3, pp. 515-527, 2017.

[48] H. Gong, K. Rafi, H. Gu, T. Starr, and B. Stucker, "Analysis of defect generation in Ti–6Al–4V parts made using powder bed fusion additive manufacturing processes," *Additive Manufacturing,* vol. 1, pp. 87-98, 2014.
[49] M. Brennan, J. Keist, and T. Palmer, "Defects in Metal Additive Manufacturing Processes," *Journal of Materials Engineering and Performance,* vol. 30, no. 7, pp. 4808-4818, 2021.
[50] Y. Hu *et al.*, "The effect of manufacturing defects on the fatigue life of selective laser melted Ti-6Al-4V structures," *Materials & Design,* vol. 192, p. 108708, 2020.
[51] S. Romano, A. Brückner-Foit, A. Brandão, J. Gumpinger, T. Ghidini, and S. Beretta, "Fatigue properties of AlSi10Mg obtained by additive manufacturing: Defect-based modelling and prediction of fatigue strength," *Engineering Fracture Mechanics,* vol. 187, pp. 165-189, 2018.
[52] A. J. Sterling, B. Torries, N. Shamsaei, S. M. Thompson, and D. W. Seely, "Fatigue behavior and failure mechanisms of direct laser deposited Ti–6Al–4V," *Materials Science and Engineering: A,* vol. 655, pp. 100-112, 2016.
[53] S. Leuders *et al.*, "On the mechanical behaviour of titanium alloy TiAl6V4 manufactured by selective laser melting: Fatigue resistance and crack growth performance," *International Journal of Fatigue,* vol. 48, pp. 300-307, 2013.
[54] A. du Plessis, I. Yadroitsava, and I. Yadroitsev, "Effects of defects on mechanical properties in metal additive manufacturing: A review focusing on X-ray tomography insights," *Materials & Design,* vol. 187, p. 108385, 2020.
[55] S. Coeck, M. Bisht, J. Plas, and F. Verbist, "Prediction of lack of fusion porosity in selective laser melting based on melt pool monitoring data," *Additive Manufacturing,* vol. 25, pp. 347-356, 2019.
[56] J. Pegues *et al.*, "Fatigue of additive manufactured Ti-6Al-4V, Part I: The effects of powder feedstock, manufacturing, and post-process conditions on the resulting microstructure and defects," *International Journal of Fatigue,* vol. 132, p. 105358, 2020.
[57] R. Molaei *et al.*, "Fatigue of additive manufactured Ti-6Al-4V, Part II: The relationship between microstructure, material cyclic properties, and component performance," *International Journal of Fatigue,* vol. 132, p. 105363, 2020.
[58] D. Greitemeier, F. Palm, F. Syassen, and T. Melz, "Fatigue performance of additive manufactured TiAl6V4 using electron and laser beam melting," *International Journal of Fatigue,* vol. 94, pp. 211-217, 2017.
[59] T. M. Mower and M. J. Long, "Mechanical behavior of additive manufactured, powder-bed laser-fused materials," *Materials Science and Engineering: A,* vol. 651, pp. 198-213, 2016.
[60] A. B. Spierings, T. L. Starr, and K. Wegener, "Fatigue performance of additive manufactured metallic parts," *Rapid prototyping journal,* 2013.
[61] N. Sanaei and A. Fatemi, "Defects in additive manufactured metals and their effect on fatigue performance: a state-of-the-art review," *Progress in Materials Science,* vol. 117, p. 100724, 2021.
[62] B. Blakey-Milner *et al.*, "Metal additive manufacturing in aerospace: A review," *Materials & Design,* vol. 209, p. 110008, 2021.
[63] J. J. Lewandowski and M. Seifi, "Metal additive manufacturing: A review of mechanical properties (postprint)," 2016.

[64] M. Seifi *et al.*, "Progress towards metal additive manufacturing standardization to support qualification and certification," *Jom,* vol. 69, no. 3, pp. 439-455, 2017.
[65] P. Li, D. Warner, A. Fatemi, and N. Phan, "Critical assessment of the fatigue performance of additively manufactured Ti–6Al–4V and perspective for future research," *International Journal of Fatigue,* vol. 85, pp. 130-143, 2016.
[66] S. Beretta and S. Romano, "A comparison of fatigue strength sensitivity to defects for materials manufactured by AM or traditional processes," *International Journal of Fatigue,* vol. 94, pp. 178-191, 2017.
[67] S. Romano, P. Nezhadfar, N. Shamsaei, M. Seifi, and S. Beretta, "High cycle fatigue behavior and life prediction for additively manufactured 17-4 PH stainless steel: Effect of sub-surface porosity and surface roughness," *Theoretical and Applied Fracture Mechanics,* vol. 106, p. 102477, 2020.
[68] P. Nezhadfar *et al.*, "Fatigue crack growth behavior of additively manufactured 17-4 PH stainless steel: Effects of build orientation and microstructure," *International Journal of Fatigue,* vol. 123, pp. 168-179, 2019.
[69] A. Yadollahi, N. Shamsaei, S. M. Thompson, A. Elwany, and L. Bian, "Effects of building orientation and heat treatment on fatigue behavior of selective laser melted 17-4 PH stainless steel," *International Journal of Fatigue,* vol. 94, pp. 218-235, 2017.
[70] N. Shamsaei and J. Simsiriwong, "Fatigue behaviour of additively-manufactured metallic parts," *Procedia Structural Integrity,* vol. 7, pp. 3-10, 2017.
[71] M. Spoerk, J. Gonzalez-Gutierrez, J. Sapkota, S. Schuschnigg, and C. Holzer, "Effect of the printing bed temperature on the adhesion of parts produced by fused filament fabrication," *Plastics, Rubber and Composites,* vol. 47, no. 1, pp. 17-24, 2018.
[72] Y. Zhang, S. Bai, M. Riede, E. Garratt, and A. Roch, "A comprehensive study on Fused Filament Fabrication of Ti-6Al-4V structures," *Additive Manufacturing,* vol. 34, p. 101256, 2020.
[73] F. Zenhausern, M. O’boyle, and H. Wickramasinghe, "Apertureless near‐field optical microscope," *Applied Physics Letters,* vol. 65, no. 13, pp. 1623-1625, 1994.
[74] J. W. Bacus and L. J. Grace, "Optical microscope system for standardized cell measurements and analyses," *Applied Optics,* vol. 26, no. 16, pp. 3280-3293, 1987.
[75] U. S. Kim and J. W. Park, "High-quality surface finishing of industrial three-dimensional metal additive manufacturing using electrochemical polishing," *International Journal of Precision Engineering and Manufacturing-Green Technology,* vol. 6, no. 1, pp. 11-21, 2019.
[76] B. Vayssette, N. Saintier, C. Brugger, M. El May, and E. Pessard, "Numerical modelling of surface roughness effect on the fatigue behavior of Ti-6Al-4V obtained by additive manufacturing," *International Journal of Fatigue,* vol. 123, pp. 180-195, 2019.
[77] Q. Liu *et al.*, "Machine-learning assisted laser powder bed fusion process optimization for AlSi10Mg: new microstructure description indices and fracture mechanisms," *Acta Materialia,* vol. 201, pp. 316-328, 2020.
[78] M. Zhang *et al.*, "Fatigue and fracture behaviour of laser powder bed fusion stainless steel 316L: Influence of processing parameters," *Materials Science and Engineering: A,* vol. 703, pp. 251-261, 2017.
[79] A. Li, S. Baig, J. Liu, S. Shao, and N. Shamsaei, "Defect criticality analysis on fatigue life of L-PBF 17-4 PH stainless steel via machine learning," *International Journal of Fatigue,* vol. 163, p. 107018, 2022.

[80] K. Vernon-Parry, "Scanning electron microscopy: an introduction," *III-Vs Review*, vol. 13, no. 4, pp. 40-44, 2000.
[81] A. Thompson, D. McNally, I. Maskery, and R. K. Leach, "X-ray computed tomography and additive manufacturing in medicine: a review," *International Journal of Metrology and Quality Engineering*, vol. 8, p. 17, 2017.
[82] A. Thompson, I. Maskery, and R. K. Leach, "X-ray computed tomography for additive manufacturing: a review," *Measurement Science and Technology*, vol. 27, no. 7, p. 072001, 2016.
[83] A. Du Plessis, I. Yadroitsev, I. Yadroitsava, and S. G. Le Roux, "X-ray microcomputed tomography in additive manufacturing: a review of the current technology and applications," *3D Printing and Additive Manufacturing*, vol. 5, no. 3, pp. 227-247, 2018.
[84] L. De Chiffre, S. Carmignato, J.-P. Kruth, R. Schmitt, and A. Weckenmann, "Industrial applications of computed tomography," *CIRP annals*, vol. 63, no. 2, pp. 655-677, 2014.
[85] L. Meng *et al.*, "Machine learning in additive manufacturing: a review," *Jom*, vol. 72, no. 6, pp. 2363-2377, 2020.
[86] N. Johnson *et al.*, "Invited review: Machine learning for materials developments in metals additive manufacturing," *Additive Manufacturing*, vol. 36, p. 101641, 2020.
[87] C. M. Bishop, *Pattern recognition and machine learning*. springer, 2006.
[88] I. Goodfellow, Y. Bengio, and A. Courville, *Deep learning*. MIT press, 2016.
[89] C. Molnar, *Interpretable Machine Learning*. Lulu. com, 2020.
[90] C. Zhang and Y. Ma, *Ensemble machine learning: methods and applications*. Springer, 2012.
[91] J. Liu, J. Ye, D. F. Silva, A. Vinel, N. Shamsaei, and S. Shao, "A Review of Machine Learning Techniques for Process and Performance Optimization in Laser Beam Powder Bed Fusion Additive Manufacturing," 2022.
[92] A. Plastics. "ABS plastic properties." https://www.adrecoplastics.co.uk/abs-plastic-properties-and-application (accessed.
[93] B. de Araujo Gomes *et al.*, "In-house three-dimensional printing workflow for face shield during COVID-19 pandemic," *The Journal of Craniofacial Surgery*, 2020.
[94] P. s. c. o. technology. "Penn College professor manufactures ventilator splitters." https://pctoday.pct.edu/penn-college-professor-manufactures-ventilator-splitters/ (accessed.
[95] B. E. Yamamoto, A. Z. Trimble, B. Minei, and M. N. Ghasemi Nejhad, "Development of multifunctional nanocomposites with 3-D printing additive manufacturing and low graphene loading," *Journal of Thermoplastic Composite Materials*, vol. 32, no. 3, pp. 383-408, 2019.
[96] P. K. Rao, J. P. Liu, D. Roberson, Z. J. Kong, and C. Williams, "Online real-time quality monitoring in additive manufacturing processes using heterogeneous sensors," *Journal of Manufacturing Science and Engineering*, vol. 137, no. 6, 2015.
[97] A. Poudel *et al.*, "Feature-based volumetric defect classification in metal additive manufacturing " 2022.
[98] V. P. Matilainen, H. Piili, A. Salminen, and O. Nyrhilä, "Preliminary investigation of keyhole phenomena during single layer fabrication in laser additive manufacturing of stainless steel," *Physics Procedia*, vol. 78, pp. 377-387, 2015.

[99] M. Courtois, M. Carin, P. Le Masson, S. Gaied, and M. Balabane, "A complete model of keyhole and melt pool dynamics to analyze instabilities and collapse during laser welding," *Journal of Laser applications*, vol. 26, no. 4, p. 042001, 2014.
[100] M. Tang, P. C. Pistorius, and J. L. Beuth, "Prediction of lack-of-fusion porosity for powder bed fusion," *Additive Manufacturing*, vol. 14, pp. 39-48, 2017.
[101] Q. C. Liu, J. Elambasseril, S. J. Sun, M. Leary, M. Brandt, and P. K. Sharp, "The effect of manufacturing defects on the fatigue behaviour of Ti-6Al-4V specimens fabricated using selective laser melting," in *Advanced Materials Research*, 2014, vol. 891: Trans Tech Publ, pp. 1519-1524.
[102] H. Gong, K. Rafi, H. Gu, G. J. Ram, T. Starr, and B. Stucker, "Influence of defects on mechanical properties of Ti–6Al–4 V components produced by selective laser melting and electron beam melting," *Materials & Design*, vol. 86, pp. 545-554, 2015.
[103] A. Fatemi *et al.*, "Fatigue behaviour of additive manufactured materials: An overview of some recent experimental studies on Ti‐6Al‐4V considering various processing and loading direction effects," *Fatigue & fracture of engineering materials & structures*, vol. 42, no. 5, pp. 991-1009, 2019.
[104] B. Torries, A. Imandoust, S. Beretta, S. Shao, and N. Shamsaei, "Overview on microstructure-and defect-sensitive fatigue modeling of additively manufactured materials," *Jom*, vol. 70, no. 9, pp. 1853-1862, 2018.
[105] A. Obaton *et al.*, "Investigation of new volumetric non-destructive techniques to characterise additive manufacturing parts," *Welding in the World*, vol. 62, pp. 1049-1057, 2018.
[106] J. T. Cantrell *et al.*, "Experimental characterization of the mechanical properties of 3D-printed ABS and polycarbonate parts," *Rapid Prototyping Journal*, 2017.
[107] P. K. Gurrala and S. P. Regalla, "DOE based parametric study of volumetric change of FDM parts," *Procedia materials science*, vol. 6, pp. 354-360, 2014.
[108] Z. Moza, K. Kitsakis, J. Kechagias, and N. Mastorakis, "Optimizing dimensional accuracy of fused filament fabrication using Taguchi design," in *Proceedings of the 14th International Conference on Instrumentation, Measurement, Circuits and Systems (IMCAS-14), Salerno, Italy*, 2015, pp. 27-29.
[109] T. Nancharaiah, "Optimization of process parameters in FDM process using design of experiments," *J Int J Emerg Technol*, vol. 2, no. 1, pp. 100-102, 2011.
[110] A. H. Peng and Z. M. Wang, "Researches into influence of process parameters on FDM parts precision," in *Applied Mechanics and Materials*, 2010, vol. 34: Trans Tech Publ, pp. 338-343.
[111] N. T. Aboulkhair, N. M. Everitt, I. Ashcroft, and C. Tuck, "Reducing porosity in AlSi10Mg parts processed by selective laser melting," *Additive Manufacturing*, vol. 1-4, pp. 77-86, 2014.
[112] N. Read, W. Wang, K. Essa, and M. M. Attallah, "Selective laser melting of AlSi10Mg alloy: Process optimisation and mechanical properties development," *Materials & Design (1980-2015)*, vol. 65, pp. 417-424, 2015.
[113] R. K. Shah and P. P. Dey, "Process parameter optimization of dmls process to produce AlSi10Mg components," *Journal of Physics: Conference Series*, vol. 1240, no. 1, p. 012011, 2019.

[114] J. Sun, Y. Yang, and D. Wang, "Parametric optimization of selective laser melting for forming Ti6Al4V samples by Taguchi method," *Optics & Laser Technology,* vol. 49, pp. 118-124, 2013.
[115] G. Tapia, S. Khairallah, M. Matthews, W. E. King, and A. Elwany, "Gaussian process-based surrogate modeling framework for process planning in laser powder-bed fusion additive manufacturing of 316L stainless steel," *The International Journal of Advanced Manufacturing Technology,* vol. 94, no. 9-12, pp. 3591-3603, 2017.
[116] L. Meng and J. Zhang, "Process Design of Laser Powder Bed Fusion of Stainless Steel Using a Gaussian Process-Based Machine Learning Model," *Jom,* vol. 72, no. 1, pp. 420-428, 2019.
[117] X. Zhang, J. Saniie, and A. Heifetz, "Detection of defects in additively manufactured stainless steel 316L with compact infrared camera and machine learning algorithms," *JOM,* vol. 72, no. 12, pp. 4244-4253, 2020.
[118] M. Abdelrahman, E. W. Reutzel, A. R. Nassar, and T. L. Starr, "Flaw detection in powder bed fusion using optical imaging," *Additive Manufacturing,* vol. 15, pp. 1-11, 2017.
[119] C. Kim, D. Espalin, A. Cuaron, M. A. Perez, E. MacDonald, and R. B. Wicker, "A study to detect a material deposition status in fused deposition modeling technology," in *2015 IEEE International Conference on Advanced Intelligent Mechatronics (AIM),* 2015: IEEE, pp. 779-783.
[120] H. Wu, Z. Yu, and Y. Wang, "A new approach for online monitoring of additive manufacturing based on acoustic emission," in *International Manufacturing Science and Engineering Conference,* 2016, vol. 49910: American Society of Mechanical Engineers, p. V003T08A013.
[121] Y. Wang *et al.*, "A CNN-based adaptive surface monitoring system for fused deposition modeling," *IEEE/ASME Transactions on Mechatronics,* vol. 25, no. 5, pp. 2287-2296, 2020.
[122] J.-R. Poulin, A. Kreitcberg, P. Terriault, and V. Brailovski, "Fatigue strength prediction of laser powder bed fusion processed Inconel 625 specimens with intentionally-seeded porosity: Feasibility study," *International Journal of Fatigue,* vol. 132, p. 105394, 2020.
[123] H. Masuo *et al.*, "Influence of defects, surface roughness and HIP on the fatigue strength of Ti-6Al-4V manufactured by additive manufacturing," *International Journal of Fatigue,* vol. 117, pp. 163-179, 2018.
[124] M. El Haddad, K. Smith, and T. Topper, "Fatigue crack propagation of short cracks," 1979.
[125] H. Bao, S. Wu, Z. Wu, G. Kang, X. Peng, and P. J. Withers, "A machine-learning fatigue life prediction approach of additively manufactured metals," *Engineering Fracture Mechanics,* vol. 242, p. 107508, 2021.
[126] S. Moon *et al.*, "Impact of surface and pore characteristics on fatigue life of laser powder bed fusion Ti–6Al–4V alloy described by neural network models," *Scientific reports,* vol. 11, no. 1, p. 20424, 2021.
[127] W. W. Wits and E. Amsterdam, "Fatigue prediction and life assessment method for metal laser powder bed fusion parts," *CIRP Annals,* 2023.
[128] E. Salvati, A. Tognan, L. Laurenti, M. Pelegatti, and F. De Bona, "A defect-based physics-informed machine learning framework for fatigue finite life prediction in additive manufacturing," *Materials & Design,* vol. 222, p. 111089, 2022.

[129] E. Akgun, X. Zhang, T. Lowe, Y. Zhang, and M. Doré, "Fatigue of laser powder-bed fusion additive manufactured Ti-6Al-4V in presence of process-induced porosity defects," *Engineering Fracture Mechanics,* vol. 259, p. 108140, 2022.
[130] N. T. Aboulkhair, N. M. Everitt, I. Ashcroft, and C. Tuck, "Reducing porosity in AlSi10Mg parts processed by selective laser melting," *Additive manufacturing,* vol. 1, pp. 77-86, 2014.
[131] G. Tapia, A. H. Elwany, and H. Sang, "Prediction of porosity in metal-based additive manufacturing using spatial Gaussian process models," *Additive Manufacturing,* vol. 12, pp. 282-290, 2016.
[132] R. Wang, J. Li, F. Wang, X. Li, and Q. Wu, "ANN model for the prediction of density in selective laser sintering," *International Journal of Manufacturing Research,* vol. 4, no. 3, pp. 362-373, 2009.
[133] J. Ye *et al.*, "Bayesian Process Optimization for Additively Manufactured Nitinol," in *2021 International Solid Freeform Fabrication Symposium*, 2021: University of Texas at Austin.
[134] J. Liu, C. Liu, Y. Bai, P. Rao, C. B. Williams, and Z. Kong, "Layer-wise spatial modeling of porosity in additive manufacturing," *IISE Transactions,* vol. 51, no. 2, pp. 109-123, 2019.
[135] W. W. Wits, S. Carmignato, F. Zanini, and T. H. Vaneker, "Porosity testing methods for the quality assessment of selective laser melted parts," *CIRP annals,* vol. 65, no. 1, pp. 201-204, 2016.
[136] D. Wu, Y. Wei, and J. Terpenny, "Predictive modelling of surface roughness in fused deposition modelling using data fusion," *International Journal of Production Research,* vol. 57, no. 12, pp. 3992-4006, 2019.
[137] U. Delli and S. Chang, "Automated process monitoring in 3D printing using supervised machine learning," *Procedia Manufacturing,* vol. 26, pp. 865-870, 2018.
[138] W. Cui, Y. Zhang, X. Zhang, L. Li, and F. Liou, "Metal Additive Manufacturing Parts Inspection Using Convolutional Neural Network," *Applied Sciences,* vol. 10, no. 2, p. 545, 2020.
[139] J. L. Bartlett, A. Jarama, J. Jones, and X. Li, "Prediction of microstructural defects in additive manufacturing from powder bed quality using digital image correlation," *Materials Science and Engineering: A,* vol. 794, p. 140002, 2020.
[140] M. Khanzadeh, L. Bian, N. Shamsaei, and S. M. Thompson, "Porosity detection of laser based additive manufacturing using melt pool morphology clustering," in *2016 International Solid Freeform Fabrication Symposium*, 2016: University of Texas at Austin.
[141] A. Garg, J. S. L. Lam, and M. M. Savalani, "A new computational intelligence approach in formulation of functional relationship of open porosity of the additive manufacturing process," *The International Journal of Advanced Manufacturing Technology*, vol. 80, no. 1, pp. 555-565, 2015.
[142] Z. Zhan and H. Li, "A novel approach based on the elastoplastic fatigue damage and machine learning models for life prediction of aerospace alloy parts fabricated by additive manufacturing," *International Journal of Fatigue,* vol. 145, p. 106089, 2021.
[143] M. Zhang *et al.*, "High cycle fatigue life prediction of laser additive manufactured stainless steel: A machine learning approach," *International Journal of Fatigue,* vol. 128, p. 105194, 2019.

[144] Z. Zhan and H. Li, "Machine learning based fatigue life prediction with effects of additive manufacturing process parameters for printed SS 316L," *International Journal of Fatigue,* vol. 142, p. 105941, 2021.
[145] M. Zhang, C.-N. Sun, X. Zhang, J. Wei, D. Hardacre, and H. Li, "Predictive models for fatigue property of laser powder bed fusion stainless steel 316L," *Materials & Design,* vol. 145, pp. 42-54, 2018.
[146] A. Li, S. Baig, J. Liu, S. Shao, and N. Shamsaei, "Defect Criticality Analysis on Fatigue Life of L-PBF 17-4 PH Stainless Steel via Machine Learning," *International Journal of Fatigue,* p. 107018, 2022.
[147] J. Li, Z. Yang, G. Qian, and F. Berto, "Machine learning based very-high-cycle fatigue life prediction of Ti-6Al-4V alloy fabricated by selective laser melting," *International Journal of Fatigue*, vol. 158, p. 106764, 2022.
[148] Y. Luo *et al.*, "Pore-affected fatigue life scattering and prediction of additively manufactured Inconel 718: An investigation based on miniature specimen testing and machine learning approach," *Materials Science and Engineering: A,* vol. 802, p. 140693, 2021.
[149] Y. Murakami, "Analysis of stress intensity factors of modes I, II and III for inclined surface cracks of arbitrary shape," *Engineering Fracture Mechanics,* vol. 22, no. 1, pp. 101-114, 1985.
[150] S. Shao, A. Poudel, and N. Shamsaei, "A Linear Elastic Finite Element Approach to Fatigue Life Estimation for Defect Laden Materials," *Engineering Fracture Mechanics,* p. 109298, 2023.
[151] I. Maskery *et al.*, "Quantification and characterisation of porosity in selectively laser melted Al–Si10–Mg using X-ray computed tomography," *Materials Characterization,* vol. 111, pp. 193-204, 2016.
[152] J. Ye *et al.*, "Machine learning augmented X-ray computed tomography features for volumetric defect classification in laser beam powder bed fusion," *The International Journal of Advanced Manufacturing Technology,* pp. 1-15, 2023.
[153] A. Poudel *et al.*, "Feature-based volumetric defect classification in metal additive manufacturing," *Nature Communications*, vol. 13, no. 1, pp. 1-12, 2022.
[154] J. Damon, S. Dietrich, F. Vollert, J. Gibmeier, and V. Schulze, "Process dependent porosity and the influence of shot peening on porosity morphology regarding selective laser melted AlSi10Mg parts," *Additive Manufacturing,* vol. 20, pp. 77-89, 2018.
[155] M. Muhammad, S. Shao, and N. Shamsaei, "Effect of Defects on the Mechanical Properties of Laser Powder Bed Fused Ti-6Al-4V," in *2022 International Solid Freeform Fabrication Symposium*, 2022.
[156] B. Shen *et al.*, "Influence of laser post-processing on pore evolution of Ti–6Al–4V alloy by laser powder bed fusion," *Journal of Alloys and Compounds,* vol. 818, p. 152845, 2020.
[157] A. du Plessis and P. Rossouw, "Investigation of porosity changes in cast Ti6Al4V rods after hot isostatic pressing," *Journal of Materials Engineering and Performance,* vol. 24, no. 8, pp. 3137-3141, 2015.
[158] D. S. Watring, J. T. Benzing, N. Hrabe, and A. D. Spear, "Effects of laser-energy density and build orientation on the structure–property relationships in as-built Inconel 718 manufactured by laser powder bed fusion," *Additive manufacturing,* vol. 36, p. 101425, 2020.

[159] S. Tammas-Williams, H. Zhao, F. Léonard, F. Derguti, I. Todd, and P. B. Prangnell, "XCT analysis of the influence of melt strategies on defect population in Ti–6Al–4V components manufactured by Selective Electron Beam Melting," *Materials Characterization,* vol. 102, pp. 47-61, 2015.
[160] N. Sanaei, A. Fatemi, and N. Phan, "Defect characteristics and analysis of their variability in metal L-PBF additive manufacturing," *Materials & Design,* vol. 182, p. 108091, 2019.
[161] M. Benedetti, V. Fontanari, M. Bandini, F. Zanini, and S. Carmignato, "Low-and high-cycle fatigue resistance of Ti-6Al-4V ELI additively manufactured via selective laser melting: Mean stress and defect sensitivity," *International journal of fatigue,* vol. 107, pp. 96-109, 2018.
[162] N. Omar, N. Shuaib, M. Ab Hadi, and A. Azmi, "Mechanical properties of carbon and glass fibre reinforced composites produced by additive manufacturing: A short review," in *IOP Conference Series: Materials Science and Engineering*, 2019, vol. 670, no. 1: IOP Publishing, p. 012020.
[163] N. Vidakis, A. Maniadi, M. Petousis, M. Vamvakaki, G. Kenanakis, and E. Koudoumas, "Mechanical and Electrical Properties Investigation of 3D-Printed Acrylonitrile–Butadiene–Styrene Graphene and Carbon Nanocomposites," *Journal of Materials Engineering and Performance,* pp. 1-10, 2020.
[164] D. Jiang and D. E. Smith, "Anisotropic mechanical properties of oriented carbon fiber filled polymer composites produced with fused filament fabrication," *Additive Manufacturing,* vol. 18, pp. 84-94, 2017.
[165] F. Ning, W. Cong, Y. Hu, and H. Wang, "Additive manufacturing of carbon fiber-reinforced plastic composites using fused deposition modeling: Effects of process parameters on tensile properties," *Journal of Composite Materials,* vol. 51, no. 4, pp. 451-462, 2017.
[166] F. Ning, W. Cong, J. Qiu, J. Wei, and S. Wang, "Additive manufacturing of carbon fiber reinforced thermoplastic composites using fused deposition modeling," *Composites Part B: Engineering,* vol. 80, pp. 369-378, 2015.
[167] P. Parandoush and D. Lin, "A review on additive manufacturing of polymer-fiber composites," *Composite Structures,* vol. 182, pp. 36-53, 2017.
[168] H. Guo, R. Lv, and S. Bai, "Recent advances on 3D printing graphene-based composites," *Nano Materials Science,* vol. 1, no. 2, pp. 101-115, 2019.
[169] X. Wei *et al.*, "3D printable graphene composite," *Scientific reports,* vol. 5, p. 11181, 2015.
[170] J. H. Sandoval and R. B. Wicker, "Functionalizing stereolithography resins: effects of dispersed multi‐walled carbon nanotubes on physical properties," *Rapid Prototyping Journal,* 2006.
[171] G. Carotenuto, V. Romeo, I. Cannavaro, D. Roncato, B. Martorana, and M. Gosso, "Graphene-polymer composites," in *International Conference on Structural Nano Composites (NANOSTRUC 2012)*, Cranfield University, Bedfordshire, UK, 2–4 July 2012 2012, vol. 40, no. IOP Conference Series: Materials Science and Engineering: IOP Publishing.
[172] N. Hong *et al.*, "Enhanced mechanical, thermal and flame retardant properties by combining graphene nanosheets and metal hydroxide nanorods for Acrylonitrile–

Butadiene–Styrene copolymer composite," *Composites Part A: Applied Science and Manufacturing,* vol. 64, pp. 203-210, 2014.
[173] S. Dul, L. Fambri, and A. Pegoretti, "Fused deposition modelling with ABS–graphene nanocomposites," *Composites Part A: Applied Science and Manufacturing,* vol. 85, pp. 181-191, 2016.
[174] K. Sakunphokesup, P. Kongkrengkri, A. Pongwisuthiruchte, C. Aumnate, and P. Potiyaraj, "Graphene-enhanced ABS for FDM 3D printing: effects of masterbatch preparation techniques," in *IOP Conference Series: Materials Science and Engineering*, 2019, vol. 600, no. 1: IOP Publishing, p. 012001.
[175] R. Singh, G. S. Sandhu, R. Penna, and I. Farina, "Investigations for thermal and electrical conductivity of ABS-graphene blended prototypes," *Materials*, vol. 10, no. 8, p. 881, 2017.
[176] G. S. Sandhu and R. Singh, "Development of ABS-Graphene Blended Feedstock Filament for FDM Process," in *Additive Manufacturing of Emerging Materials*: Springer, 2019, pp. 279-297.
[177] C. Aumnate, A. Pongwisuthiruchte, P. Pattananuwat, and P. Potiyaraj, "Fabrication of ABS/graphene oxide composite filament for fused filament fabrication (FFF) 3D printing," *Advances in Materials Science and engineering,* vol. 2018, 2018.
[178] K. Gnanasekaran *et al.*, "3D printing of CNT-and graphene-based conductive polymer nanocomposites by fused deposition modeling," *Applied materials today,* vol. 9, pp. 21-28, 2017.
[179] V. Tambrallimath, R. Keshavamurthy, S. D, P. G. Koppad, and G. S. P. Kumar, "Thermal behavior of PC-ABS based graphene filled polymer nanocomposite synthesized by FDM process," *Composites Communications,* vol. 15, pp. 129-134, 2019. [Online]. Available: https://www.sciencedirect.com/science/article/pii/S2452213919300981.
[180] N. Vidakis, M. Petousis, A. Maniadi, E. Koudoumas, M. Liebscher, and L. Tzounis, "Mechanical Properties of 3D-Printed Acrylonitrile–Butadiene–Styrene TiO2 and ATO Nanocomposites," *Polymers,* vol. 12, no. 7, 2020.
[181] N. Vidakis *et al.*, "The Mechanical and Physical Properties of 3D-Printed Materials Composed of ABS-ZnO Nanocomposites and ABS-ZnO Microcomposites," *Micromachines,* vol. 11, no. 6, 2020.
[182] C. E. Rasmussen, "Gaussian Processes in Machine Learning," in *Advanced Lectures on Machine Learning: ML Summer Schools 2003, Canberra, Australia, February 2 - 14, 2003, Tübingen, Germany, August 4 - 16, 2003, Revised Lectures,* O. Bousquet, U. von Luxburg, and G. Rätsch Eds. Berlin, Heidelberg: Springer Berlin Heidelberg, 2004, pp. 63-71.
[183] C. K. Williams and C. E. Rasmussen, "Gaussian processes for regression," 1996.
[184] T. Savitsky, M. Vannucci, and N. Sha, "Variable Selection for Nonparametric Gaussian Process Priors: Models and Computational Strategies," (in eng), *Stat Sci,* vol. 26, no. 1, pp. 130-149, 2011.
[185] H. G. Sung, "Gaussian mixture regression and classification," Ph.D., Rice University, Ann Arbor, 3122551, 2004.
[186] G. Tapia, S. Khairallah, M. Matthews, W. E. King, and A. Elwany, "Gaussian process-based surrogate modeling framework for process planning in laser powder-bed fusion additive manufacturing of 316L stainless steel," *The International Journal of Advanced Manufacturing Technology,* vol. 94, no. 9, pp. 3591-3603, 2018.

[187] J. Liu, O. Beyca, P. Rao, Z. Kong, and S. Bukkapatnam, "Dirichlet Process Gaussian Mixture Models for Real-Time Monitoring and Their Application to Chemical Mechanical Planarization," *IEEE Transactions on Automation Science and Engineering,* vol. 14, no. 1, pp. 208-221, 2017.
[188] P. K. Rao, J. Liu, D. Roberson, Z. Kong, and C. Williams, "Online Real-Time Quality Monitoring in Additive Manufacturing Processes Using Heterogeneous Sensors," *Journal of Manufacturing Science and Engineering,* vol. 137, no. 6, 2015.
[189] I. Durgun and R. Ertan, "Experimental investigation of FDM process for improvement of mechanical properties and production cost," *Rapid Prototyping Journal,* 2014.
[190] L. Ventola *et al.*, "Rough surfaces with enhanced heat transfer for electronics cooling by direct metal laser sintering," *International Journal of Heat and Mass Transfer,* vol. 75, pp. 58-74, 2014.
[191] N. Jayanth, P. Senthil, and C. Prakash, "Effect of chemical treatment on tensile strength and surface roughness of 3D-printed ABS using the FDM process," *Virtual and Physical Prototyping,* vol. 13, no. 3, pp. 155-163, 2018.
[192] J. Antony, *Design of experiments for engineers and scientists*. Elsevier, 2014.
[193] P. K. Rao, J. Liu, D. Roberson, and Z. Kong, "Sensor-Based Online Process Fault Detection in Additive Manufacturing," in *ASME 2015 International Manufacturing Science and Engineering Conference,* 2015, vol. Volume 2: Materials; Biomanufacturing; Properties, Applications and Systems; Sustainable Manufacturing, V002T04A010.
[194] D. Chaidas and J. D. Kechagias, "An investigation of PLA/W parts quality fabricated by FFF," *Materials and Manufacturing Processes,* pp. 1-9, 2021.
[195] E. Sirjani, P. J. Cragg, and M. K. Dymond, "Glass transition temperatures, melting temperatures, water contact angles and dimensional precision of simple fused deposition model 3D prints and 3D printed channels constructed from a range of commercially available filaments," *Chemical Data Collections,* vol. 22, p. 100244, 2019.
[196] J. H. Los, K. V. Zakharchenko, M. I. Katsnelson, and A. Fasolino, "Melting temperature of graphene," *Physical Review B,* vol. 91, no. 4, 2015.
[197] J. A. Afonso, J. L. Alves, G. Caldas, B. P. Gouveia, L. Santana, and J. Belinha, "Influence of 3D printing process parameters on the mechanical properties and mass of PLA parts and predictive models," *Rapid Prototyping Journal,* vol. ahead-of-print, no. ahead-of-print, 2021.
[198] K. Sakunphokesup, P. Kongkrengkri, A. Pongwisuthiruchte, C. Aumnate, and P. Potiyaraj, "Graphene-enhanced ABS for FDM 3D printing: effects of masterbatch preparation techniques," *IOP Conference Series: Materials Science and Engineering,* vol. 600, p. 012001, 2019.
[199] H. 3D. "Flow Rate." http://hyrel3d.net/wiki/index.php/Flow_Rate (accessed.
[200] R. B. Gramacy, *Surrogates: Gaussian process modeling, design, and optimization for the applied sciences*. CRC Press, 2020.
[201] M. T. Ribeiro, S. Singh, and C. Guestrin, "Model-agnostic interpretability of machine learning," *arXiv preprint arXiv:1606.05386,* 2016.
[202] A. Fisher, C. Rudin, and F. Dominici, "Model class reliance: Variable importance measures for any machine learning model class, from the "Rashomon" perspective. arXiv 2018," *arXiv preprint arXiv:1801.01489*.
[203] C.-F. Wu and M. Hamada, *Experiments : planning, analysis, and optimization,* 2nd ed. (Wiley series in probability and statistics). Hoboken, N.J.: Wiley, 2009, pp. xxix, 716 p.

[204] L. Sullivan, "Hypothesis testing-analysis of variance (ANOVA)," *Prospective versus Retrospective Studies,* 2016.

[205] A. Poudel *et al.*, "Feature-based volumetric defect classification in metal additive manufacturing," *Nature Communications,* vol. 13, no. 1, p. 6369, 2022.

[206] H. Villarraga. Gómez, C. M. Peitsch, A. Ramsey, and S. T. Smith, "The role of computed tomography in additive manufacturing," in *2018 ASPE and euspen summer topical meeting: advancing precision in additive manufacturing,* 2018, vol. 69, pp. 201-209.

[207] H. Villarraga-Gómez, C. M. Peitsch, A. Ramsey, and S. T. Smith, "The role of computed tomography in additive manufacturing," in *2018 ASPE and euspen summer topical meeting: advancing precision in additive manufacturing*, 2018, vol. 69, pp. 201-209.

[208] W. E. King *et al.*, "Observation of keyhole-mode laser melting in laser powder-bed fusion additive manufacturing," *Journal of Materials Processing Technology,* vol. 214, no. 12, pp. 2915-2925, 2014.

[209] I. E. Anderson, E. M. White, and R. Dehoff, "Feedstock powder processing research needs for additive manufacturing development," *Current Opinion in Solid State and Materials Science,* vol. 22, no. 1, pp. 8-15, 2018.

[210] G. Chen, S. Zhao, P. Tan, J. Wang, C. Xiang, and H. Tang, "A comparative study of Ti-6Al-4V powders for additive manufacturing by gas atomization, plasma rotating electrode process and plasma atomization," *Powder technology,* vol. 333, pp. 38-46, 2018.

[211] T. Qi, H. Zhu, H. Zhang, J. Yin, L. Ke, and X. Zeng, "Selective laser melting of Al7050 powder: Melting mode transition and comparison of the characteristics between the keyhole and conduction mode," *Materials & Design,* vol. 135, pp. 257-266, 2017.

[212] Q. Luo, L. Yin, T. W. Simpson, and A. M. Beese, "Effect of processing parameters on pore structures, grain features, and mechanical properties in Ti-6Al-4V by laser powder bed fusion," *Additive Manufacturing,* vol. 56, p. 102915, 2022.

[213] R. Esmaeilizadeh *et al.*, "On the effect of laser powder-bed fusion process parameters on quasi-static and fatigue behaviour of Hastelloy X: A microstructure/defect interaction study," *Additive Manufacturing,* vol. 38, p. 101805, 2021.

[214] M. A. Buhairi *et al.*, "Review on volumetric energy density: influence on morphology and mechanical properties of Ti6Al4V manufactured via laser powder bed fusion," *Progress in Additive Manufacturing,* pp. 1-19, 2022.

[215] M. Vetterli, R. Kleijnen, M. Schmid, and K. Wegener, "Process impact of elliptic smoothness and powder shape factors on additive manufacturing with laser sintering," in *Online Proceedings: 76nd Annual Technical Conference of the Society of Plastics Engineers (ANTEC 2018),* 2018: Society of Plastics Engineers.

[216] J. Zheng and R. D. Hryciw, "Roundness and sphericity of soil particles in assemblies by computational geometry," *Journal of Computing in Civil Engineering,* vol. 30, no. 6, p. 04016021, 2016.

[217] I. Baturynska, "Statistical analysis of dimensional accuracy in additive manufacturing considering STL model properties," *The International Journal of Advanced Manufacturing Technology,* vol. 97, no. 5, pp. 2835-2849, 2018.

[218] M. Kusano *et al.*, "Tensile properties prediction by multiple linear regression analysis for selective laser melted and post heat-treated Ti-6Al-4V with microstructural quantification," *Materials Science and Engineering: A,* vol. 787, p. 139549, 2020.

[219] R. Li, M. Jin, and V. C. Paquit, "Geometrical defect detection for additive manufacturing with machine learning models," *Materials & Design*, vol. 206, p. 109726, 2021.
[220] J. Liu, J. Ye, F. Momin, X. Zhang, and A. Li, "Nonparametric bayesian framework for material and process optimization with nanocomposite fused filament fabrication," *Additive Manufacturing*, p. 102765, 2022.
[221] L. Meng and J. Zhang, "Process Design of Laser Powder Bed Fusion of Stainless Steel Using a Gaussian Process-Based Machine Learning Model," *JOM*, vol. 72, no. 1, pp. 420-428, 2020.
[222] J. P. Liu, O. F. Beyca, P. K. Rao, Z. J. Kong, and S. T. Bukkapatnam, "Dirichlet process Gaussian mixture models for real-time monitoring and their application to chemical mechanical planarization," *IEEE Transactions on Automation Science and Engineering*, vol. 14, no. 1, pp. 208-221, 2016.
[223] M. Samie Tootooni, A. Dsouza, R. Donovan, P. K. Rao, Z. J. Kong, and P. Borgesen, "Classifying the dimensional variation in additive manufactured parts from laser-scanned three-dimensional point cloud data using machine learning approaches," *Journal of Manufacturing Science and Engineering*, vol. 139, no. 9, 2017.
[224] M. Khanzadeh, S. Chowdhury, M. Marufuzzaman, M. A. Tschopp, and L. Bian, "Porosity prediction: Supervised-learning of thermal history for direct laser deposition," *Journal of Manufacturing Systems*, vol. 47, pp. 69-82, 2018.
[225] C. Gobert, E. W. Reutzel, J. Petrich, A. R. Nassar, and S. Phoha, "Application of supervised machine learning for defect detection during metallic powder bed fusion additive manufacturing using high resolution imaging," *Additive Manufacturing*, vol. 21, pp. 517-528, 2018.
[226] K. Aoyagi, H. Wang, H. Sudo, and A. Chiba, "Simple method to construct process maps for additive manufacturing using a support vector machine," *Additive manufacturing*, vol. 27, pp. 353-362, 2019.
[227] V. W. H. Wong, M. Ferguson, K. H. Law, Y.-T. T. Lee, and P. Witherell, "Segmentation of Additive Manufacturing Defects Using U-Net," *Journal of Computing and Information Science in Engineering*, vol. 22, no. 3, 2021.
[228] C. A. Schneider, W. S. Rasband, and K. W. Eliceiri, "NIH Image to ImageJ: 25 years of image analysis," *Nature Methods*, vol. 9, no. 7, pp. 671-675, 2012.
[229] B. Wu *et al.*, "A review of the wire arc additive manufacturing of metals: properties, defects and quality improvement," *Journal of Manufacturing Processes*, vol. 35, pp. 127-139, 2018.
[230] Y. Chen, K. Zhang, J. Huang, S. R. E. Hosseini, and Z. Li, "Characterization of heat affected zone liquation cracking in laser additive manufacturing of Inconel 718," *Materials & Design*, vol. 90, pp. 586-594, 2016.
[231] T. Brugo, R. Palazzetti, S. Ciric-Kostic, X. Yan, G. Minak, and A. Zucchelli, "Fracture mechanics of laser sintered cracked polyamide for a new method to induce cracks by additive manufacturing," *Polymer Testing*, vol. 50, pp. 301-308, 2016.
[232] S. K. Chilelli, J. J. Schomer, and M. J. Dapino, "Detection of crack initiation and growth using Fiber Bragg grating sensors embedded into metal structures through ultrasonic additive manufacturing," *Sensors*, vol. 19, no. 22, p. 4917, 2019.
[233] E. Wycisk, A. Solbach, S. Siddique, D. Herzog, F. Walther, and C. Emmelmann, "Effects of defects in laser additive manufactured Ti-6Al-4V on fatigue properties," *Physics Procedia*, vol. 56, pp. 371-378, 2014.

[234] J. Gockel, L. Sheridan, B. Koerper, and B. Whip, "The influence of additive manufacturing processing parameters on surface roughness and fatigue life," *International Journal of Fatigue,* vol. 124, pp. 380-388, 2019.
[235] W. Walton, "Feret‘s statistical diameter as a measure of particle size," *Nature,* vol. 162, no. 4113, pp. 329-330, 1948.
[236] Y. Mingqiang, K. Kidiyo, and R. Joseph, "A survey of shape feature extraction techniques," *Pattern recognition,* vol. 15, no. 7, pp. 43-90, 2008.
[237] Y. Takashimizu and M. Iiyoshi, "New parameter of roundness R: circularity corrected by aspect ratio," *Progress in Earth and Planetary Science,* vol. 3, no. 1, pp. 1-16, 2016.
[238] A. S. f. Testing and Materials, "ASTM E8-E8M: standard test methods for tension testing of metallic materials," ed: ASTM International West Conshohocken, 2016.
[239] M. D. Abràmoff, P. J. Magalhães, and S. J. Ram, "Image processing with ImageJ," *Biophotonics international,* vol. 11, no. 7, pp. 36-42, 2004.
[240] X. Cui, S. Zhang, C. Zhang, J. Chen, J. Zhang, and S. Dong, "Additive manufacturing of 24CrNiMo low alloy steel by selective laser melting: influence of volumetric energy density on densification, microstructure and hardness," *Materials Science and Engineering: A,* vol. 809, p. 140957, 2021.
[241] S. Senck *et al.*, "Additive manufacturing and non-destructive testing of topology-optimised aluminium components," *Nondestructive Testing and Evaluation,* vol. 35, no. 3, pp. 315-327, 2020.